2013-12-01

Obstacles and Solutions to Studying Functional Adhesives Using Vibrational Sum-Frequency Generation Spectroscopy

Angela Renee Andersen
Brigham Young University - Provo

BYU ScholarsArchive Citation

Andersen, Angela Renee, "Obstacles and Solutions to Studying Functional Adhesives Using Vibrational Sum-Frequency Generation Spectroscopy" (2013). *All Theses and Dissertations*. 4267.
https://scholarsarchive.byu.edu/etd/4267

Obstacles and Solutions to Studying Functional Adhesives Using Vibrational Sum-Frequency Generation Spectroscopy

Angela Renée Andersen

A dissertation submitted to the faculty of
Brigham Young University
in partial fulfillment of the requirements for the degree of

Doctor of Philosophy

James E. Patterson, Chair
Matthew C. Asplund
Steven R. Goates
Thomas A. Knotts
Eric T. Sevy

Department of Chemistry and Biochemistry

Brigham Young University

December 2013

ABSTRACT

Obstacles and Solutions to Studying Functional Adhesives Using Vibrational Sum-Frequency Generation Spectroscopy

Angela Renée Andersen
Department of Chemistry and Biochemistry, BYU
Doctor of Philosophy

Important aspects of adhesion occur at interfaces, including structures that may be different from those in the bulk materials. However, probing the orientation of molecules in functional adhesives poses a significant challenge because adhesive molecules are always located at a buried interface. The limited penetration depth of surface-specific analysis prohibits the study of buried interfaces using those techniques. The large quantity of bulk molecules relative to the adhesive molecules interacting at the interface results in the bulk signal swamping out adhesive signal in bulk analysis techniques. An interface-specific technique is required to study functional adhesives. One such technique that has shown promise in recent years is Vibrational sum frequency generation (VSFG) spectroscopy. This technique is useful for studying interactions that occur at surfaces and interfaces because it selectively probes regions of broken inversion symmetry.

Despite the ability of VSFG to isolate signal from a buried interface, a non-resonant signal that is produced simultaneously with the resonant signal corrupts the vibrational data of interest and greatly impedes reliable analysis of VSFG spectra. Over the last several years, researchers have experimentally removed non-resonant signal by delaying the upconverting pulse with respect to the initial excitation. Obtaining reliable results from VSFG data depends upon complete removal of non-resonant signal. However, complete removal of non-resonant signal presents a challenge because it can be present in spectra even when the indicators of non-resonant signal are absent. By taking advantage of polarization selection rules for VSFG and the differing symmetry of an azimuthally isotropic film and an azimuthally non-isotropic substrate, spectra containing non-resonant signal can be easily identified.

These and other advances in VSFG methodology have enabled the study of surface and interfacial systems of interest. In a study of the effects of plasma treatment on polystyrene thin films, plasma exposure was found to affect not only the free surface but also portions of the sub-surface polymer, challenging previous assumptions that plasma effects are constrained to the free surfaces of materials. The next step is to use VSFG to study functional adhesives under known amounts of applied stress. An apparatus is in place to simultaneously collect VSFG spectra during mechanical testing of a functional adhesive, and in preliminary studies, an increase in VSFG non-resonant signal has been observed when a pulling force is applied to the adhesive bond.

Keywords: adhesion, plasma treatment, surface spectroscopy, sum-frequency generation spectroscopy, nonlinear spectroscopy, polymers, strength testing, spin-coating, signal processing

ACKNOWLEDGEMENTS

The work included in this dissertation represents one of my proudest accomplishments, and I wish to thank some of the many people and organizations that made this great accomplishment possible. During my graduate studies I have received funding from the U.S. Airforce, and was awarded the Nicholes Maw Fellowship and Roland K. Robins Research Fellowship. I am also grateful for the generous financial support I received from the Hayswood Foundation in the form of the Elsie Downing Scholarship that completely funded my undergraduate education and gave me the financial freedom to pursue this graduate degree.

I am thankful to have had Dr. Patterson as my academic adviser during my graduate program who has provided helpful guidance and needed encouragement throughout this process. My committee has also helped to guide my research and has helped motivate me to work diligently throughout this time. I also thank the kind and helpful staff of the BYU Department of Chemistry and Biochemistry, especially Janet Fonoimoana.

Last but not least, I thank my family and friends for their continuing support; my parents, who always encouraged me to value education and taught me a love of learning, and my husband, Aaron Andersen, who has helped me to see my potential and supported me emotionally in the final stages of completing my graduate work.

CONTENTS

Chapter 1: Introduction and Background

1.1 The challenge of probing molecular structures in functional adhesives

Paints, coatings, lubricants, and adhesives are used across many disciplines, and all depend upon the adhesive behavior of the materials involved. Despite the importance of the adhesive phenomena, adhesive design is still performed primarily by trial and error. Adhesion behavior is dictated by specific molecular-level interactions at the interface between two or more materials. If the orientation of the molecules involved in adhesive interactions could be determined and correlated to the performance of the adhesive, directed design of adhesives could become possible.

Mechanical testing is typically used to study the behavior of adhesives; however, this type of characterization is inherently destructive. One of the simplest tests of adhesion is a peel test, in which a piece of cellophane tape is pressed onto a coating and then peeled away. If the tape lifts the coating at all, it fails the peel test, and if the coating does not peel away, it passes the peel test. This test does not always destroy the adhesive bond but also only provides qualitative information relating to the adhesive bond.

Quantitative testing on adhesive bonds can be performed using mechanical strength testing. These tests are performed by bonding two substrates with the adhesive to be tested and pulling the bond apart while measuring the load and the distance between the two substrates. These tests reveal the strength of the adhesive interaction but do not give any information regarding molecular-level behavior and often end in the destruction of the adhesive bond.

Spectroscopic characterization leaves the adhesive bond intact, but poses its own challenges. Bulk spectroscopies, such as FTIR, probe all molecules in a sample but fail to retrieve useful information from the interfaces. Because most molecules in the sample are in the bulk, the signal from bulk molecules drowns out any signal from the interfacial molecules participating in adhesion. Most inherently surface-specific techniques also fall short in capturing information from molecules involved in a functional adhesive bond because the probing depth of these techniques is insufficient. A technique well-suited for the study of functional adhesives must have sufficient probing depth to access a buried interface yet be able to also distinguish between molecules at the interface and in the bulk. Vibrational sum-frequency generation spectroscopy (VSFG) is a technique capable of such selectivity.

1.2 Overview of Vibrationally Resonant Sum-Frequency Generation Spectroscopy

The interaction of low intensity electromagnetic radiation with matter–such as in the case of absorption, reflection, and scattering–can be described by the expression

$$\vec{P} = \varepsilon_0 \chi^{(1)} \vec{E} \tag{1.1}$$

where $\vec{P}$ is the total polarization due to the electric field, ε_0 is the vacuum permittivity, $\chi^{(1)}$ represents the tensor describing the linear polarizability, and $\vec{E}$ is the electric field vector. However, when high intensity pulsed lasers are used, higher order terms must be added to the expression to account for these interactions, as expressed by

$$P = \varepsilon_0 \chi^{(1)} \vec{E} + \varepsilon_0 \sum_{ijk} \chi^{(2)}_{ijk} \vec{E}_j \vec{E}_k + \ldots \tag{1.2}$$

where $\chi^{(2)}_{ijk}$ represents the tensor that describes the second-order susceptibility, and the $\overrightarrow{E_n}$ vectors represent incident electric fields. The second term in (1.2) gives rise to second-order nonlinear optical processes such as second harmonic generation, sum frequency generation, difference frequency generation, and optical rectification.[1]

1.2.1 Symmetry requirements

The $\chi_{ijk}^{(2)}$ tensor that governs all second-order nonlinear optical processes is a third-rank tensor that contains 27 independent elements that correspond to lab-frame coordinates:

$$\begin{aligned}
\chi_{x}^{(2)} &= \begin{bmatrix} \chi_{xxx}^{(2)} & \chi_{xxy}^{(2)} & \chi_{xxz}^{(2)} \\ \chi_{xyx}^{(2)} & \chi_{xyy}^{(2)} & \chi_{xyz}^{(2)} \\ \chi_{xzx}^{(2)} & \chi_{xzy}^{(2)} & \chi_{xzz}^{(2)} \end{bmatrix} \\
\chi_{y}^{(2)} &= \begin{bmatrix} \chi_{yxx}^{(2)} & \chi_{yxy}^{(2)} & \chi_{yxz}^{(2)} \\ \chi_{yyx}^{(2)} & \chi_{yyy}^{(2)} & \chi_{yyz}^{(2)} \\ \chi_{yzx}^{(2)} & \chi_{yzy}^{(2)} & \chi_{yzz}^{(2)} \end{bmatrix} \\
\chi_{z}^{(2)} &= \begin{bmatrix} \chi_{zxx}^{(2)} & \chi_{zxy}^{(2)} & \chi_{zxz}^{(2)} \\ \chi_{zyx}^{(2)} & \chi_{zyy}^{(2)} & \chi_{zyz}^{(2)} \\ \chi_{zzx}^{(2)} & \chi_{zzy}^{(2)} & \chi_{zzz}^{(2)} \end{bmatrix}
\end{aligned} \tag{1.3}$$

The symmetry of $\chi_{ijk}^{(2)}$ must be identical to the symmetry of the sample. For example, if the sample is totally isotropic, all elements are equivalent by sample symmetry; therefore, all of the elements of $\chi_{ijk}^{(2)}$ must also be equivalent.

We will consider a sample that is azimuthally symmetric, meaning that it is totally isotropic with respect to rotations about the axis perpendicular to the surface plane, which we will define as the *z*-axis, but anisotropic with respect to rotations about the x and y axes. Many polymeric samples are azimuthally symmetric because the polymer can be considered to be isotropic in all directions on the surface and in the bulk, but at the surfaces and interfaces, this symmetry is broken. Because the sample has azimuthal symmetry, $\chi_{ijk}^{(2)}$ must also have azimuthal symmetry. By performing symmetry operations on $\chi_{ijk}^{(2)}$ that are allowed for the azimuthal sample, many of the tensor elements must go to zero.

Because of required symmetry about the *z*-axis, there should be symmetry with respect to 180° rotations and 90° rotations about the *z*-axis and mirror planes that include the *z*-axis. Rotating about the *z*-axis 180° requires that all of the positive values of *y* be equal to the corresponding negative values of *y* and that all of the positive values of *x* be equal to the corresponding negative values of *x*. Therefore, all elements of $\chi_{ijk}^{(2)}$ containing an odd number of either *x* or *y* in the index, such as $\chi_{xyx}^{(2)}$, $\chi_{yxx}^{(2)}$, or $\chi_{xzz}^{(2)}$ must be zero. A mirror plane including the *z*-axis requires that negative *y* values be equivalent to the corresponding positive *x* values and that positive *y* values be equivalent to the corresponding negative *x* values. This operation requires that all terms with both an *x* and a *y* in the subscript such as $\chi_{xyz}^{(2)}$ and $\chi_{zxy}^{(2)}$ go to zero. These symmetry operations leave us with

$$\begin{aligned}
\chi_x^{(2)} &= \begin{bmatrix} 0 & 0 & \chi_{xxz}^{(2)} \\ 0 & 0 & 0 \\ \chi_{xzx}^{(2)} & 0 & 0 \end{bmatrix} \\
\chi_y^{(2)} &= \begin{bmatrix} 0 & 0 & 0 \\ 0 & 0 & \chi_{yyz}^{(2)} \\ 0 & \chi_{yzy}^{(2)} & 0 \end{bmatrix} \\
\chi_z^{(2)} &= \begin{bmatrix} \chi_{zxx}^{(2)} & 0 & 0 \\ 0 & \chi_{zyy}^{(2)} & 0 \\ 0 & 0 & \chi_{zzz}^{(2)} \end{bmatrix}
\end{aligned} \tag{1.4}$$

If the sample is rotated 90° about the z-axis, the positive side of the y axis becomes the negative side of the x axis, and the positive side of the x axis becomes the negative side of the y axis. This operation serves to reduce the number of independent elements in $\chi_{ijk}^{(2)}$ to

$$\begin{aligned}
&\chi^{(2)}_{xxz} = \chi^{(2)}_{yyz} \\
&\chi^{(2)}_{xzx} = \chi^{(2)}_{yzy} \\
&\chi^{(2)}_{zxx} = \chi^{(2)}_{zyy} \\
&\chi^{(2)}_{zzz}
\end{aligned} \tag{1.5}$$

For a totally isotropic sample, a mirror plane in the *xy* plane requires that positive *z* values be equivalent to the corresponding negative *z* values. The only way this can be true is if all of the tensor elements containing an odd number of *z* terms in the index go to zero. This operation eliminates all of the remaining tensor elements in Equation (1.4), making $\chi^{(2)}_{ijk}$ equal to zero; therefore, in a totally isotropic sample no second-order nonlinear optical phenomena can occur. Under the right conditions, this property of $\chi^{(2)}_{ijk}$ gives surface and interface specificity to spectroscopic techniques relying on second-order nonlinear optical effects. If the bulk of a sample is isotropic, only molecules located in regions of the sample lacking the additional mirror plane produce signal in second-order nonlinear spectroscopic techniques; however, if the bulk is not isotropic, these techniques lose surface and interface specificity.

1.2.2 VSFG theory

I direct the rest of the discussion specifically to sum-frequency generation (SFG), in which the two input fields generate an output field with a frequency equal to the sum of the two input frequencies. In vibrational sum-frequency generation spectroscopy (VSFG), the two input fields have frequencies respectively in the visible and infrared regions. As shown in Figure 1.1, infrared photons couple with vibrational modes to promote molecules to a higher vibrational level, and the photons in the visible region provide enough energy to further promote those molecules to a virtual state of even higher energy. The relaxation of the system back to the ground state generates radiation with energy equal to the sum of the two photons used to initiate

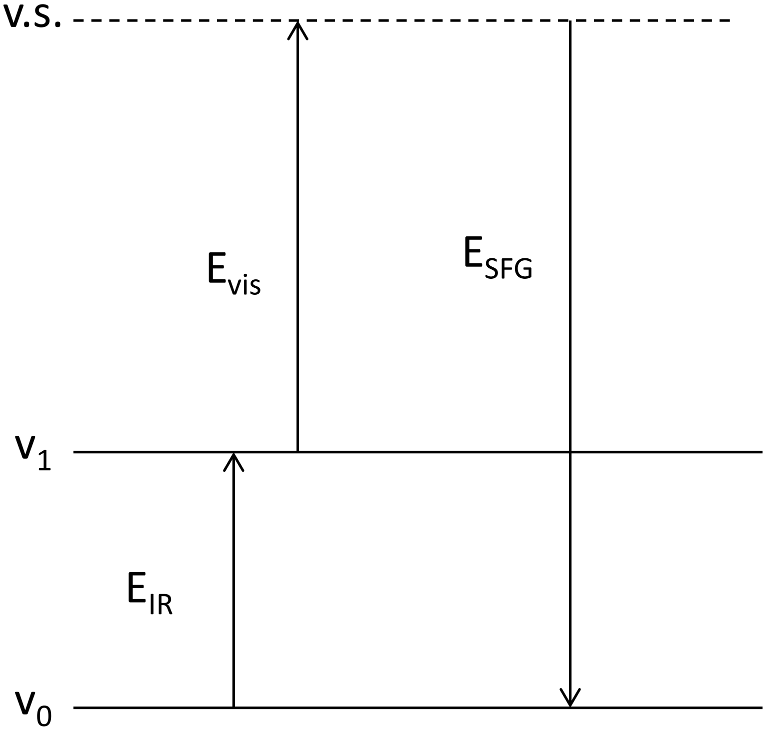

Figure 1.1 Energy diagram of the vibrationally resonant sum frequency generation process. Infrared light promotes molecules to a higher vibrational state, visible light further excites the system to a virtual state, and light is generated that has a frequency equal to the sum of the two input frequencies.

the process. This process is roughly equivalent to a simultaneous infrared and Raman anti-stokes transition, and in order for a mode to be active in VSFG, it must be both Raman and infrared active.

The non-zero elements of $\chi_{ijk}^{(2)}$ that provide surface and interface specificity in VSFG also represent the allowed polarization of the input and output beams. The index *i* corresponds to the polarization of sum-frequency signal, the index *j* corresponds to the polarization of the visible input, and the index *k* corresponds to the polarization of the infrared input. Different polarization combinations, therefore, probe different elements of the $\chi_{ijk}^{(2)}$ tensor. The *x* and *z* indices represent *p*-polarized light, and the *y* index represents *s*-polarized light. Therefore, only certain polarization combinations are allowed for a sample with azimuthal symmetry: *ssp*, *ppp*, *sps*, and *pss*. The studies included in this dissertation mostly used the *ssp* polarization combination, which collects *s*-polarized VSFG signal by overlapping an *s*-polarized visible beam and a *p*-polarized infrared beam.

1.3 VSFG Collection Methods

To generate sum frequency signal, an infrared beam and a visible beam from a laser are overlapped spatially at the sample; however, there are a variety of ways to collect this data. In this section, I summarize the most common methods used to collect VSFG data.

The first VSFG spectrometers collected spectra in the frequency domain using nanosecond laser pulses that produced input beams that were intrinsically narrow in frequency.[2] In these systems, the narrowband visible and infrared inputs are temporally overlapped to maximize the generation of sum frequency signal from the sample, which is directed into a single-channel detector. The frequency of the infrared beam is then scanned over the desired range of infrared frequencies, and the spectrum is created by plotting the intensity recorded by the single-channel detector against the center frequency of the infrared input beam. Frequency-scanning VSFG spectrometers can be purchased commercially, and are still used by several research groups.[3-10]

The studies included in this dissertation all used broadband frequency domain detection[11,12] to collect VSFG spectra. In broadband VSFG, both infrared and visible input beams come from an ultrafast pulsed laser that produces pulses that are short (~100 fs) in time and broad in frequency. In broadband systems, the infrared beam arrives at the sample as a broadband pulse to simultaneously excite all of the resonant vibrational modes of the probed molecules within the infrared envelope. A frequency-narrowed visible pulse is used to up-convert the molecular response, and all resonant frequencies within the infrared envelope are detected simultaneously using a multiplex detector.

To improve the frequency resolution in broadband VSFG experiments, the visible beam is narrowed in frequency using gratings and a slit or etalons. Narrowing the frequency profile of the visible beam lengthens the pulse in time, and different narrowing methods give different visible pulse profiles in time, even when the frequency composition of the pulses is identical. Using gratings and a slit gives the visible pulse a symmetric quasi-Gaussian profile in time, whereas using etalons gives an asymmetric visible pulse with a steep quasi-Gaussian rise at early times and a slow exponential decay at later times.[13] In the studies included in this dissertation, all spectra were collected by using etalons to narrow the frequency profile of the visible beams; the implications of this choice are discussed in Section 1.4.4.

Although VSFG data is often presented in the frequency domain with the intensity of generated signal plotted against the frequency of the infrared input, VSFG data can also be collected in the time domain.[13-15] Time domain VSFG detection is performed using ultrafast (~100 fs) pulses for both the infrared and visible input. The intensity of the VSFG signal is measured using a single-channel detector while scanning over the delay between the infrared excitation pulse and the visible up-converting pulse.

Figure 1.2 shows VSFG spectra from the C-N stretching region of acetonitrile on gold collected in both the frequency and time domain. The top panel of the figure shows the VSFG spectrum (fit two ways) collected in the frequency domain, and the bottom panel shows the signal collected in the time domain. Unlike VSFG data collected in the frequency domain, VSFG data collected in the time domain gives information about the decay of the signal over time. This data can provide structural information regarding the system being studied. Figure 1.2 illustrates that although the calculated fit in the frequency domain assuming a homogeneous distribution of adsorption sites for acetonitrile on gold was nearly identical to the fit assuming an inhomogeneous distribution, the fits in the time domain for the two distributions were distinct. The distinction between the two structural distributions enabled by time-domain measurement allowed the investigators to determine that the acetonitrile was inhomogeneously distributed on the gold surface.

In addition to differences in detecting signal in the time domain or frequency domain, VSFG detection can further be divided into homodyne and heterodyne detection. The previous descriptions of VSFG detection assumed a homodyne detection scheme in which the signal is detected directly. In VSFG, the interaction of the two input pulses with molecules within the

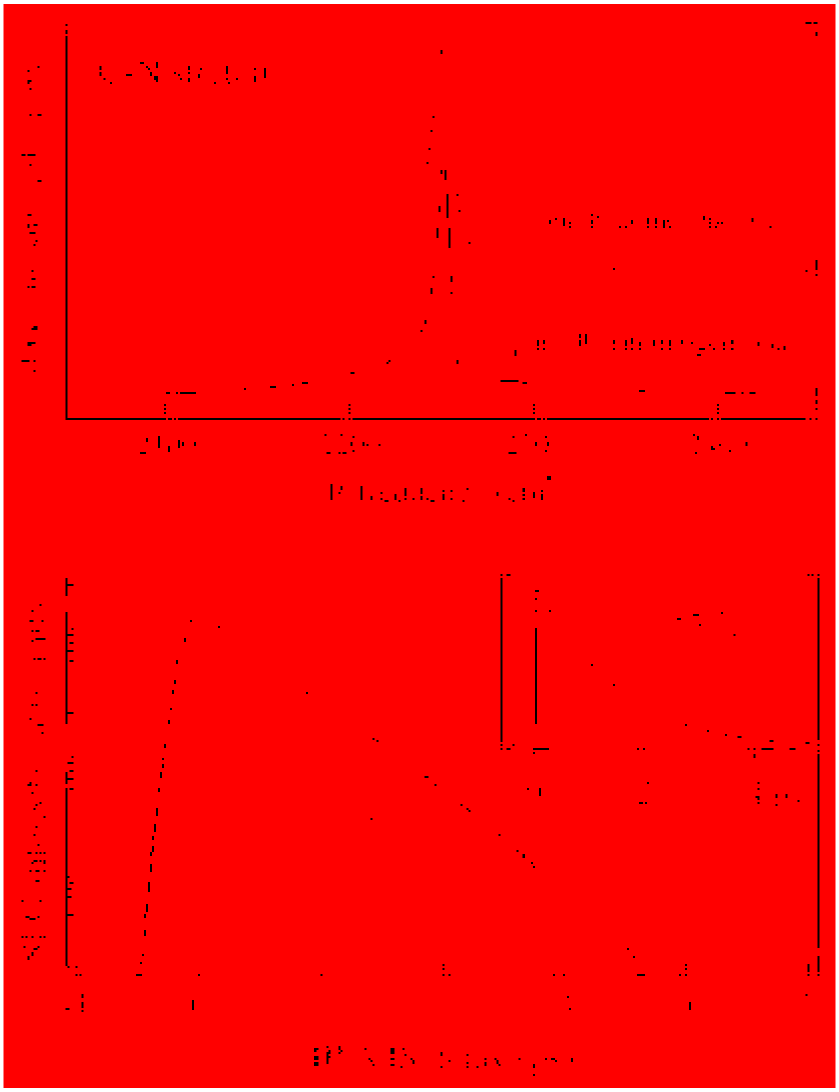

Figure 1.2 A comparison of frequency- (upper panel) and time- (lower panel) domain measurement of the VSFG signal from the C-N stretching region of acetonitrile on gold. In the upper panel, the top spectrum is fit assuming the acetonitrile adsorbs homogeneously to the gold, and the lower spectrum is fit assuming partially inhomogeneous adsorption sites. In the bottom panel, gray squares are the average of nine time-domain spectra with error bars shown. The dashed line represents the calculated time-domain signal assuming a homogeneous distribution of adsorption sites, and the solid line represents a calculation assuming an inhomogeneous distribution. Reprinted from *Chemical Physics Letters* **370** (227-232). Roke, S.; Kleyn, A.W.; Bonn, M. “Time- vs. frequency-domain femtosecond surface sum frequency generation”, Copyright (2003), with permission from Elsevier.

sample generates a complex electromagnetic field. In homodyne measurements, the signal detected is the modulus squared of that field; therefore, phase information is lost.

Heterodyne detection preserves this phase information by mixing the signal with a local oscillator (LO) prior to detection instead of detecting the modulus squared of the VSFG signal directly.[13,16-19] The detected signal is then represented by

$$\left|E_{LO}+E^{(2)}\right|^2=\left|E_{LO}\right|^2+2\left(E_{LO}*E^{(2)}\right)+\left|E^{(2)}\right|^2 \tag{1.6}$$

where E_{LO} represents the complex field of the local oscillator, and $E^{(2)}$ represents the complex field of the signal.

The desired quantity in heterodyne-detected techniques is the interference between the LO and the relatively weak signal; however, the LO intensity is often much larger than this cross-term and represents a significant source of noise in heterodyne systems, so the LO is typically removed mathematically from the data. The LO is measured separately from the heterodyned signal represented by Equation (1.6), usually by turning the signal on and off with a chopper. The modulus squared of the LO term can then be subtracted from the spectrum, leaving the cross-term and the modulus squared of the signal field; however, the signal field is significantly weaker than the cross-term and can be neglected. The LO term is then divided out of the cross-term, leaving only the complex field of the signal.

The Shen group first demonstrated heterodyne detection of VSFG signal in the frequency domain studying octadecyltrichlorosilane monolayers on fused silica. Figure 1.3 shows the modulus squared of the VSFG signal as well as the real and imaginary parts of the signal. As discussed further in Section 1.4.3, the imaginary portion (blue, bottom panel) is considered to contain all information about the resonant modes probed by VSFG. The modulus squared of the

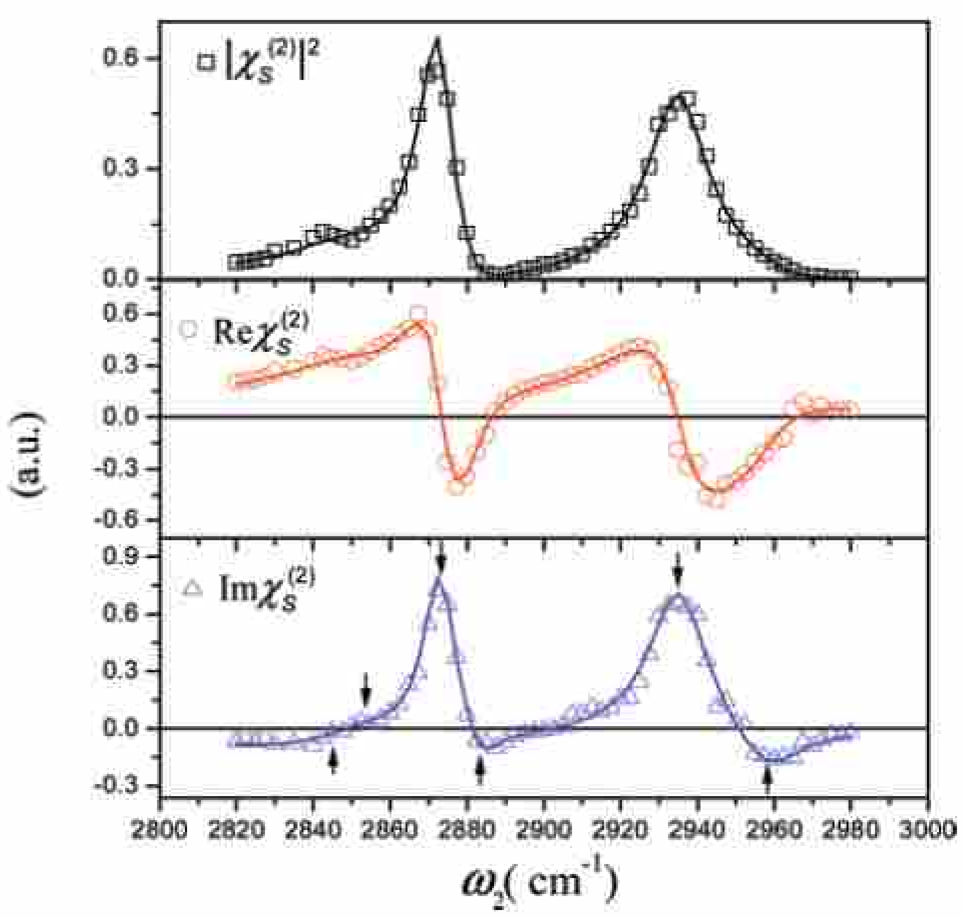

.

Figure 1.3 Heterodyne detected VSFG spectra of an octadecyltrichlorosilane monolayer on fused silica. The black squares represent the modulus squared of the signal field, the red circles represent the real portion of the signal field, and the blue triangles represent the imaginary portion of the signal field. The solid lines represent fits obtained by simultaneous fitting of the three spectra. The arrows indicate known vibrational modes of octadecyltrichlorosilane. Reprinted with permission from Ji, N.; Ostroverkhov, V.; Chen, C.-Y.; Shen, Y.-R. *J. Am. Chem. Soc.* **2007**, *129*, 10056. Copyright 2007, American Chemical Society.

signal field is shown in black in the top panel, and is analogous to the spectrum that would be detected using a homodyne detection scheme. In the imaginary portion of the signal both positive and negative peaks are apparent; however, all peaks appear positive in the modulus squared signal. The appearance of negative peaks in the imaginary portion of the signal demonstrate the ability of heterodyne detected techniques to preserve phase information.

Like homodyne detection, heterodyne detection can be used for frequency-domain measurements using either a frequency-scanning or broadband VSFG spectrometer or for measurements in the time domain. Heterodyne detection in the time domain is discussed in Section 1.4.3.

1.4 VSFG nonresonant signal

Aside from the resonant signal produced by coupling the infrared input to vibrational modes in sample molecules, VSFG also produces a nonresonant signal, generally thought to arise from a fast electronic response in the sample.[15,20] The $\chi_{ijk}^{(2)}$ tensor then becomes

$$\chi_{ijk}^{(2)} = \chi_{NR}^{(2)} + \chi_{R}^{(2)}(\omega) = \chi_{NR}^{(2)} + \sum_{R} \frac{A_R}{\omega - \omega_R + i\Gamma_R} \tag{1.7}$$

where $\chi_{NR}^{(2)}$ represents the second order hyperpolarizability of the nonresonant response, A_R represents the amplitude of a resonant peak and is related to the product of the Raman anti-Stokes and infrared transition dipole moments, ω_R represents the center frequency of a resonant peak, and Γ_R represents the width of a resonant peak. The presence of nonresonant signal complicates the analysis of VSFG data by adding more unknowns in curve fitting routines and distorting spectral lineshapes and peak positions. Below, I discuss the methods that have been used to cope with nonresonant signal.

1.4.1 Ignoring or treating nonresonant signal as negligible

Bare metallic and semiconducting materials produce significant amounts of nonresonant signal. Studies using these materials as substrates for attaching other molecules do not typically ignore nonresonant signal to extract resonant peak parameters from the VSFG data. Bare dielectric materials such as sapphire and fused silica produce no nonresonant signal, and many investigators choose to ignore nonresonant contributions when analyzing VSFG data from systems using these materials as substrates[7,8,21,22] because nonresonant signal has largely been assumed to originate only from the substrate.

The studies of model chromatographic systems performed by our group demonstrate the error of assuming the nonresonant signal is negligible when substrates are used that do not produce detectable nonresonant signal without enhancement from resonant signal.[23] In these studies, fused silica was functionalized with a model chromatographic stationary phase, and VSFG spectra of the stationary phase were collected in different solvents at ambient and elevated pressures. In one set of experiments, nonresonant signal was assumed to be negligible, and the apparent relative peak amplitudes of the two resonant peaks changed when the functionalized windows were transferred from deuterated water to deuterated methanol, but the change did not occur at elevated pressures (~900 psi); however, no changes in resonant peak amplitudes were observed in either case when nonresonant signal was removed.

Even when using substrates that do not produce nonresonant signal, the nonresonant signal from the sample could significantly change the collected spectrum. The nonresonant signal has been known to enhance the resonant signal, and this effect has been used previously to study self-assembled monolayers on gold.[24,25] In a similar manner, the resonant signal can enhance the nonresonant signal. This effect has been shown by our group for both polystyrene and silanes on fused silica.[23,26] Even when the bare substrate does not produce nonresonant signal, the resonant peaks of the material coated on the substrate can still contain nonresonant signal.

Ultimately, the consequence of ignoring the nonresonant signal is obtaining inaccurate results from data analysis. As has been shown previous by our group, the presence of nonresonant signal in spectra distorts the amplitude, center frequency, and width of the resonant peaks in unpredictable ways.[26,27] As a consequence of extracting peak parameters from distorted spectra, investigators make incorrect interpretations of the molecular orientation. This pitfall is well demonstrated by two simultaneous determinations of the molecular orientation of polystyrene thin films by VSFG published by Briggman[28] *et al.* and Gautam *et al.*[22]

Gautam *et al*. reported the orientation of phenyl rings in 160 nm polystyrene films spin-coated onto sapphire prisms at both the free and buried interface. They reported that phenyl rings at the buried interface were tilted 70° from the surface normal and that phenyl rings at the free surface were tilted 20° from the surface normal. Briggman *et al.* reported the orientation of phenyl rings on the surface of 350 nm polystyrene films spin-coated on polished silicon. With this film thickness and substrate, however, they reported a phenyl tilt angle of 57° relative to the surface normal. The two studies both claimed to report the orientation of polystyrene phenyl rings at a free surface, but the angles they reported were significantly different.

Although it has been argued that the use of different film thicknesses and substrate material could account for the differences between the two reports,[29] our group has since shown that the VSFG spectra for polystyrene are identical on both substrates and with both film thicknesses when the nonresonant signal is removed.[26] The presence of non-negligible amounts of nonresonant signal in systems using these substrates were unknown at the time of the studies by Briggman and Gautam; however, we now know that nonresonant signal cannot be ignored without acknowledging and accepting the consequences of doing so.

1.4.2 Treating nonresonant signal as a background

Rather than ignoring nonresonant signal entirely, some VSFG practitioners have treated it as a background[17] or have included it as a variable in fitting routines.[1,2,15,30-32] These studies model the signal using an expanded version of Equation (1.7):

$$\chi_{ijk}^{(2)} = \chi_{NR}^{(2)} + \chi_{R}^{(2)}(\omega) = Be^{i\phi} + \sum_{R} \frac{A_R}{\omega - \omega_R + i\Gamma_R} \tag{1.8}$$

where the term $Be^{i\phi}$ replaces the $\chi_{NR}^{(2)}$ term. The term B represents the amplitude of the nonresonant response, and ϕ is the relative phase between the resonant and nonresonant signals. These treatments of nonresonant signal either implicitly or explicitly assume that both the amplitude and the phase of the nonresonant term are independent of frequency and of the resonant spectrum. This assumption adds two more unknown parameters, nonresonant amplitude and phase, to the fitting routine. With more unknown parameters, the fit is under-constrained, and the routine produces multiple solutions that give good fits, only one of which is correct.[33] Increasing the number of good fits increases the difficulty of determining the fit that gives the correct peak parameters.

In addition to the increased difficulty in determining the most correct fit by adding unknown parameters, this fitting of nonresonant signal is inaccurate. Both the nonresonant and resonant term in Equation (1.7) are complex and can interfere with one another. The intensity of VSFG signal is directly proportional to the modulus-squared value of the $\chi_{ijk}^{(2)}$, and the signal obtained from VSFG can be expressed by expanding Equation (1.7) to

$$I_{SFG} \propto \left|\chi_{ijk}^{(2)}\right|^2 = \left|\chi_{NR}^{(2)}\right|^2 + \left|\chi_{R}^{(2)}(\omega)\right|^2 + \left|\chi_{NR}^{(2)}\right|\left|\chi_{R}^{(2)}(\omega)\right|\cos[\delta(\omega)] \quad (1.9)$$

where I_{SFG} is the intensity of VSFG signal and $\delta(\omega)$ is the frequency-dependent relative phase between the resonant and nonresonant contributions. The complex interference between resonant and nonresonant signal makes the treatment of nonresonant signal as a background to be subtracted from the overall signal unreasonable; however, the interference does not on its own rule out the possibility of including the nonresonant signal as unknown parameters in fits to experimental data.

Although the nonresonant signal is usually modeled as being frequency-independent, previous work done in our group has suggested that this assumption is not necessarily true.[27] The symmetry requirements of $\chi_{ijk}^{(2)}$ limit the generation of sum-frequency signal to regions of broken symmetry; however, these requirements do not limit the attenuation of input beams as they pass through the sample to reach the buried interface. This exception is especially true when VSFG is used to probe a buried interface, such as in adhesion studies. The vibrational modes of molecules in the surface and bulk that are resonant with frequencies in the infrared beam can attenuate the infrared beam prior to reaching the buried interface. This attenuation causes the intensity of the nonresonant signal to vary with frequency such that the nonresonant signal intensity weakens at frequencies corresponding to resonant peaks and further invalidates the assumption that the nonresonant signal can be treated purely as a background or single-valued fitting parameter. Moreover, if the nonresonant amplitude and phase terms are not assumed to be constant with frequency, more unknowns are introduced to the fits, and every additional unknown parameter reduces the uniqueness of the fits to experimental data.

The remaining methods of coping with nonresonant signal claim to completely remove nonresonant signal from experimental data. In Chapter 3 I illustrate that even spectra that appear free of nonresonant signal can still contain enough nonresonant signal to interfere significantly with a proper analysis and suggest an experimental strategy to check for the presence of nonresonant signal. With the removal of nonresonant signal, fewer assumptions must be made to extract the true resonant peak parameters that reveal orientational information about the probed molecules.

1.4.3 Time-domain heterodyne-detected VSFG

One method that has been devised to remove nonresonant signal involves heterodyne detection of the VSFG signal in the time domain. The Zanni group[13] has used this strategy to study 1,4-phenylene diisocyanide (PDI) monolayers on gold using a new system design devised by the group. The system included several improvements to previous time-domain and heterodyne VSFG designs.[15,17] Many of the new elements in the setup have to do with the phase stability of the system. Over time, the phase of the LO and sample signal can drift, and phase drift distorts measured lineshapes by changing the shape of the sample free induction decay (FID). They report that the phase stability of their system is comparable to other passively phase stabilized systems, which exhibit 6 times the phase stability over non-passively stabilized systems.

The local oscillator and the VSFG signal take the same path to the detector to eliminate phase drift in the local oscillator and visible VSFG signal. The phase of the infrared pulse does drift over time, but this change is slow, so scans can be taken for several minutes before phase drift significantly affects the signal. The slow phase drift of the infrared pulse is corrected over a series of scans by adding a constant phase term across each spectrum such that they all have the same phase as a reference before averaging.

A mid-IR pulse shaper aids in phase stabilization of the infrared pulse and fulfills several other critical requirements in the experiment. The pulse shaper corrects for the chirp that occurs by the beams passing through materials so that the infrared pulse is always transform-limited at the sample. Ensuring that the IR pulse is transform-limited at the sample allows the frequency-domain spectrum to be acquired by a Fourier transform of the time-domain data. The pulse shaper also allows shot-to-shot variation in the time delay and phase of the infrared pulse. The ability to vary the delay shot-by-shot makes the data collection significantly faster than using a mechanical stage to alter delays.

The phase cycling made possible by the pulse shaper also enables a type of balanced heterodyne detection that allows for faster collection times. By cycling the infrared phase from 0 to π, the signal and LO go in phase and out of phase with each other so the generated signals are respectively represented by

$$\left|E_{LO}+E^{(2)}\right|^2=\left|E_{LO}\right|^2+2\operatorname{Re}\left(E_{LO}*E^{(2)}\right)+\left|E^{(2)}\right|^2 \tag{1.10}$$

and

$$\left|E_{LO}-E^{(2)}\right|^2=\left|E_{LO}\right|^2-2\operatorname{Re}\left(E_{LO}*E^{(2)}\right)+\left|E^{(2)}\right|^2 \tag{1.11}$$

If either Equation (1.10) or (1.11) is subtracted from the other, the desired cross-term is the only term that remains. By collecting the data in a rotating frame instead of switching the LO on and off, data collection time is reduced by half. In addition to increasing the speed of data collection, collecting data with a phase that rotates shot-to-shot makes it possible to increase the signal to noise by averaging data over more laser shots.

The system they chose to study using their new method was also important. PDI monolayers on gold are of importance in the molecular electronics industry, but PDI monolayers have also been widely studied. The value in this study was, therefore, not in the determination of the orientation and distribution of PDI on gold, but in the demonstration of the new heterodyned time-domain VSFG method. PDI bonds heterogeneously to the gold surface, resulting in a broadening of the peak associated with CN bound to the gold surface. It has previously been shown that inherent line widths are better preserved with time-domain detection than with frequency-domain detection,[15] and the structural heterogeneity of PDI provides a good system on which to demonstrate this advantage with the new VSFG setup devised by the Zanni group.

Compared to the heterodyne detected frequency-domain measurements done by the group, the peak associated with the stretching mode of bound CNbroadened with respect to the width of the peak associated with the stretching mode of the free CN in the spectrum obtained by performing a Fourier transform on the time-domain data. This result demonstrates some advantages to collecting data in the time-domain. Theoretically, time-domain and frequency-domain detection give the same spectrum if infinitely short pulses are used in the time-domain measurements or infinitely long pulses in frequency domain measurements; however, these conditions are not met in practice.[15] The Zanni group demonstrated by simulated spectra that frequency-domain measurements always have lineshapes that are distorted by using the visible pulse as a single window function to up-convert only a portion of the vibrational response. Time domain measurements also use the visible pulse as a window function to up-convert a portion of the vibrational response, but it does so with minimal spectral distortion because the visible pulse is short compared to the decay of the vibrational response. Because the window function has a minimal effect on lineshape, the intrinsic vibrational lineshapes are measured by collecting data in the time domain.

In addition to obtaining more accurate lineshapes, collecting data in the time domain also enables the resolution to be arbitrarily increased by simply increasing the number of delays over which the data is collected, whereas in frequency-domain measurements, the spectral resolution is limited by the frequency spread of the visible pulse. Collecting in the time domain also uses a single channel detector, which can be less expensive than the dispersive optics and multiplex detectors typically used for frequency-domain VSFG experiments. In addition to the other advantages of collecting in the time domain, less laser power is needed because it does not require frequency-narrowing of the visible beam, which diminishes laser power. However, a major disadvantage of collecting in time-domain is the amount of time required to collect a spectrum. Even when using a pulse shaper rather than mechanical stage to control delays, time-domain measurements took 30 minutes each, compared to 2 minutes to measure a comparable spectrum using frequency-domain detection.

The other advantages of the technique devised by the Zanni group arise from the choice to use heterodyne detection. In the spectra collected from PDI on gold shown in Figure 1.4, the peak arising from bound CN appeared as a negative peak, and the peak arising from free CN appeared as a positive peak. The sign of the peak amplitude indicates whether the mode is pointing up or down in relation to the substrate surface. One would expect the bound CN mode to appear as a negative peak because it is pointed down, and for the free CN mode to manifest as a positive peak because it is pointed up from the gold.

This up/down orientational information is not as forthcoming in a single homodyne spectrum as it is in a spectrum collected by heterodyne detection because homodyne detection,

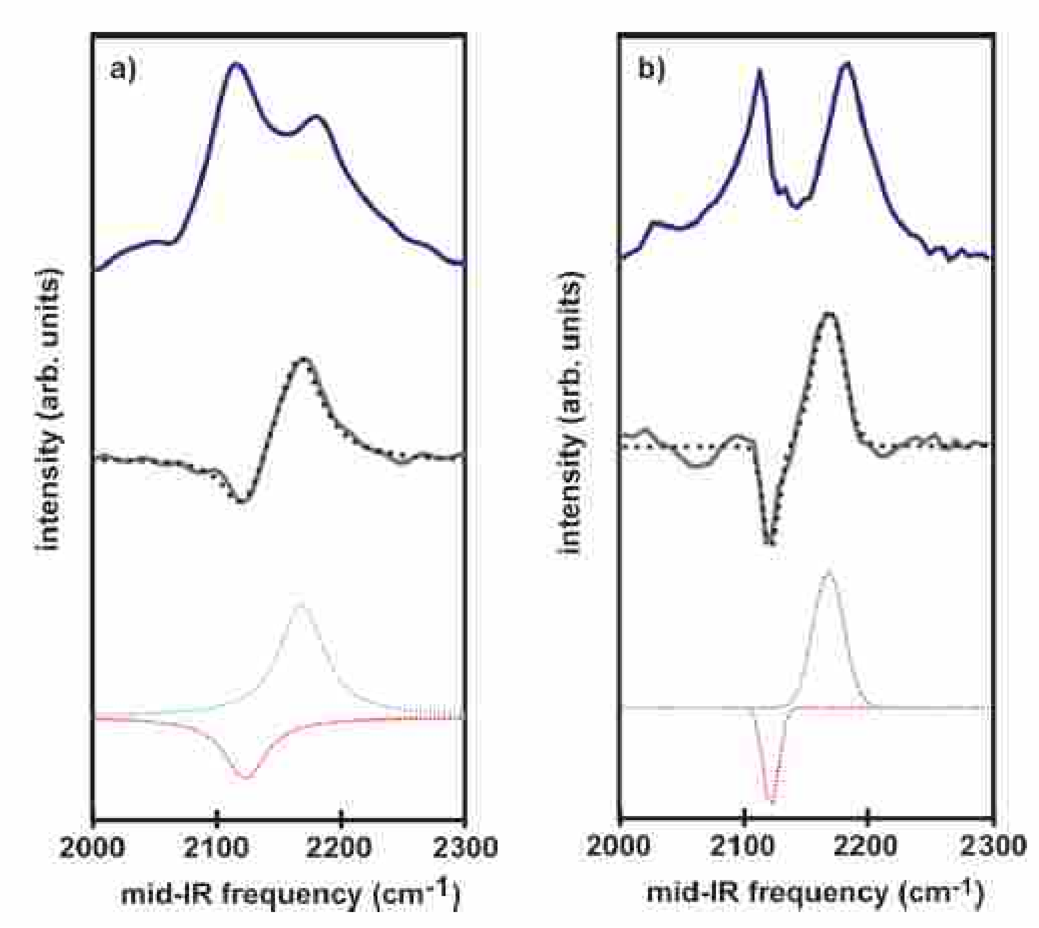

Figure 1.4 VSFG spectra of PDI on gold collected by the Zanni group using a) frequency-domain heterodyne and b) time-domain heterodyne detection schemes. The top spectra in blue are the real portion of the heterodyne spectra. The middle spectra in black are the imaginary portion of the heterodyne spectra (solid) with the fit (dotted) to the experimental data. Plotted at the bottom of the chart are the fits to the spectra decomposed into the individual peaks. Reprinted with permission from Laaser, J. E.; Xiong, W.; Zanni, M. T. J. Phys. Chem. B. 2011, 115, 2536. Copyright ©2011, American Chemical Society.

even in the time domain, measures only the square magnitude of the complex field associated with the signal. Figure 1.5 shows spectra collected using heterodyne detection with different carrier frequencies and compares those spectra to a spectrum collected using homodyne detection. Another consequence of measuring the square magnitude shown in Figure 1.5 is that oscillations in time necessary to obtain the frequency-domain VSFG spectrum from a Fourier transform are not seen in homodyne time domain detection schemes.

The Zanni group also claims that heterodyne detection allows the removal of nonresonant signal by allowing the separation of the signal into its real and imaginary parts. They claim that the nonresonant signal only appears in the real part of the spectrum, and that the imaginary part of the spectrum represents the pure resonant response. In the spectra of PDI on gold from Figure 1.4, the real portion of both the spectrum collected in the time domain and the spectrum collected in the frequency domain displays dispersive lineshapes in the resonant peaks on top of a broad nonresonant pedestal. Dispersive lineshapes and a broad pedestal are typical of VSFG spectra containing nonresonant contributions, and they interpreted the lack of these indicators in the imaginary portion of the PDI spectra as evidence that the imaginary portion did not contain nonresonant signal.

1.4.4 Nonresonant suppression by visible pulse delay and variable time delay VSFG

Lagutchev *et al.* [34] demonstrated that nonresonant signal in VSFG can be suppressed by delaying the visible upconverting pulse relative to the visible excitation pulse. One important feature in this demonstration of nonresonant suppression was the use of etalons to frequency-narrow the visible pulse. The sharp rise and slow decay of the time profile imparted by the use of etalons provides an ideal pulse shape for this nonresonant suppression. The sharp rise avoids the up-conversion of nonresonant signal while the slow decay enables the up-conversion of a large

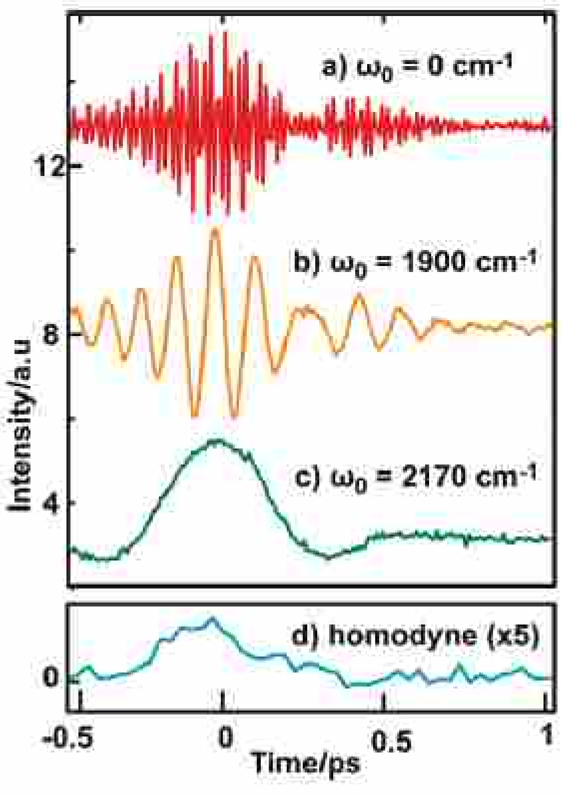

Figure 1.5 VSFG spectra of PDI on gold collected in the time domain by the Zanni group using a rotating frame frequency of a) 0 cm^{-1}, b) 1900 cm^{-1} c) 2170 cm^{-1}. The time-domain spectrum d) was collected using homodyne detection for comparison. Reprinted with permission from Laaser, J. E.; Xiong, W.; Zanni, M. T. *J. Phys. Chem. B*. **2011**, 115, 2536. Copyright 2011, American Chemical Society.

portion of the resonant response decay. Using this method increases the symmetry and resolution of resonant peaks,[35] and with sufficient delay between the excitation and up-conversion pulse, can be used to completely remove nonresonant signal. Unfortunately, suppressing the nonresonant signal in this way also distorts the appearance of resonant peaks in spectra.

The Benderskii group[32] showed that delaying the visible up-converting pulse relative to the infrared excitation pulse to suppress nonresonant signal can cause apparent phase shifts in the observed vibrational modes. Although the group used a homodyne detection scheme, VSFG with incompletely suppressed nonresonant signal is similar to a heterodyne technique. Comparing Equations (1.6) and (1.9), we see that the cross-term in Equation (1.9) containing both the nonresonant signal and the resonant signal is analogous to the cross-term in Equation (1.6) containing the local oscillator and sample signal. In samples that produce a strong nonresonant signal from the substrate, measuring the phase of the resonant signal relative to the phase of the nonresonant "background" by fitting to Equation (1.8) is a standard practice, and the Benderskii group fit the data obtained in this study to that model.

The Benderskii group used a broadband homodyne VSFG system to study methyl-terminated Si(111), CH_3-Si(111). As discussed further in Chapter 3, the surface of Si(111) has 3-fold azimuthal rotational anisotropy, which causes the nonresonant signal from the substrate to be periodic with respect to rotations. To collect the spectra in this study, they rotated the samples to maximize this substrate nonresonant response, and with the substrate nonresonant response dominating the spectra, the resonant peaks from the methyl groups appear as peaks or dips on the nonresonant pedestal. They frequency-narrowed the visible beam profile with an etalon, and collected VSFG spectra with full nonresonant contribution at the maximum overlap between the infrared and visible pulses (t=0) and with the visible pulse delayed (t=300 fs) to partially suppress the nonresonant signal.

The VSFG spectra of methyl-terminated Si(111) contain two resonant peaks corresponding to a methyl symmetric stretch at ~2907 cm^{-1} and a methyl asymmetric stretch at ~2979 cm^{-1}. Figure 1.6 shows that at zero delay between the two pulses, the nonresonant response is fit as a strong, broad, Gaussian peak, and both peaks appear as dips on this pedestal. When the delay between pulses is increased to 300 fs, however, the methyl symmetric stretch at ~2907 cm^{-1} becomes a negative dip relative to the phase of the nonresonant signal. The frequency and time profile of both pulses remain unchanged through the experiment, with variation only in the delay between them; therefore, the apparent phase "flip" observed in Figure 1.6 is caused only by the delay between the pulses.

The apparent phase flip that occurs in the nonresonant-suppressed VSFG spectra of methyl-terminated silicon results from the two peaks being in phase during some portions of the resonant response decay, and out of phase during other portions. Whenever there are two or more resonant peaks in a spectrum, they cause beats in the time domain response. The two resonances initially oscillate in phase, but if the lifetime of the mode is comparable to or greater than the frequency difference between the two modes according to Equation (1.12), the modes go in and out of phase during the decay of the resonant response.

$$t \geq \frac{1}{\Delta\omega_0} \tag{1.12}$$

In Equation (1.12), t represents the time delay of the visible pulse relative to the infrared pulse, and $\Delta\omega_0$ represents the offset of the two center frequencies of the modes.

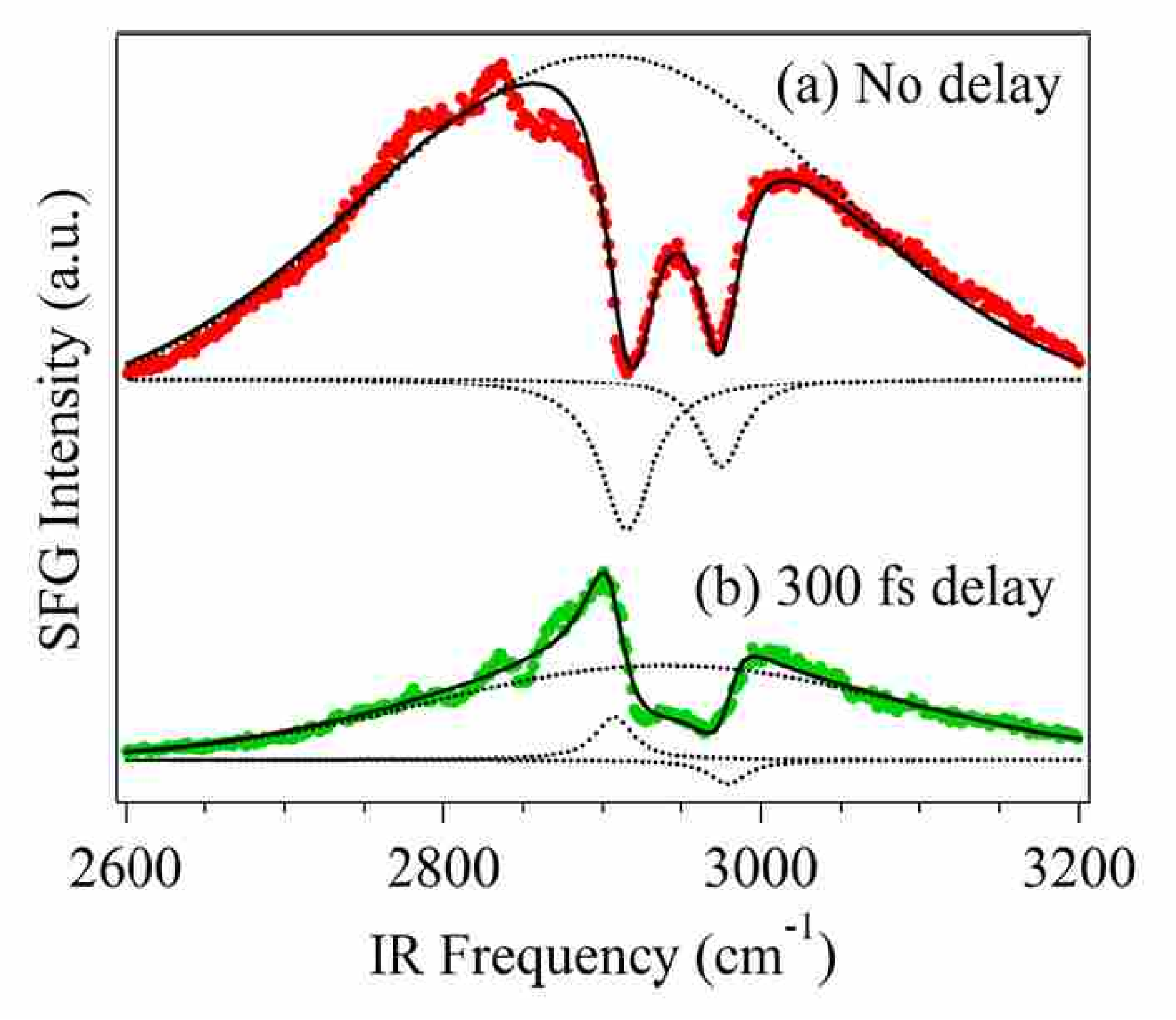

Figure 1.6 Experimental VSFG spectra of methyl terminated Si(111) using an etalon-narrowed visible pulse delayed with respect to the infrared pulse by (a) 0 fs and (b) 300 fs. The solid black line shows the fits obtained by fitting to Equation (1.8), and the dotted lines show the three fitting components in each fit. The spectrum in (a) shows two negative peaks, and the spectrum in (b) shows a positive peak and a negative peak. Reprinted with permission from Shalhout, F. Y.; Malyk, S.; Benderskii, A. V. *J. Phys. Chem. Lett.* **2012**, *3*, 3493. Copyright 2012, American Chemical Society.

In the case of the symmetric and asymmetric methyl stretches of methyl-terminated silicon, the 300 fs delay represents a time in the resonant vibrational response that is approximately one-half the period of the oscillation in the relative phases of the two modes. When the visible pulse overlaps with this portion of the resonant response decay, it up-converts only the part of the spectrum in which the two modes are out of phase. This study highlights the importance of obtaining time-domain vibrational information from the sample in addition to the frequency-domain information.

The variable time delay method of collecting and analyzing VSFG data developed in our group by Alexander Curtis[36] balances time-domain and frequency-domain data acquisition while it also compensates for the distortions caused by suppressing the nonresonant signal, overcomes spectral congestion, eliminates nonresonant signal, and aids in obtaining unique fits to spectral data. This method is essentially a hybrid of time-domain and frequency-domain data collection strategies. All data are collected in the frequency domain, but over multiple time delays after complete suppression of nonresonant signal. The spectra collected are different from each other because they sample different portions of the FID, and this provides multiple data points with which to constrain the parameters of the nonlinear curve fitting, which is performed on all spectra simultaneously.

Data are collected using a femtosecond infrared pulse and a visible pulse that is frequency-narrowed using etalons to give the upconverting pulse the desired sharp rise and exponential decay in time, as discussed above. Time zero is set at the timing of the visible pulse that gives the maximum nonresonant signal off of a bare gold mirror. To collect sample data, the visible pulse is delayed relative to the infrared pulse using a mechanical stage until the nonresonant signal is completely suppressed.[34] The minimum time delay to remove nonresonant signal is approximated by the point at which the signal is free of the broad pedestal and dispersive lineshapes typical of signal containing nonresonant signal. If this amount of delay is insufficient to entirely remove nonresonant signal, the subsequent fitting routine fails, and a later point can be chosen by trial and error. Spectra are collected in the frequency domain using a CCD camera from multiple delays of the visible upconverting pulse. A number of spectra equal to the number of resonant peaks are selected and fit simultaneously to the same set of resonant peak parameters. A set of five spectra collected by the variable time delay method are shown in Figure 1.7 with the results of simultaneous fitting shown in red and the delay of the infrared pulse relative to the visible pulse reported in the inset of each spectrum.

This method of suppression can be used to completely remove nonresonant signal, but also distorts the observed vibrational lineshapes[26,27,32] and introduces a frequency-dependent phase shift in the resonant response.[13,32] One argument for using the heterodyne detection method devised by the Zanni group rather than the variable time delay method is that the Zanni method removes nonresonant signal without apodizing the free induction decay of the vibrational response. However, some apodization of the FID always occurs in frequency domain measurements, regardless of whether nonresonant signal is included or not. The upconverting pulse either undersamples the early portions of the FID containing information about peak areas or the latter portion responsible for peak resolution; therefore, the spectra are always distorted in frequency-domain measurements. The variable time domain method uses this distortion as an advantage. Although the distortions to the spectra are different at each delay, the underlying free induction decay of the vibrational response is unchanged by delaying the visible pulse.

The set of spectra obtained by sampling multiple portions of the same free induction decay are essentially a set of linearly independent equations with the same set of unknown

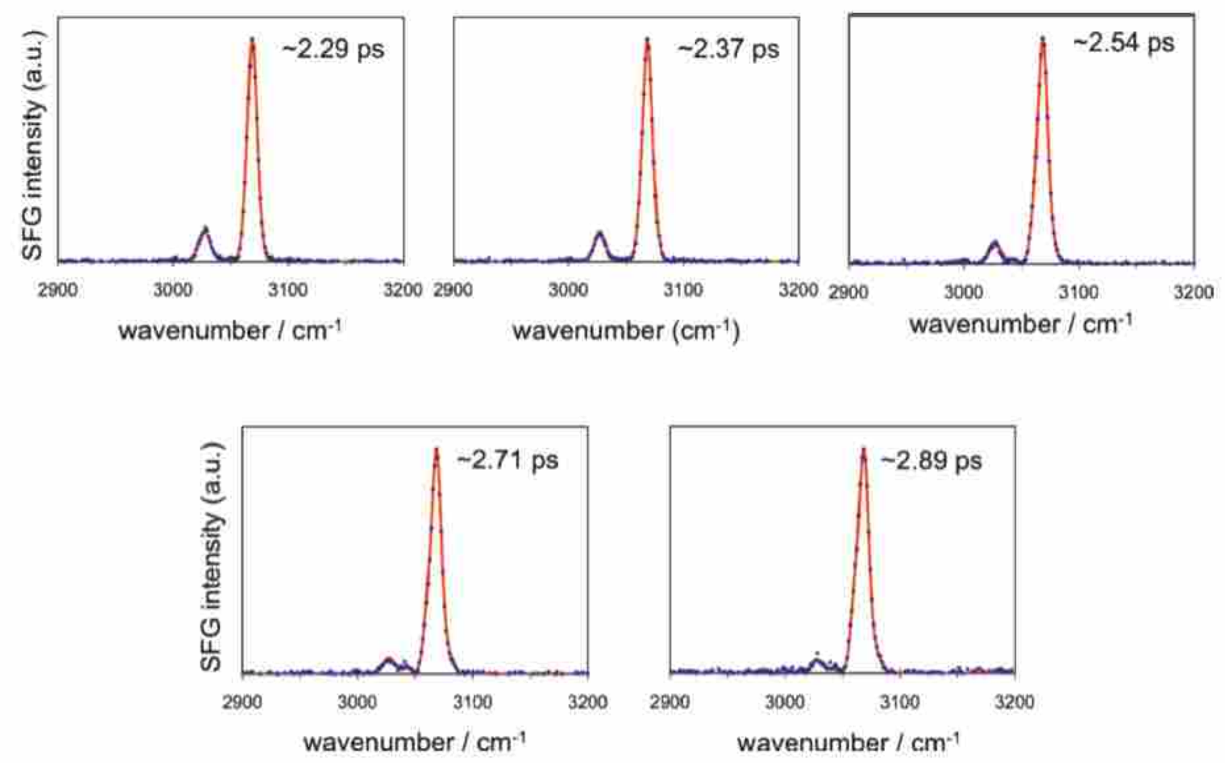

Figure 1.7 Polystyrene spectra collected with various delays of the infrared pulse with respect to the visible pulse using the variable time delay method. Experimental data points are shown in blue, the results of simultaneous fitting are shown in red, and the approximate delay in picoseconds (ps) is inset in each spectrum. Reprinted with permission from Curtis, A. D.; Asplund, M. C.; Patterson, J. E. J. Phys. Chem. C 2011, 115, 19303. Copyright 2011, American Chemical Society.

parameters, providing the constraints necessary to obtain meaningful parameters from nonlinear curve-fitting. Nonlinear curve fitting of vibrational lineshapes is difficult unless peak parameters are sufficiently constrained to obtain a unique fit.[33] VSFG often probes different regions of the sample than bulk techniques because of the symmetry requirements on $\chi_{ijk}^{(2)}$, so peak parameters are not necessarily known *a priori*, even when the system is well-studied using bulk spectroscopic techniques. Just as adding nonresonant parameters to fitting increases the number of solutions, adding constraints to resonant parameters by fitting simultaneously to a system of linearly independent data points decreases the number of solutions obtained through nonlinear curve-fitting.

Another factor in proper curve-fitting of data is fitting to the correct number of peaks; although too few peaks gives a poor fit, using too many peaks causes the fit to lose physical meaning. This advantage of the variable time delay method was demonstrated by using the method to analyze spectra of octadecyltrichlorosilane on fused silica. If the delay of the visible pulse is adjusted to maximize VSFG signal, the spectra contain two well-resolved peaks at 2945 cm^{-1} and 2880 cm^{-1}; however, variable time delay analysis revealed that the peaks at 2945 cm^{-1} is actually composed of at least two peaks, as shown in Figure 1.8. These two peaks at 2920-2930 cm^{-1} and 2945 cm^{-1} are respectively attributed to the methyl antisymmetric stretch and the Fermi resonance between the methyl symmetric bend and stretch. Likewise, previous reports fit the peak at 2880 cm^{-1} to two neighboring resonant features, but in variable time delay analysis, no neighboring peak ever appeared in the spectra at any delay.

In addition to the ability to determine the correct number of resonant peaks, the variable time delay method also provides information about how the frequency composition of the signal evolves in the time domain. A similar technique is used to create heat map spectrograms of audio

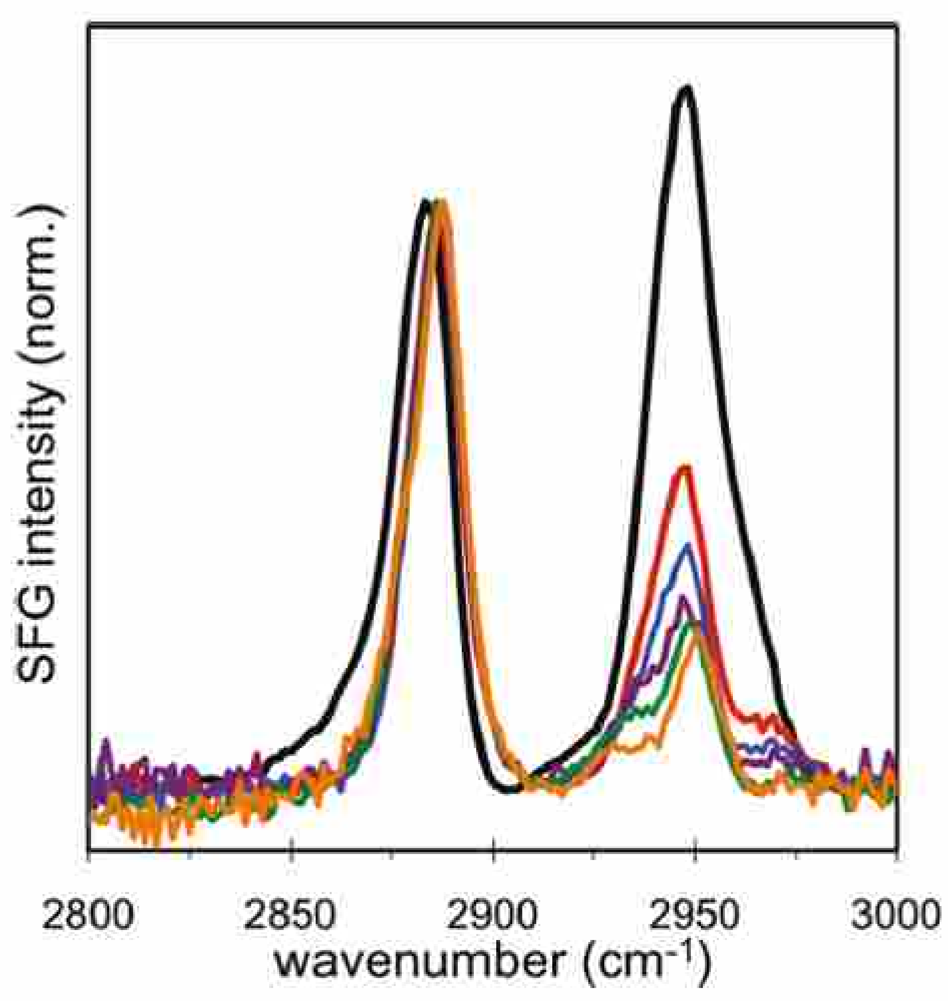

Figure 1.8 VSFG spectra of octadecyltrichlorosilane on fused silica collected using the variable time delay method. The spectra were collected using delay times of (black) 0 ps; (red) 1.86 ps; (blue) 2.04 ps; (purple) 2.20 ps; (green) 2.20 ps; (orange) 2.54 ps. The spectra were scaled such that the peak at 2880 cm^{-1} had the same amplitude in each spectrum. Reprinted with permission from Curtis, A. D.; Asplund, M. C.; Patterson, J. E. J. Phys. Chem. C 2011, 115, 19303. Copyright 2011, American Chemical Society.

signals that map the intensity of various frequencies present in the signal over time. Audio signals are recorded in the time domain, and the spectrogram analysis is performed as a post-processing step. A window function is used to apodize the time-domain signal in overlapping sections, and each apodized section is then transformed into the frequency domain to create the spectrogram. In the variable time domain technique, the time domain signal is the free induction decay of the resonant vibrational response, and the temporal profile of the upconverting pulse acts as a window function. Figure 1.9 illustrates this process using a simulated resonant polystyrene spectrum and the temporal profile of the visible pulse shaped by etalons. The Fourier transform in the variable time delay method occurs as a result of detection in the frequency domain.

Like spectrogram analysis, the variable time delay method presents data that allows the user to easily observe how the frequency composition of the signal evolves with time. This unique advantage of the variable time delay technique was demonstrated by the observation of the temporal behavior of the peak at 2945 cm^{-1} in octadecyltrichlorosilane on fused silica. The relative intensity of the Fermi resonance peak changed significantly with changes in the delay between the infrared and visible pulses. This sensitivity to delay further confirmed that the peak at 2945 cm^{-1} arises from a Fermi resonance because Fermi resonances tend to have shorter lifetimes than peak widths would suggest, and thus dephase quickly.

The variable time delay method also aids in discerning peaks in congested spectra. Variable time delay analysis of polystyrene showed that there is a weak, narrow peak at 3045 cm^{-1} but no peak at 3035 cm^{-1}, whereas a previous study fit a broad negative peak at 3035 cm^{-1} but no peak at 3045 cm^{-1}.[28] Although the appearance of a negative peak at 3035 cm^{-1} was probably due to the nonresonant signal present in that study, the 3045 cm^{-1} usually does not

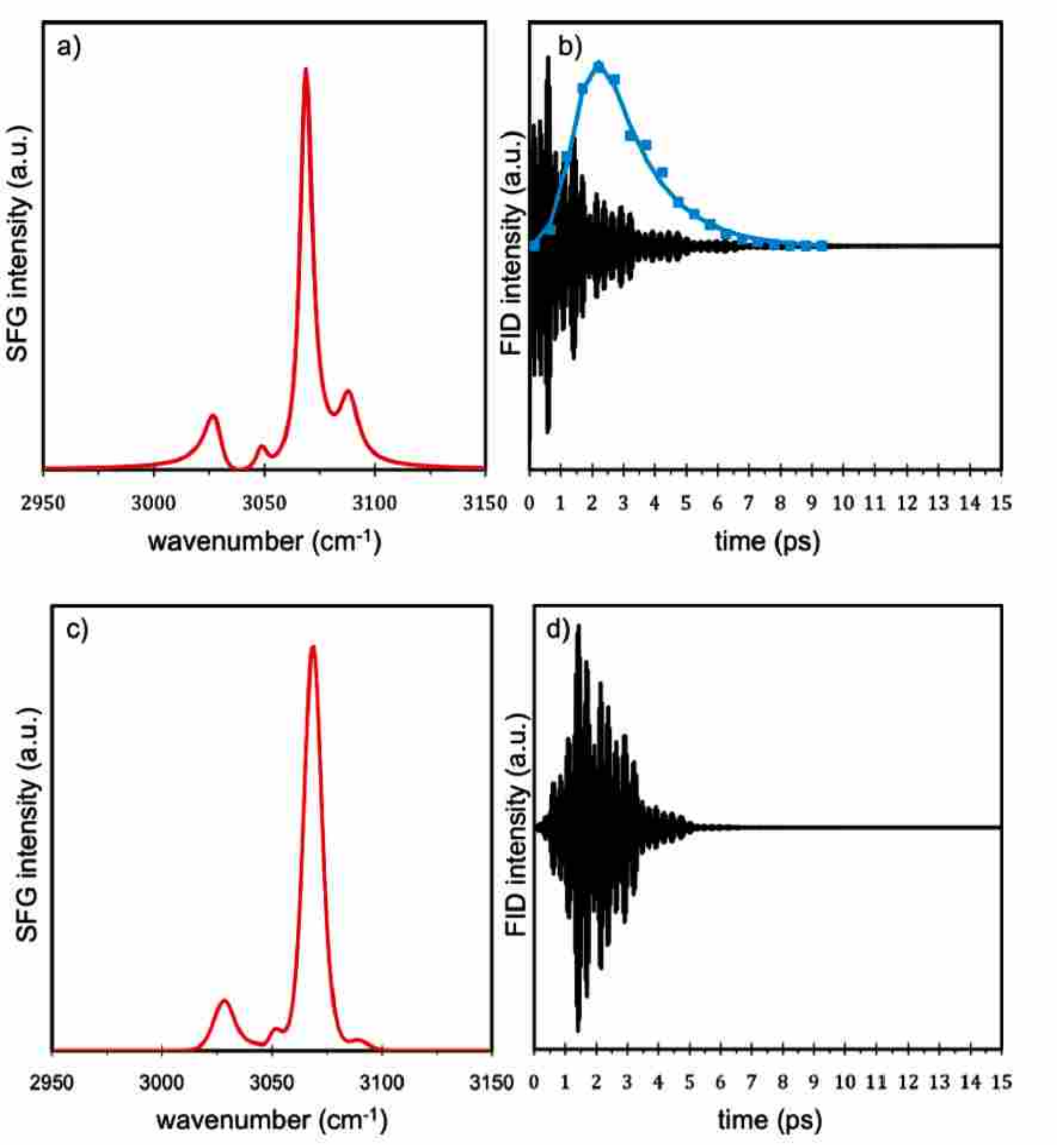

Figure 1.9 The effects of apodization on the purely resonant VSFG spectrum of polystyrene. a) Simulated purely resonant VSFG spectrum of polystyrene. b) The inverse Fourier transform of the simulated spectrum (black) with the temporal profile of the visible pulse (blue) acting as a window function. c)A representation of the frequency composition of the apodized signal. d) The portion of the free induction decay upconverted by the visible pulse profile. Reprinted with permission from Curtis, A. D.; Burt, S. R.; Calchera, A. R.; Patterson, J. E. *The Journal of Physical Chemistry C* **2011**, *115*, 11550. Copyright 2011, American Chemical Society.

appear in spectra, even with the nonresonant signal suppressed, because of interference with the nearby peak at 3057 cm^{-1}. This method allows the inherently narrow, weak peak at 3045 cm^{-1} to appear by broadening it and diminishing the amplitude of the interfering 3057 cm^{-1} peak. Although apodization broadens all peaks, inherently broad peaks with shorter lifetimes are diminished at the longer delays, and spectral congestion is decreased while narrow peaks are broadened, enhancing the ability to detect them.

1.4.5 Summary of methods for coping with nonresonant signal

Given that nonresonant signal can neither be ignored nor treated as a background, we must consider the advantages and disadvantages of each technique proposed to eliminate it as they pertain to the study of adhesion. The heterodyne time domain detection method does not require any assumptions of lineshape and as a result is able to maintain the intrinsic vibrational lineshapes in the spectra. In contrast, the variable time delay method assumes well-behaved Lorentzian lineshapes to obtain the simultaneous fits, and so intrinsic vibrational lineshape is lost.

Another disadvantage of the variable time delay method is that absolute peak amplitude and phase are also lost. The required temporal suppression of the nonresonant signal removes the beginning points of the FID that are necessary to determine absolute peak amplitudes; however, relative amplitudes are sufficient to determine molecular orientation when the molecule has two vibrational modes with orthogonal dipole moments.[28,37] The absolute phase of peaks is also lost in the variable time delay method as described, whereas it is preserved in the heterodyne time domain detection method; however, phase sensitivity in the Zanni experiment comes from the heterodyne detection, and thus phase determination is also possible with the variable time delay method if a heterodyne detection scheme is employed.

One significant drawback of both techniques is the amount of time required to collect the data and perform the analyses. In spite of the many improvements made to both time-domain and heterodyne detection schemes incorporated into the heterodyne time domain detection scheme reported by the Zanni group, the collection of a time-domain spectrum took thirty minutes to acquire, compared with the two minutes required to collect a frequency-domain spectrum. The variable time delay method requires at minimum twelve minutes to collect the data necessary for analysis because it takes approximately two minutes to collect a single spectrum with sufficient signal to noise after a two minute background, and spectra must be collected from multiple delays to perform the analysis. Realistically, data collection takes significantly longer because the correct time delays to provide linearly independent data points for fitting are not usually known prior to the experiment.

Secondly, neither method can be performed using the picosecond or nanosecond pulsed laser sources commonly employed in frequency-scanning systems. The longer pulses do not provide the temporal resolution necessary for the Zanni method, and because the infrared pulse is relatively long, it constantly pumps the nonresonant response and prohibits the use of visible pulse delays to suppress the nonresonant signal in the variable time delay method. However, so far no work has come forward demonstrating the successful removal of nonresonant signal from VSFG spectra using a frequency-scanning system.

Both of these methods are also less than ideal for use during dynamic adhesion experiments or during any observation of changes over time unless those changes are known to occur slowly relative to collection time. In this regard, the variable time domain approach is preferable because the collection of multiple spectra is only necessary once for each system, whereas the full treatment must be performed for each heterodyne time domain experiment.

Once peak parameters are obtained for each system to constrain the analysis of future spectra by simultaneously fitting spectra from multiple delays, the rest of the spectra can be collected from a single delay. Although collecting data from a single delay distorts each spectrum, it distorts all spectra the same way, so changes in spectra collected from the same time delay relate to changes in molecular orientation.

Another advantage of the variable time domain method is that no assumptions are made concerning the nonresonant signal because with the constraints added by collecting multiple spectra, it must be completely removed experimentally in order to obtain good fits to the data. Although compete removal of nonresonant signal using the heterodyne time-domain detection method seems like a straightforward and convenient way to determine the pure resonant response of probed molecules, doing so requires the assumption that the nonresonant response is symmetric about the point t=0, or in other words, that it is instantaneous.[13,15,17] However, we have shown previously that the temporal response of the nonresonant signal is not identical on all substrates and can also be affected by adding coatings to the substrate.[27] Because of the dependence of the temporal response of the nonresonant signal on substrate material and the identity and thickness of coatings, the assumption of an instantaneous nonresonant response may not be valid for anything other than monolayers. In fact, since the date of the publication reporting this method in 2011, this group has yet to demonstrate the use of heterodyne time-domain method to study any systems other than PDI on gold.

The variable time delay method offers several other advantages over the heterodyne time detection method. It is relatively inexpensive in that it uses etalons as a means of providing the proper pulse shape, which many systems already have in place. In contrast, the heterodyne time detection method requires the use of a pulse shaper, which represents a significant expense.

Additional advantages of the variable time delay not offered by the heterodyne time detection method are that it gives uniqueness to structural determinations by obtaining multiple data points to fit simultaneously, allows observation of the temporal evolution of vibrational frequencies, and diminishes spectral congestion.

1.5 Studying functional adhesives using VSFG

These recent improvements in VSFG methodology and spectral analysis have prepared the way to use the technique to study functional adhesives; however, we are not the first to attempt such a study. Wilson *et al.*[38] at NIST previously performed VSFG studies to determine the connection between interfacial structure and adhesive strength of polystyrene thin films on spin-on glass (SOG). In these experiments, the substrate was a gold mirror with SOG of various thicknesses that was later coated with a polystyrene thin film. They reported the orientation of polystyrene at what they thought was the buried interface for two different treatments of the SOG. SOG is natively hydrophobic because the surface is Si-H terminated, and one treatment was to coat the polystyrene directly onto this hydrophobic surface.

To make the SOG hydrophilic, they treated it with ultraviolet light and ozone, which converted some of the surface Si-H to Si-OH. They confirmed that the surface conversion was complete enough to change the hydrophilicity by water contact angle measurement. Through atomic force microscopy measurements of surface RMS roughness and FTIR spectroscopy before and after the treatment, they ensured that RMS roughness and bulk composition remained unchanged by the treatment.

The adhesive strength of the polystyrene films were tested qualitatively using a 90° peel test. In this test, a piece of adhesive tape is applied to the surface of the coating and removed at a 90° angle from the surface. If the coating is removed by the tape, it fails the peel test, and if it remains after peeling the tape, it passes the peel test. It was found that the polystyrene coating on the hydrophilic surface passed the peel test, whereas the coating on the hydrophobic surface failed. The VSFG data was collected separately from the peel tests, and the orientation of polystyrene at the buried interface with the two different substrate surfaces was determined in an attempt to explain the difference in adhesive behavior.

Previous to the Wilson study, no attempt to provide a molecular explanation for the macroscopic behavior of a functional adhesive using VSFG had yet been made. However, this study was not without its flaws. The VSFG data and adhesion data were collected separately, so the experiments did not provide any information about what orientation changes occurred as the adhesion between the polystyrene films and the SOG substrates failed. Additionally, the peel test gives only qualitative data about adhesion, and does not give detailed information about the amount of force that is applied to cause the adhesive to fail in each test.

In addition to the drawback of providing limited information regarding the correlation between the spectral response and adhesive strength of the sample, at the time of this study, many aspects regarding the analysis of VSFG data and the surface and interfacial orientation of polystyrene still remained unresolved. At the time, the importance of the elimination or suppression of nonresonant signal was yet unappreciated, and as a result, all of the spectra in the study contained large amounts of nonresonant signal. Because of the large amounts of nonresonant signal present, the analysis of the VSFG data was unnecessarily complicated.

To isolate signal from the buried interface, they used the multiple interference method they developed.[39] In this method, they claimed to be able to selectively probe either the free surface or buried interface by changing the thickness of the SOG layer between the polymer thin film being studied and a gold mirror. They fit the spectra using five peaks for the resonant normal modes of polystyrene and two combination modes for both the buried interface and the polystyrene/air interface. To determine the molecular orientation of polystyrene, they used the relative amplitudes of the polystyrene peaks obtained from this fitting, as set forth previously by Briggman *et al.*[28] They report a phenyl tilt angle of 60° from the surface normal for polystyrene on untreated SOG.

Although they had success with fitting the spectra of polystyrene on untreated SOG, they were unable to obtain good fits for polystyrene on the UV-ozone treated SOG using the Briggman model. They attributed this difficulty to an assumption in the model that the relative amplitudes of the peaks in a spectrum are independent of the torsional angle between the phenyl rings and the polystyrene backbone. Using isopropylbenzene in density functional theory (DFT) calculations, they determined that the torsional angle does influence the relative amplitudes of peaks. After adding torsional angle as a fitting parameter, they were able to obtain good fits, and reported that on the UV-ozone treated SOG, polystyrene phenyl rings tilt 50° from the surface normal with a 30° torsional angle from the polymer backbone.

The Chen group[8,10] has studied adhesion between various polymers and epoxy materials used in flip-chip underfills in several studies. The VSFG was performed using a frequency-scanning system to study the interface between the polymer and the epoxy. In order to enhance VSFG signal, a right angle prism was used as a substrate for the polymer; the polymer was first coated onto the substrate, and that coating was bonded to the epoxy. The two polymers studied, poly(ethylene glycol terephthalate) (PET) and polystyrene, were deuterated to eliminate the detection of C-H stretching modes at the buried polymer/substrate interface.

Adhesive strength was tested by measuring the force on the adhesive bond and displacement during a shear test modified from the ASTM D3163 Standard. The VSFG spectroscopy and adhesive strength measurements were again performed separately in the Chen studies as well. In the shear test, the epoxy was applied between two sheets of either polystyrene or PET, and the two sheets were pulled in opposite directions parallel to the plane of attachment. They reported that the failure of the bond occurred at the interface between the epoxy and the polymer in every trial; therefore, the strength test results correlate to the strength of the adhesive bond. This test enabled better quantification of adhesive strength compared to the earlier study by Wilson *et al*.

In some samples, small amounts (1.5%) of various silanes were added to the epoxy prior to curing. The introduction of silanes into the epoxy greatly impacted the observed VSFG spectrum, and by extension, the interfacial molecular orientation. In some of the epoxy/silane combinations, the addition of silanes caused the VSFG interfacial signal to decrease compared to the native epoxy. This loss in signal was interpreted as increased disorder at the interface because a preferred orientation is required for the generation of sum-frequency signal. The more disordered interfaces corresponded to samples with strong adhesive strength in the mechanical strength testing measurements, and they explained that the disordered structure enables more entanglements to occur between molecular chains, resulting in stronger interfacial adhesion.

These pioneering studies by Wilson and Chen clearly demonstrated the viability of using VSFG data to correlate adhesive behavior with molecular response from the interface. We intend to improve further upon this previous study by using recent discoveries about the nonresonant signal and methods for removing it to collect data. We can obtain this data at various stages of adhesive failure and quantitatively measure the load on the adhesive bond by coupling the VSFG spectrometer with a commercial strength tester and collecting spectral and strength data simultaneously.

1.6 My role

None of the work done in our group is without collaboration, and I have striven in this dissertation to give credit to all of the people who have contributed to the chapters herein. Likewise, I wish to acknowledge the contributions I have made to the works cited in this introductory chapter but not included in this work. I was involved in many discussions regarding the effects of nonresonant signal on VSFG spectra and the limitations that the presence of nonresonant signal causes in spectral analysis that led to the publication of two of the papers referenced.[26,27] I also designed the spin-coating programs to give quality coatings, determined the proper concentration of the polymer solutions to make the different thicknesses necessary for the comparisons, and made all of the samples. In addition to preparing sample coatings of the proper thickness on multiple substrates, I also developed the annealing procedure that was used and carried out the annealing of the polymer films in both studies.

Particularly on the paper titled "Limitations in the Analysis of Vibrational Sum-Frequency Spectra Arising from the Nonresonant Contribution," I contributed significantly to the actual writing of the papers. Alexander Curtis wrote the initial ideas to communicate in the paper and discussed them with me, and I helped flesh out the ideas and express them in an organized and coherent fashion. Aside from these more significant contributions, I also participated in the revision process, including assisting in gathering additional data and formulating responses to reviewer comments.

A publication by Alexander Curtis reporting the sub-surface phenyl rings of polystyrene and updating the mode assignments for VSFG spectra of polystyrene[37] was also enabled by the plasma treatment paper included as Chapter 4 in this work. The two papers were essentially written together, with each of us contributing significantly to both papers through frequent collaboration. It took nearly two years for the paper reporting the detection of bulk phenyl rings using VSFG to be accepted for publication, and during the portion of that time that Alex was no longer in the group, I made significant contributions in the way of reviewer-requested revisions, including providing the data for additional figures.

1.7 Summary

VSFG spectroscopy overcomes the barriers to molecular-level study of adhesion and other phenomena at buried interfaces by providing access to the buried interface, the ability to distinguish molecules at a buried interface from those in the bulk, and the sensitivity to detect the small number of molecules participating in adhesion. The resonant signal in VSFG contains information about the identity and orientation of molecules in regions of broken symmetry within the probing depth of the input beams. Interference from the nonresonant signal hinders accurate spectral analysis, but recent advances in VSFG collection methods have made it possible to completely remove nonresonant signal to obtain the pure resonant peak parameters. We intend to study adhesion on a molecular level using VSFG during quantitative strength testing using recent findings about nonresonant signal to inform our study in order to correlate spectral data from the interface with the macroscopic behavior of an adhesive bond. Observing a correlation between spectroscopic data and strength-testing data is the first step in learning the relationship between adhesive molecular orientation and behavior.

Chapter 2 contains general information about the VSFG spectrometer setup and sample preparation. In Chapter 3, we discuss how nonresonant signal can exist in the absence of the indicators of nonresonant signal and how to exploit the polarizations of the nonresonant and resonant signals imposed by sample symmetry to check for nonresonant signal. Chapter 4 presents a paper on the changes in polystyrene thin films with plasma treatment. Due to the ability to successfully remove all nonresonant signal, this study reported different results than previous VSFG studies that assumed nonresonant signal to be negligible and provides evidence against the assumption that the effects of plasma treatment are limited to the free surface. To our knowledge, this study on the plasma treatment of polystyrene is the first VSFG study to challenge a previously accepted physical model. Chapter 5 details the current progress toward simultaneously obtaining VSFG spectra and quantitative adhesion strength measurements. Finally, Chapter 6 summarizes our work so far and describes current projects toward furthering our knowledge.

1.8 References

(1) Bain, C. D. *J. Chem. Soc., Faraday Trans.* **1995**, *91*, 1281.

(2) Zhu, X. D.; Suhr, H.; Shen, Y. R. *Phys. Rev. B* **1987**, *35*, 3047.

(3) Ding, B.; Laaser, J. E.; Liu, Y.; Wang, P.; Zanni, M. T.; Chen, Z. *J. Phys Chem. B* **2013**.

(4) Li, J.; Oh, K.; Yu, H. *Chin. J. Polym. Sci.* **2005**, *23*, 187.

(5) Wang, J.; Woodcock, S. E.; Buck, S. M.; Chen, C.; Chen, Z. *J. Am. Chem. Soc.* **2001**, *123*, 9470.

(6) Lu, X.; Li, D.; Kristalyn, C. B.; Han, J.; Shephard, N.; Rhodes, S.; Xue, G.; Chen, Z. *Macromolecules* **2009**, *42*, 9052.

(7) Wang, J.; Chen, C.; Buck, S. M.; Chen, Z. *J. Phys. Chem. B* **2001**, *105*, 12118.

(8) Zhang, C.; Hankett, J.; Chen, Z. *ACS Appl. Mater. Interfaces* **2012**, *4*, 3730.

(9) Lu, X.; Shephard, N.; Han, J.; Xue, G.; Chen, Z. *Macromolecules* **2008**, *41*, 8770.

(10) Vázquez, A. V.; Shephard, N. E.; Steinecker, C. L.; Ahn, D.; Spanninga, S.; Chen, Z. *J. Colloid Interface Sci.* **2009**, *331*, 408.

(11) Richter, L. J.; Petralli-Mallow, T. P.; Stephenson, J. C. *Opt. Lett.* **1998**, *23*, 1594.

(12) van der Ham, E. W. M.; Vrehen, Q. H. F.; Eliel, E. R. *Vib. Surf.* **1996**, *368*, 96.

(13) Laaser, J. E.; Xiong, W.; Zanni, M. T. *J. Phys. Chem. B* **2011**, *115*, 2536.

(14) Roeterdink, W. G.; Berg, O.; Bonn, M. *J. Chem. Phys.* **2004**, *121*, 10174.

(15) Roke, S.; Kleyn, A. W.; Bonn, M. *Chem. Phys. Lett.* **2003**, *370*, 227.

(16) Pool, R. E.; Versluis, J.; Backus, E. H. G.; Bonn, M. *J. Phys. Chem. B* **2011**, *115*, 15362.

(17) Stiopkin, I. V.; Jayathilake, H. D.; Bordenyuk, A. N.; Benderskii, A. V. *J. Am. Chem. Soc.* **2008**, *130*, 2271.

(18) Singh, P. C.; Nihonyanagi, S.; Yamaguchi, S.; Tahara, T. *J. Chem. Phys.* **2012**, *137*, 094706.

(19) Ji, N.; Ostroverkhov, V.; Chen, C.-Y.; Shen, Y.-R. *J. Am. Chem. Soc.* **2007**, *129*, 10056.

(20) Malyk, S.; Shalhout, F. Y.; O'Leary, L. E.; Lewis, N. S.; Benderskii, A. V. *J. Phys. Chem. C* **2012**, *117*, 935.

(21) Zhang, D.; Dougal, S. M.; Yeganeh, M. S. *Langmuir* **2000**, *16*, 4528.

(22) Gautam, K. S.; Schwab, A. D.; Dhinojwala, A.; Zhang, D.; Dougal, S. M.; Yeganeh, M. S. *Phys. Rev. Lett.* **2000**, *85*, 3854.

(23) Quast, A. D.; Curtis, A. D.; Horn, B. A.; Goates, S. R.; Patterson, J. E. *Anal. Chem.* **2012**, *84*, 1862.

(24) Himmelhaus, M.; Eisert, F.; Buck, M.; Grunze, M. *J. Phys. Chem. B* **1999**, *104*, 576.

(25) Bain, C. D.; Whitesides, G. M. *Science* **1988**, *240*, 62.

(26) Curtis, A. D.; Reynolds, S. B.; Calchera, A. R.; Patterson, J. E. *J. Phys. Chem. Lett.* **2010**, *1*, 2435.

(27) Curtis, A. D.; Burt, S. R.; Calchera, A. R.; Patterson, J. E. *J. Phys. Chem. C* **2011**, *115*, 11550.

(28) Briggman, K. A.; Stephenson, J. C.; Wallace, W. E.; Richter, L. J. *J. Phys. Chem. B* **2001**, *105*, 2785.

(29) Chen, Z.; Shen, Y. R.; Somorjai, G. A. *Annu. Rev. Phys. Chem.* **2002**, *53*, 437.

(30) Weeraman, C.; Chen, M.; Moffatt, D. J.; Lausten, R.; Stolow, A.; Johnston, L. J. *Langmuir* **2012**, *28*, 12999.

(31) Stiopkin, I. V.; Weeraman, C.; Pieniazek, P. A.; Shalhout, F. Y.; Skinner, J. L.; Benderskii, A. V. *Nature* **2011**, *474*, 192.

(32) Shalhout, F. Y.; Malyk, S.; Benderskii, A. V. *J. Phys. Chem. Lett.* **2012**, *3*, 3493.

(33) Meier, R. J. *Vib. Spectrosc.* **2005**, *39*, 266.

(34) Lagutchev, A.; Hambir, S. A.; Dlott, D. D. *J. Phys. Chem. C* **2007**, *111*, 13645.

(35) Stiopkin, I. V.; Jayathilake, H. D.; Weeraman, C.; Benderskii, A. V. *J.Chem. Phys.* **2010**, *132*, 234503.

(36) Curtis, A. D.; Asplund, M. C.; Patterson, J. E. *J. Phys. Chem. C* **2011**, *115*, 19303.

(37) Curtis, A. D.; Calchera, A. R.; Asplund, M. C.; Patterson, J. E. *Vib. Spectrosc*. **2013**, *68*, 71.

(38) Wilson, P. T.; Richter, L. J.; Wallace, W. E.; Briggman, K. A.; Stephenson, J. C. *Chem. Phys. Lett.* **2002**, *363*, 161.

(39) Wilson, P. T.; Briggman, K. A.; Wallace, W. E.; Stephenson, J. C.; Richter, L. J. *Appl. Phys. Lett.* **2002**, *80*, 3084

Chapter 2: Materials and Methods

2.1 Preparation of substrates for coatings

2.1.1 Cutting silicon wafers

Many of the experiments included in this dissertation were performed using silicon as a substrate for thin polymer films. The silicon substrates were cut from Si (111) test wafers doped with phosphorus (Cemat Silicon S.A.). The wafers were cut into approximately 1 inch by 1 inch squares using a tungsten carbide scriber and gloved hands. First, the wafer was placed face-down on a paper towel, then a straight line was scribed with the scriber about 1 inch from the edge of the wafer. The wafer was carefully broken at the scribe mark by pulling slightly while attempting to bend the wafer at the mark. The rectangular piece was further cut into 1 inch squares. The scoring was likewise made one mark at a time with the strip of silicon with the polished side down, and the break was performed by pulling and bending simultaneously. This procedure was repeated until the desired number of silicon pieces were obtained.

2.1.2 Removal of previous coatings

To prepare substrates for polymer coatings, any previous coating were first removed. If the substrate had not previously been coated, this step was skipped. To remove polymer coatings, the substrate was submerged in chloroform for several minutes. This solvent was chosen because the only coatings used in this study were polystyrene and poly (methyl methacrylate), both of which dissolve readily in chloroform. If multiple substrates were cleaned simultaneously, we ensured that the surfaces of the different substrate materials did not overlap so that all coated surfaces were completely exposed to the chloroform. Immediately following removal from the chloroform bath, all surfaces were completely rinsed with a stream of chloroform and air-dried by placing face-up on a paper towel. The substrates were rinsed a second time in a stream of fresh chloroform, and returned to dry on the paper towel. This process was repeated several times until no visible traces of coating remained on the substrate surfaces. CAUTION: All visible traces of organic solvent must evaporate from the surface prior to cleaning with piranha bath.

2.1.3 Piranha cleaning

CAUTION: Piranha bath is extremely corrosive and reactive. Acid piranha bath was made by combining 1 part 30% hydrogen peroxide solution with 3 parts 18 M sulfuric acid, by volume, in a glass crystallization dish. Fresh piranha bath was made every time samples were cleaned.

While the piranha bath is still hot, the clean, dry, substrates were added one by one to the piranha bath solution, ensuring that they were in a single layer with no overlap. The substrates were then left to react in the piranha bath for one to one and a half hours to remove any residual polymer, solvent, or contamination from storage. The clean substrates were removed one by one with clean, long forceps and rinsed with Millipore purified water (resistivity ≥ 18 MΩ·cm) immediately following removal from piranha bath. Each substrate was then submerged in additional purified water in a single layer so that the full surface to be coated is exposed to water. In the case of silicon substrates, the polished side was facing up, and in the case of sapphire or fused silica windows care was taken that the side that facing up was the side that was eventually coated. Clean substrates were stored completely covered by purified water for at least an hour until they were needed. If they were stored for more than twelve hours, the beaker containing the samples and water was covered with several layers of Parafilm® to minimize evaporation of the water and prevent contamination.

2.1.4 Final rinsing and drying

When the substrates were ready to be used, they were removed one by one from the water with clean long forceps, and rinsed with additional portions of Millipore water. Immediately following the rinsing, each substrate was carefully dried under a stream of nitrogen gas. The clean substrate was always coated or scanned as soon as possible following this final cleaning step.

2.1.5 Sample naming

After the cleaning procedure was completed and throughout all processing and testing thereafter, the samples were stored individually in Petri dishes labeled with a systematically-assigned sample name. The name consisted of letters indicating the substrate material and a number assigned chronologically to the sample. The numbers were assigned based on how many samples had been made previously using that substrate material, so although there were multiple samples with the number "1," there was only ever one sample called "SPS1." The substrate abbreviations used in the sample naming system are listed in Section A.2 of the Appendix.

2.2 Spin-coating thin polymer films

One of the first tasks in performing these studies was to determine reliable methods for creating thin polymer films of high quality and reproducible thickness. The thickness and quality of the film deposited by spin coating depends upon the concentration of polymer in the coating solution and the spin coating program used. This section describes two general methods that were used to create polymer thin films, illustrates the dependency of the final film thickness on both spin speed and polymer solution concentration. Following this section, we describe the methods used to make the films in these studies.

In general, the thickness of the film increases as the concentration of polymer in the polymer solution is increased or as the maximum spin speed is decreased. The recommended range for running the spin coater (Model WS650SZ-6NPP/A1/AR1 spin coater from Laurell Technologies) is between 1500 RPM and 4000 RPM, and all films were spin coated staying within this range of spin speeds. We have used both dynamic and static dispensing methods for spin coating in our group. With dynamic dispensing, the spin coating program is begun with no solution on the substrate, and the solution is dispensed by hand from a Pasteur pipet in an even stream during the first few seconds after the spin coater reaches the maximum spin speed. The dynamic dispensing method gives high-quality coatings with a single-step spin coating program but gives a large variation in coating quality and thickness between users.

Figure 2.1 was created from film thicknesses obtained using a dynamic dispense spin coating method to make polystyrene thin films from toluene solution. Figure 2.1 (a) shows the relationship between polymer concentration and the thickness of the resulting film for programs using different top spin speeds. Likewise, Figure 2.1 (b) shows the relationship between the top spin speed and the thickness of the resulting film for polymer solutions of varying thickness. The greatest variation is shown for solutions with the highest polymer concentration and programs with the highest top spin speed; however, the best quality of films were obtained using either 3% or 4% polystyrene solutions by weight, and a mid-range top spin speed.

Although we did not use a dynamic dispense method to create the thin polymer films in these studies, the general trends illustrated in Figure 2.1 also hold for the static dispense method as well as for other polymer solutions. In the static dispense method, the surface of the substrate

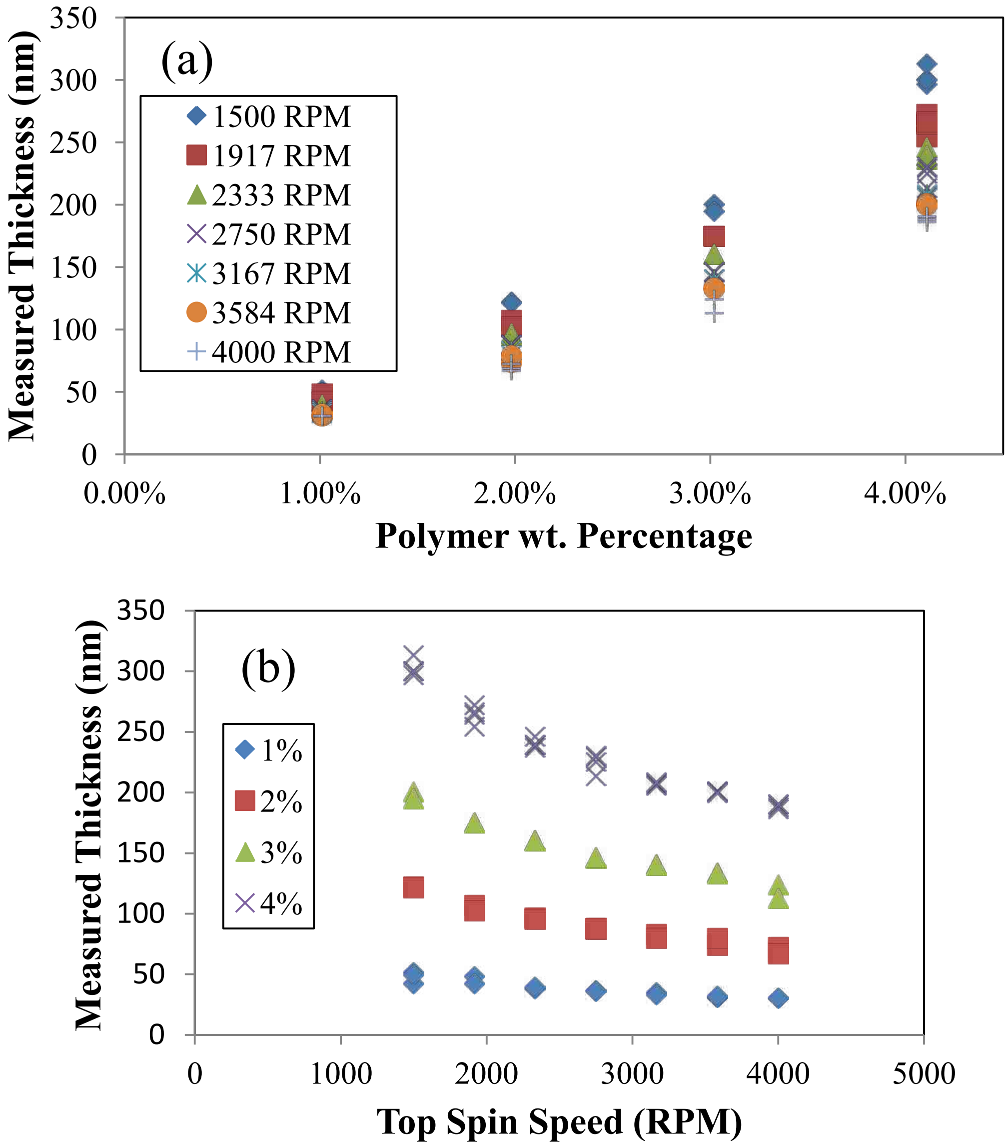

Figure 2.1. Variation of polystyrene thin film thickness as measured by spectroscopic ellipsometry as a function of (a) the concentration of polystyrene in the coating solution and (b) the top spin speed.

was totally covered with the polymer solution to be coated prior to beginning the spin-coating program. The static dispense method was used to spin coat all polymer films used in these studies because this method gives the most consistent results user-to-user and can still give good quality films. A sample list of programs and polymer solution concentrations used to spin coat high-quality thin polymer films of polystyrene and poly(methyl methacrylate) of varying thicknesses are included in Section A.1 of the Appendix.

2.2.1 Making polymer solutions

These studies used polystyrene (M_w=230,000 from Aldrich) spin coated from toluene (UltimAR® from Mallinckrodt Chemicals) solution and poly(methyl methacrylate) (M_w=120,000 from Aldrich) spin coated from nitromethane (spectrograde from Fisher Scientific) solution. The polystyrene came in pellet form, whereas the poly (methyl methacrylate) came in powder form. Slight differences in handling were necessary in the preparation of the polystyrene and poly(methyl methacrylate) as a result of these differences, and these differences are included in this section.

An Erlenmeyer flask was prepared for making the polymer solution by weighing the clean, dry flask and recording the mass. The flask was then rinsed with the solvent to be used for dissolving and diluting the polymer. A glass funnel with a Teflon® magnetic stir bar was used to direct the solvent into the flask, and with the stir bar in the funnel, the stir bar was rinsed at the same time as the flask. Following rinsing several times with clean solvent, the desired volume of solvent approximately equivalent to the final volume of solution desired was added to the flask. The mass of the flask and solvent were determined, and this value was used to determine the mass of the solvent added to the flask. The stir-bar was sometimes added to the flask at this time, and sometimes it was added after the addition of a properly measured mass of the polymer.

Using the mass of the solvent, the mass of polymer needed to achieve the desired concentration in solution was determined using

$$m_{polymer} = \frac{m_{solvent} x}{1 - x} \tag{2.1}$$

Where $m_{polymer}$ is the mass of the polymer needed, $m_{solvent}$ is the mass of the solvent determined by weighing by difference, and x is the desired mass fraction of polymer in the final solution.

Once the mass of the polymer needed was determined, the correct mass of polymer was weighed out. After zeroing the balance with a piece of folded weighing paper on the balance, the polymer was carefully added to the weighing paper until the correct mass had been measured. A piece of weighing paper was used as a funnel to transfer the polymer to the Erlenmeyer flask containing the solvent that had already been weighed. In the case of polystyrene, the same piece of weighing paper used to weigh the polymer could be used to transfer it to the flask because of the ease of transferring the pellets. Poly(methyl methacrylate) required the use of a separate piece of weighing paper inserted nearly to the solvent level in the flask to make the transfer. This extra care was required for poly(methyl methacrylate) because it came in powder form and easily adhered to the sides of the flask, and those pieces of polymer stuck to the side of the flask tended to not dissolve into the solution. After transferring the polymer to the flask, the stir-bar was added to the solution if it had not already been added in a previous step and left to stir overnight at room temperature on a stir plate.

2.2.2 Spin coating procedure

Just prior to coating, substrates are first prepared for by undergoing the full cleaning procedure as described in Section 2.1.

First, the nitrogen tank connected to the spin coater was opened and the regulator adjusted so that the output pressure was between 60 and 70 psi. The vacuum connected to the spin coater was also opened. The correct spin coating parameters were then programmed into the spin coater. The clean substrate to be coated was positioned so that the center of mass was centered on the chuck, and then the vacuum button was pressed to secure the sample to the chuck. Before applying any solution to the substrate, the substrate surface was carefully cleared of debris with canned air. The solution was applied with a Pasteur pipet so that the solution covered the entire surface of the substrate. The surface of the liquid was inspected to ensure that there were no air bubbles, and then the spin coater program is begun by pressing the green "start" button on the front of the spin coater control panel.

When the spin coating program completed, the coated substrate was removed from the chuck with forceps after the vacuum was released by pressing the vacuum button on the spin coater controller console, and the sample was stored in a Petri dish labeled with the sample name. The approximate thickness is given by the tables in Section A.1 of the Appendix, but the actual thickness of the coating was determined by spectroscopic ellipsometry, as further detailed in Section 2.3.

2.2.3 Creating layered samples

Layered samples can be created by spin-coating a film of poly(methyl methacrylate) on top of a film of polystyrene; however, polystyrene cannot be layered on top of poly(methyl methacrylate). Poly(methyl methacrylate dissolves well in nitromethane, toluene, and a variety of other solvents. We used nitromethane to make poly(methyl methacrylate) solutions for spin coating on top of polystyrene thin films because nitromethane dissolves poly(methyl methacrylate) but not polystyrene. Polystyrene cannot be coated on top of poly(methyl methacrylate) because every solvent that dissolves polystyrene also dissolves poly(methyl methacrylate). Coating poly(methyl methacrylate) on top of polystyrene using nitromethane as the solvent gives two well-defined layers, preserving the measured thickness of the bottom polystyrene layer; however, coating polystyrene on top of poly(methyl methacrylate) coats polystyrene while removing part of the bottom poly(methyl methacrylate) layer.

2.3 Determining film thickness using spectroscopic ellipsometry

Reported film thicknesses were determined just after coating by spectroscopic ellipsometry (M-2000 from J. A. Woollam Co., Inc.).. The substrate used for all thickness measurements was polished silicon; however, since the top layer of polished silicon is composed of silica, the thicknesses of films coated on fused silica from the same spin coating program and the same polymer solution were assumed to be the same as those coated on silicon. The collection angle on the ellipsometer was set to 45°, and the resulting data were fit using the built-in curve-fitting routines in the software included with the ellipsometer. In all models used to fit for polymer thickness, the thickness of silicon was set to 1 mm, and the thickness of SiO_2 used was the thickness measured prior to coating the substrate (~2 nm) by fitting the ellipsometry data to the SiO_2 model included in the ellipsometer software.

The models used to determine polymer thickness were developed by Alex Curtis using profilometry data from a collection of silicon substrates partially coated with three or four polymer thicknesses within the ranges used for these experiments. Prior to coating, approximately half of the piece of silicon was covered with a piece of cellophane tape. The tape was carefully removed, and upon visual inspection, there was a clean line separating the coated and uncoated portions of the silicon. Each partially coated sample was then measured by using a profilometer to measure the difference in height between the bare silicon and the coated silicon.

Profilometry revealed that the height at the edge of the coating was slightly greater than that of the majority of the coating. To compensate for this ridge, the height of the polymer coating was taken to be the height of the coated portion further from the ridge where the coating starts to flatten.

Ellipsometry models were created by first determining the thickness of the SiO_2 layer from the uncoated portion of the sample, and then collecting spectroscopic data from the coated portion of the sample. The data from the coated portion was fit to a model containing three layers: silicon, silicon dioxide, and a Cauchy layer. The thicknesses of Si and SiO_2 were entered into the model as 1 mm of Si and the thickness of SiO_2 measured previously. The thickness of the polymer that was determined by profilometry was entered as the thickness of the Cauchy layer, and data was fit by varying the optical constants, holding the film thickness constant. This method was repeated for all thicknesses of polymer, using the ending parameters of the previous fit as starting parameters for the next. After the determination of optical constants for the range of thicknesses desired, the layer was checked for accuracy by acquiring new data sets from the partially coated samples and fitting the data for thickness using the newly created custom layer and comparing the thickness determined using ellipsometry to the thickness determined using profilometry.

2.4 Plasma Treatment

Chapter 4 describes the study of the effects of plasma treatment on thin films of polystyrene as studied by VSFG. The plasma treatments for these studies were performed with an 18 W RF plasma from a Harrick Plasma basic plasma cleaner (PDC-32G). To perform the treatment, first the sample or samples were placed in the glass tube inside the plasma cleaner. The valve on the front cover of the plasma chamber was completely closed by turning the knob clockwise as far as possible. All of the stopcocks on the trap between the vacuum system and the plasma cleaner were closed except for the ones connecting the vacuum to the back of the plasma cleaner. The stopcocks remained in this position through the entire duration of plasma treatment.

The front cover was placed over the opening to the glass tube where the samples were placed, and the vacuum was turned on. The toggle switch on the front of the plasma cleaner on the lower right side labeled "power" was switched to the "on" position, and the power knob was turned to "high." The inlet nozzle on the front cover was adjusted until the plasma, visible through the vents on the left side of the unit, glowed bright violet. The nozzle was sometimes adjusted several times during the treatment to maintain the plasma intensity.

Upon completion of the desired treatment, the power knob was turned back counter-clockwise to the "off" position, and the power toggle switch was also turned to "off." The partial vacuum was released by slowly opening the air inlet valve on the front cover of the plasma cleaner while supporting the cover with a free hand. As the pressure inside the chamber equilibrated with the ambient room pressure, the cover eventually released on its own from the front opening of the plasma chamber, and the samples were removed and stored in clearly labeled Petri dishes.

2.5 Annealing

To anneal a polymer coating, the samples were stored in a vacuum oven at a constant temperature for 24 hours, and then slowly cooled down to room temperature. The temperature selected for annealing was above the glass transition temperature but below the melting point of the polymer. For example, the polystyrene in these studies was annealed at 120°C.

To preheat the oven, the closed oven was turned on several hours prior to the annealing process, adjusting the heating dial several times during that period until the thermometer inserted inside the oven read the desired temperature when the light indicating active heating turned off. The vacuum oven is equipped with a liquid nitrogen-cooled trap between the vacuum inlet and the lab vacuum. Just before storing samples in the oven, the u-shaped trap was submerged in a Dewar flask filled with liquid nitrogen. After the samples were arranged in the oven, the door was closed, the latch secured, and the air was removed by turning on the vacuum with the valve connected to the vacuum open and the valve open to the air closed. Once the pressure inside the oven reached a minimum, the vacuum valve was sealed and the vacuum turned off. The trap remained connected to the vacuum but was no longer necessary, and the liquid nitrogen was allowed to evaporate from the Dewar flask during the annealing period.

After 24 hours, the oven was turned off, but the door remained closed for another 24 hours to allow the samples to slowly cool to room temperature. After the samples cooled, the partial vacuum was released by opening the inlet valve to fill the oven with room air, the latch and oven door were opened, and the samples were removed and stored in clearly labeled polystyrene Petri dishes.

2.6 Vibrational sum-frequency generation spectroscopy

2.6.1 Spectrometer description

The sum-frequency generation spectrometer used in these studies was originally set up by L. Robert Baker and Alexander D. Curtis. A schematic of this spectrometer and more recent alterations made to allow for the selection of different signal polarizations is shown in Figure 2.2. The amplified Ti-Sapphire laser (Quantronix, Integra-C) puts out 120 fs pulses at

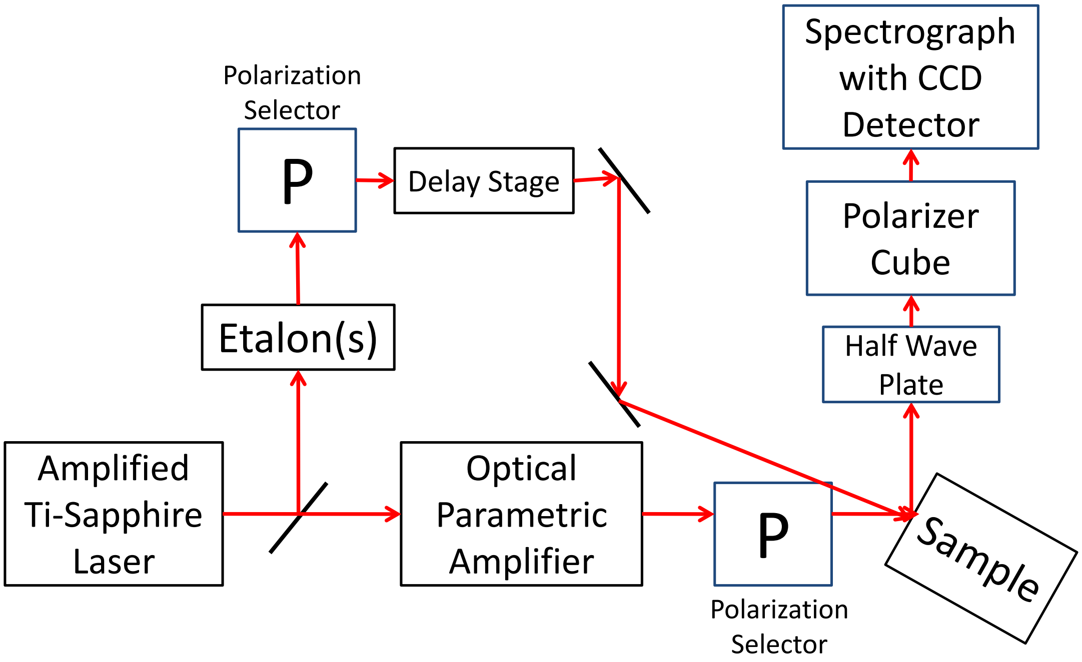

Figure 2.2 Schematic diagram of sum-frequency generation spectrometer

1 kHz centered around 795 nm, with about 2.7 mJ per pulse. This power then goes to a beam splitter, where most of the intensity goes to the optical parametric amplifier (Light Conversion via Quantronix, TOPAS-C). The optical parametric amplifier (OPA) converts the visible output of the laser to tunable mid-infrared light that was tuned to 3200 nm with power of about 20 mW for these studies. Prior to hitting the sample, the light must pass through a periscope that allows us to select the polarization of the infrared beam. The infrared pulse then hits the sample and excites vibrations at the resonant frequencies of the molecule.

The portion of light that is reflected at the beam splitter goes through either one or two Fabry-Perot etalons. The purpose of the etalons is two-fold: they narrow the frequency distribution of the beam, giving the collected spectra better frequency resolution, and they make the visible pulse longer in time. They also provide an ideal pulse shape for the suppression of non-resonant signal. Nonresonant signal suppression by delaying the visible pulse with respect to the infrared pulse requires that the visible upconverting pulse have a sharp rise and gradual fall similar to what is provided by the two etalons.

The polarization selector for the visible beam is a periscope followed by a half-wave plate. The polarization of the visible beam is adjusted by adjusting the half-wave plate and checking with a polarizer cube.

The visible pulse then goes to a mechanical delay stage controllable by remote computer. Sum-frequency signal is generated at the sample only when the infrared and visible pulses overlap spatially in the correct sequence and within a few picoseconds of each other. The temporal delay between the infrared and visible pulses can also be used to suppress nonresonant signal.[1] The delay stage was adjusted to ensure the correct timing of the two pulses but was also aligned such that the beams are spatially unaffected by the temporal adjustments.

All frequencies of the generated light are detected simultaneously using an Andor charge-coupled device (CCD). Prior to collection at the detector, the signal passes through a half-wave plate used to rotate the polarization. The detector is more sensitive to *p*-polarized light than to *s*-polarized light, so typically the wave plate was rotated so that the majority of signal is *p*-polarized after passing through it. Following the wave plate, the VSFG signal passes through a polarizer cube that allows *p*-polarized light to pass through and reflects *s*-polarized light. The polarizer cube is on a delay stage that allowed us to easily and cleanly move it in and out of the beam path. The polarization experiments reported in Chapter 3 involved changing the polarization of light that passed through to the detector by rotating the wave plate and altering the position of the polarizer cube. Section 2.6.4 details the procedure for making these changes.

2.6.2 Initial alignment of the VSFG system

Spatial overlap of the input beams at the sample was achieved in steps. First, a piece of card paper coated in graphite was used to roughly overlap the two beams. The focused infrared beam causes the graphite to spark, and the visible beam can be overlapped with the spark. Following alignment with graphite, a window of CLEARTRAN™ (Advanced Materials) was placed in the sample mount, and the delay stage was adjusted so that the VSFG signal was at a maximum. CLEARTRAN™ produces a nonresonant VSFG signal throughout the region that the two input beams overlap. When the input beams are properly overlapped, the signal produced from CLEARTRAN™ is visible to the naked eye. The output path was also adjusted using the visible output signal from CLEARTRAN™ with the assistance of the detector collecting data in real time.

Following alignment with CLEARTRAN™, a gold mirror was placed in the sample mount, and the alignment was repeated. However, the signal produced off of a gold mirror is not visible without the detector. Alignment of the beams with the gold mirror was achieved using the detector collecting data in real time, both to make final fine adjustments to the spatial and temporal overlap of the input beams and to adjust the path of the output beam to the detector. With proper spatial and temporal alignment of the visible and infrared beams, sum-frequency signal is generated at the sample.

2.6.3 Daily alignment of the VSFG system

Under normal operating conditions (after initial alignments), all three beams should already be roughly aligned, but fine adjustments were made every day to maximize the signal collected during experiments. These alignments were also necessary when the wavelength of the infrared pulse from the OPA was changed. The laser was turned on and allowed to warm up for about two hours, and then power measurements were recorded. After powering up the laser, the gold mirror was placed in the sample mount, and the temporal and spatial overlap of the input beams and to the collection path of the VSFG beam were slightly adjusted to maximize signal and minimize output signal aberration. The gold mirror was then plasma cleaned at high power for five minutes according to the procedure described in Section 2.4. The gold mirror was plasma cleaned whenever the signal profile from the gold mirror showed resonant attenuation from contaminants. After cleaning the gold mirror, a spectrum of the full nonresonant response off of gold was collected as a reference at least once every day using the same collection parameters as the experimental spectra.

2.6.4 Polarization Experiments

The experiments in Chapter 3 were performed by changing the polarization of the signal collected. All of these experiments were performed with *s*-polarized visible input and *p*-polarized infrared input. To collect the *s*-polarized portion of the output signal, the wave plate was rotated to maximize signal off the gold mirror with the polarizer cube in place prior to collecting experimental data. To collect the *p*-polarized portion of the output signal, the wave plate was rotated to minimize signal off of the gold mirror with the polarizer cube in place. "Unfiltered" spectra were collected with the polarizer cube stage pushed back out of the beam path, and "filtered" spectra were collected with the polarizer cube directly in the beam path. It should be noted that despite the designation of "filtered" and "unfiltered" to the spectra in the polarization experiments of Chapter 3, in reality all of the spectra were filtered to some degree because the detector is more sensitive to vertically (*p*-) polarized light than to horizontally (*s*-) polarized light. However, from the observed differences between the "filtered" and "unfiltered" spectra, it is apparent that polarization selection by the detector alone is incomplete.

2.7 References

(1) Lagutchev, A.; Hambir, S. A.; Dlott, D. D. *J. Phys. Chem. C* **2007**, *111*, 13645.

Chapter 3: Ensuring adequate suppression of nonresonant signal in vibrational sum-frequency generation spectroscopy

3.1 Introduction

Vibrational sum-frequency generation (VSFG)[1,2] has become a powerful tool for investigating the molecular structure of free surfaces and buried interfaces.[3-7] In this nonlinear optical technique, two laser pulses, one visible and one infrared, interact with a surface or interface, producing a nonlinear polarization that oscillates at the sum of the two input frequencies. Under the dipole approximation, the nonlinear susceptibility, $\chi^{(2)}$, is identically zero for an isotropic medium; thus, no SFG signal is produced from amorphous bulk material. At a surface or interface, however, this symmetry is broken and some elements of the $\chi^{(2)}$ tensor are nonzero, which provides VSFG with inherent selectivity for surfaces and interfaces. Unfortunately, the VSFG measurement generally includes a nonresonant response that can interfere with and distort the features that correspond to vibrational resonances. For broadband VSFG systems,[8,9] methods have been developed to experimentally suppress the nonresonant signal by introducing a time-delay between the incident infrared and visible probe pulses.[10] As we show here, however, great care must be taken to ensure that all the nonresonant signal has been fully suppressed. Otherwise, unaccounted for distortions remain in the measured spectrum, which will negatively affect any analysis and interpretation of those results.

The nonlinear susceptibility that governs the VSFG process is typically written as

$$\chi^{(2)} = \chi^{(2)}_{NR} + \chi^{(2)}_{R}(\omega) = \chi^{(2)}_{NR} + \sum_{R} \frac{A_R}{\omega - \omega_R + i\Gamma_R} \tag{3.1}$$

where the overall susceptibility consists of a nonresonant (NR) term, considered to be frequency independent, and a resonant (R) term, which depends on the infrared frequency. The resonant term consists of individual elements for each discrete vibrational resonance, each represented by a Lorentzian profile with amplitude A_R, central frequency ω_R, and line width Γ_R. Both the resonant and nonresonant terms are mathematically complex, which can lead to interference between the various contributions. The measured VSFG signal can be mathematically represented as follows:

$$I_{SFG} \propto \left|\chi^{(2)}\right|^2 = \left|\chi_{NR}^{(2)}\right|^2 + \left|\chi_R^{(2)}(\omega)\right|^2 + \left|\chi_{NR}^{(2)}\right|\left|\chi_R^{(2)}(\omega)\right|\cos[\delta(\omega)] \tag{3.2}$$

where $\delta(\omega)$ is a frequency-dependent phase term. The cross term in this expression accounts for the interference between the resonant and nonresonant contributions and often results in dispersive line shapes of the resonant features. If two or more resonances are near enough, they can also interfere with each other.

Because of the interference and distortion it causes, the nonresonant contribution is an important part of a VSFG measurement; it should not be thought of as simply a background to the resonant response. Although the source of the nonresonant signal is still an area of investigation, it is generally accepted that this contribution arises from fast electronic responses in the sample.[11,12] As such, it can depend on multiple factors at the surface or interface, such as material identity,[3] interface potential,[13-16] and solvent identity at a solid-liquid interface.[17] It can also arise from all components of the sample,[18,19] and may even have contributions from the bulk through electric-quadrupole and/or magnetic-dipole effects.[20-26] In fact, as recently stated by Y. R. Shen, "the electric-quadrupole and magnetic-dipole contributions of the bulk to SFG are always allowed and cannot generally be ignored, but this point has not been emphasized enough in the literature."[27] The purpose of this work is not to account for all the sources of the nonresonant contribution, be they surface or bulk, but to properly ensure that the nonresonant contribution can be completely removed from the measured VSFG spectrum.

VSFG can be performed in one of three experimental configurations. The first, which could be termed narrowband VSFG, uses spectrally narrow visible and infrared pulses. The infrared frequency is then scanned over the range of interest to produce the VSFG spectrum. The second approach is often termed broadband VSFG and involves the use of a narrowband visible pulse and a broadband (temporally short) infrared pulse to cover a broad spectral range without the need for scanning.[8,9] The third approach involves using short pulses for both the visible and infrared beams. In this time-domain VSFG approach,[11,28] the time-domain response is what is measured and the frequency-domain spectrum is produced through a Fourier transform.

In each of these techniques, different approaches have been put forth to isolate the nonresonant response from the resonant response. With broadband VSFG, the introduction of a time delay between the infrared and visible pulses allows for experimental suppression of the nonresonant signal because it decays more quickly than the resonant free induction decay (FID).[10] The measured resonant response is affected by this time delay,[29] but this can be corrected through additional measurements at multiple delay times.[30] In the time-domain VSFG approach, with heterodyne detection, the real and imaginary components of the signal are both measured. It is argued that[28] because the nonresonant response is "instantaneous", it should only be included in the real portion and that the imaginary response is completely resonant. In this fashion, the resonant and nonresonant components can be separated. In narrowband VSFG, not much can be done to remove the nonresonant response without phase-sensitive detection. In this case, as in the time-domain approach, the nonresonant contribution is assumed to exist only in the real portion of the signal, leaving a purely resonant imaginary portion.[31]

Our work focuses on suppression of the nonresonant response in broadband VSFG. This is the only case where the isolation of the nonresonant response occurs directly as part of the measurement and not in a post-processing step. In either the time-domain approach or a phase-sensitive narrowband measurement, a common assumption is that the imaginary portion of the signal contains no nonresonant contribution. Although this may be a reasonable assumption for monolayers on metallic substrates, we have serious reservations about applying this assumption to the case of polymer thin films, where we have seen significant contributions to the nonresonant response from the bulk polymer.[18,19] Even if the nonresonant signal arises “instantaneously”, the finite thickness of a polymer layer means that the nonresonant signal is generated over a range of time, and there will be a phase lag between different portions of the nonresonant signal because the resonant and nonresonant signal contributions arise from different physical locations. Thus the focus of this chapter centers on ensuring that all the nonresonant signal is experimentally suppressed in a broadband VSFG measurement, thereby minimizing the number of assumptions that must be made in subsequent analysis and interpretation. We use a combination of experimental measurement and theoretical modeling to pursue this end.

Before proceeding further in a discussion of how to ensure complete removal of the nonresonant signal, we wish to point out that the nonresonant response is not without value. For example, we have found that the intensity of the nonresonant contribution for polystyrene thin films changes with the history of the sample.[18] We have also observed changes in the nonresonant contribution for functionalized fused silica surfaces with a change in solvent environment.[17] Interference with the nonresonant signal has also been used to determine the absolute orientation of molecules relative to the surface.[32,33] There are likely other uses for the nonresonant SFG signal, but proper interpretation of the resonant response requires that the nonresonant contribution be completely removed.

3.1.1 Theoretical Treatment and Modeling Approach

The conventional frequency-domain description of the VSFG signal is provided by Equations (3.1) and (3.2). For this discussion, however, we must also consider a time-domain description of this process. In the sum-frequency generation process, two laser pulses interact with the system of interest. First, the broad-band, ultrafast IR pulse interacts with the sample in two ways: it excites resonant vibrations, including vibrations in the bulk as well as the surface;[34] it excites a nonresonant electronic response within the sample. The nonresonant electronic response decays very quickly, and does not persist once the IR excitation field has ended. The resonant vibrational response will dephase over a period of several picoseconds. The second interaction is with the narrow-band visible pulse, which upconverts the first-order polarization to a second-order polarization and imparts surface selectivity for isotropic materials. The time-integrated second-order polarization is measured in the frequency domain, and the measured signal is affected by the temporal delay between the two laser pulses.[29]

The second-order nonlinear polarization arises from the interaction of the sample with the two incident laser pulses. This can be written mathematically as

$$P^{(2)}(t) = \int_{-\infty}^{\infty} dt_1 \int_{-\infty}^{\infty} dt_2 \, S^{(2)}(t_1,t_2) E_{vis}(t-t_2) E_{IR}(t-t_2-t_1) \ . \tag{3.3}$$

In this expression, [35] $S^{(2)}(t_1,t_2)$ is the time-dependent, second-order response function of the sample, t_1 refers to the time between the IR and visible pulses, and t_2 refers to the time between the visible pulse and an arbitrary later time, t. The two incident fields, E_{vis} and E_{IR}, are the local fields at the surface or interface. In the "two-step" picture of the VSFG process,[29] the IR pulse excites a first-order polarization in the sample

$$P^{(1)}(t) = \int_{-\infty}^{\infty} S^{(1)}(t_1) E_{IR}(t - t_1) dt_1 = S^{(1)}(t) \otimes E_{IR}(t) \tag{3.4}$$

where $\otimes$ denotes convolution. $P^{(1)}(t)$ is asymmetric in time, rising with the leading edge of the temporal profile of the IR pulse and decaying according to the dephasing of the resonant molecular vibrations. The early-time portion of $P^{(1)}(t)$ will also contain the nonresonant response of the sample.

The first-order polarization is converted to a second-order polarization by the second, visible pulse. The interaction between the visible pulse and the first-order polarization can be thought of as occurring instantaneously at each time-point of the interaction; i.e., no phase lag is introduced by this interaction at each point in time. Mathematically, each point in time of the interaction can be written as $S^{(2)}(t_1, t_2) = S(t_1)\delta(t_2)$, meaning the integration over t_2 is simply replaced by multiplication of the time-dependent visible field. The visible field therefore acts as a window function which upconverts the first-order polarization. It is important, however, to maintain the possibility of a time delay between the two pulses, which we will symbolize as τ. The final description of $P^{(2)}(t, \tau)$ can then be written as

$$P^{(2)}(t, \tau) = P^{(1)}(t) E_{vis}(t - \tau) = \left[S^{(1)}(t) \otimes E_{IR}(t) \right] E_{vis}(t - \tau) . \tag{3.5}$$

The measured VSFG spectrum is then proportional to the square of the Fourier transform of this polarization

$$I_{VSFG}(\omega, \tau) \propto \left| \int_{-\infty}^{\infty} P^{(2)}(t, \tau) e^{i\omega t} dt \right|^2 . \tag{3.6}$$

Note that the measured VSFG spectrum depends on the delay time between the two pulses.

The measured VSFG response also depends on the temporal shape of the visible pulse.[29] Spectral narrowing of the visible beam by a dispersive element and slit will produce a time-symmetric pulse. Delay of such a pulse relative to the infrared pulse will significantly affect the line shapes of the resonant features. The other common method for spectral narrowing of the visible beam is with an etalon. This causes the pulse to be time-asymmetric, with a steep rising edge and a longer decay.[10] This type of pulse lends itself well to suppressing the nonresonant response, because the fast, nonresonant signal can decay before the visible pulse arrives, but the visible pulse has a sufficient enough tail to overlap with the majority of the resonant free induction decay. This pulse shape also results in changes to the measured resonant signal, because the front end of the resonant FID is apodized in the time-domain,[28,36] but these effects can be corrected through multiple measurements at additional delay times.[30]

The variable time delay method[30] actually takes advantage of the changes that occur to the measured VSFG spectrum because of apodization in the time-domain. Multiple spectra are acquired at different delay times and, because the underlying FID is always the same, the multiple spectra can be simultaneously fit to a single set of spectral parameters. The mathematical basis of this method of analysis begins with a description of the VSFG spectrum as the frequency-domain convolution of the resonant spectral features and the visible probe beam

$$I_{VSFG} = \left| L(\omega) \otimes V(\omega) \right|^2 . \tag{3.7}$$

The term $L(\omega)$ represents the sum of Lorentzian features from Equation (3.1) and $V(\omega)$ represents the spectrally narrow visible pulse. We have found that this method only works when the nonresonant signal has been fully suppressed, therefore the nonresonant term from Equation (3.1) need not be included here.

Because of the variable time delays performing this type of measurement, it is more useful to recast Equation (3.7) in the following form

$$I_{VSFG}(\omega,\tau) = \left| ft\left[ift\left(L(\omega)\right) \times ift\left(V(\omega)\right)\right]\right|^2 = \left| ft\left[ift\left(L(\omega)\right) \times V(t-\tau)\right]\right|^2 \qquad (3.8)$$

Here, *ft* and *ift* represent the Fourier transform and inverse Fourier transform, respectively, and $V(t-\tau)$ represents the temporal profile of the visible pulse with delay time τ. The shape of $V(t)$ is determined by cross-correlation with the much shorter infrared pulse. Changing the delay time only shifts the profile of $V(t)$ in time, but does not change its shape; however changing the delay time does cause changes in the measured I_{VSFG}. $L(\omega)$ is unchanged with the delay time because the resonant FID is the same, being caused by the same incident infrared pulse. Simultaneous fitting of multiple spectra, acquired at multiple delay times, allows for extraction of the resonant spectral parameters, which are then free of any distortion resulting from interference with the nonresonant signal and from apodization effects caused by suppression of the nonresonant signal. This process is shown graphically in Figure 3.1. This same mathematical approach is used to generate the model spectra presented in this chapter; model spectra are generated from a given set of resonant parameters, a given temporal profile and the visible beam, and a chosen delay time.

As stated above, in our experience, the variable time delay approach is only successful with spectra where all the nonresonant response has been experimentally suppressed. Inclusion of even a small amount of nonresonant signal results in an unsuccessful analysis. The largest problem with including the nonresonant signal is the lack of an adequate model for this

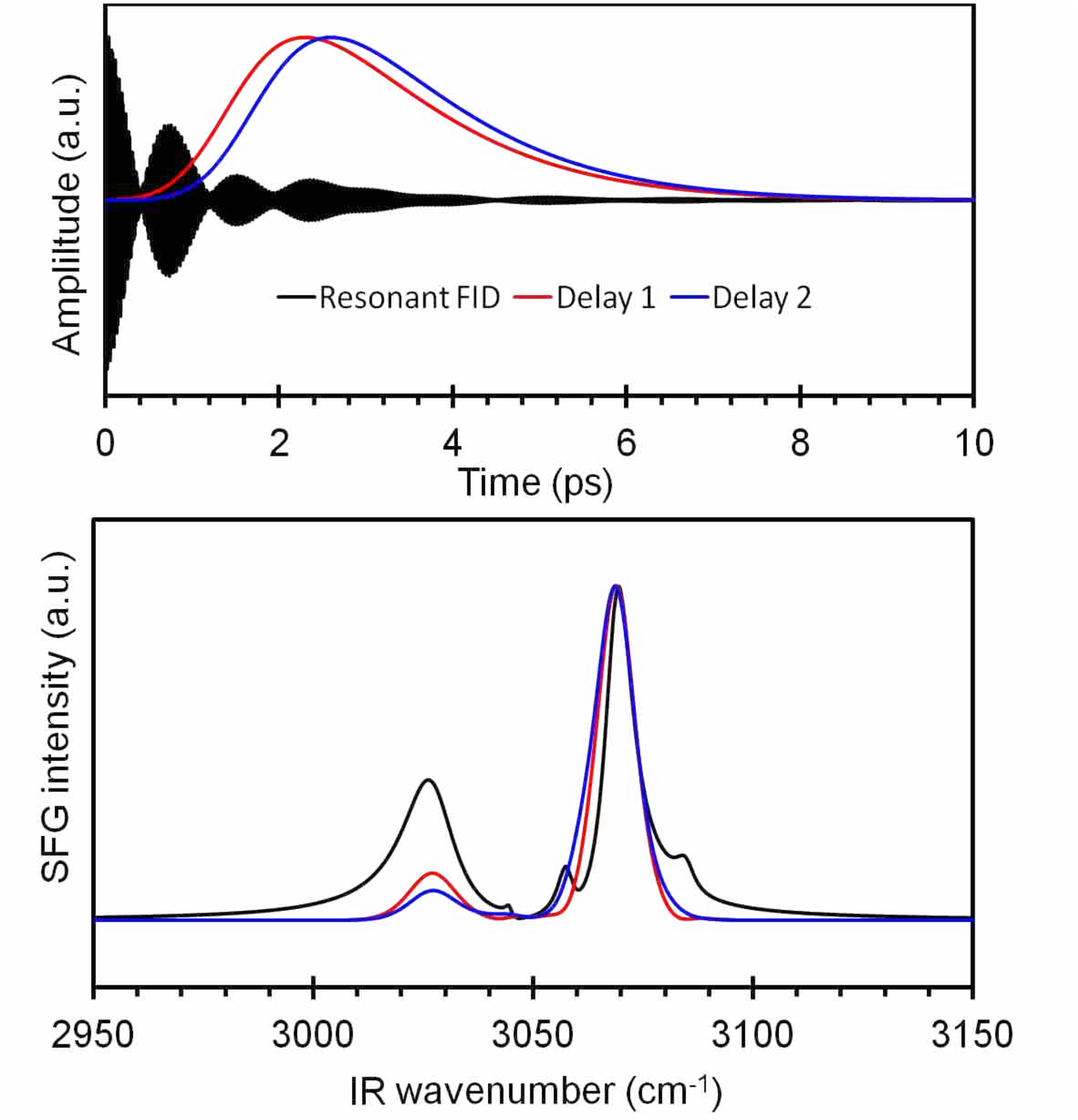

Figure 3.1. Pure resonant peaks without apodization and with apodization by the time profile of the upconverting pulse at (red) 2.3 ps and (blue) 2.6 ps.

signal.[19,37] The inclusion of additional, unknown parameters will only complicate the determination of an unique set of fitting parameters.[38] Ensuring adequate suppression of nonresonant signal is particularly important when spectra are compared from a single visible pulse delay. As we demonstrate in this chapter, good fits can still be obtained when nonresonant signal is present, but fit parameters vary from those that would be obtained if the signal were free from nonresonant interference. It is therefore vitally important that all nonresonant signal be completely removed from the measured VSFG spectrum. As we show in this chapter, it is not always obvious when the nonresonant signal is adequately suppressed.

3.2 Methods

3.2.1 Building Theoretical Models

Theoretical models were made using MATLAB. The purely resonant spectrum of polystyrene was modeled using a sum of Lorentzian peaks, each described by

$$L(\omega) = \frac{\sqrt{A}\Gamma}{\omega - \omega_0 + i\Gamma} \tag{3.9}$$

where A is the amplitude, Γ is the half width at half max, and ω_0 is the center frequency. The parameters of the peaks were those previously determined using the variable time delay technique.[39]

The nonresonant signal was modeled using a Gaussian profile with an added complex exponential term to account for the phase, described by

$$NR = \frac{A}{\sqrt{2\pi\sigma^2}} e^{\frac{-(\omega-\omega_0)^2}{2\sigma^2}} e^{i\Phi} \tag{3.10}$$

where A is the amplitude, σ^2 is the variance, ω_0 is the center frequency, and Φ is the innate phase of a Lorentzian peak, given by

$$\Phi = \tan^{-1}\left(\frac{\Gamma}{\omega - \omega_0}\right) \tag{3.11}$$

where Γ is the half width at half max for the Gaussian, and ω_0 is the central frequency . This phase term was added to allow the Gaussian peak to interfere with other peaks in the model as they would in a coherent technique like VSFG.[40]

To create the attenuated nonresonant profile shown in Figure 3.2 (b), the modulus squared of the sum of the five resonant Lorentzian peaks of polystyrene was subtracted from the modulus squared of the Gaussian nonresonant profile. We took the modulus squared of the unattenuated nonresonant response when creating Figure 3.3 because the modulus squared of the nonresonant response was taken to model the attenuated nonresonant response used to create in Figure 3.4 (a). The spectra in Figure 3.3 and Figure 3.4 (a) were generated by transforming the appropriate nonresonant profile and the resonant peaks to the time domain and adding them together in the time domain with equal amounts of nonresonant and resonant signal. The resulting spectra were created by transforming the resulting signal back to the frequency domain and plotting the modulus squared.

All other spectra modeled in this study were modeled using the unattenuated Gaussian nonresonant response. Although attenuation of the nonresonant signal due to competition with resonant features can be well-described in the frequency domain by

$$Att(\omega) = \left|NR\right|^2 - \left|\sum L(\omega)\right|^2 \tag{3.12}$$

the transform of Equation (3.12) with its modulus-squared terms probably does not satisfactorily describe the behavior of the actual attenuated nonresonant response in the time domain. The

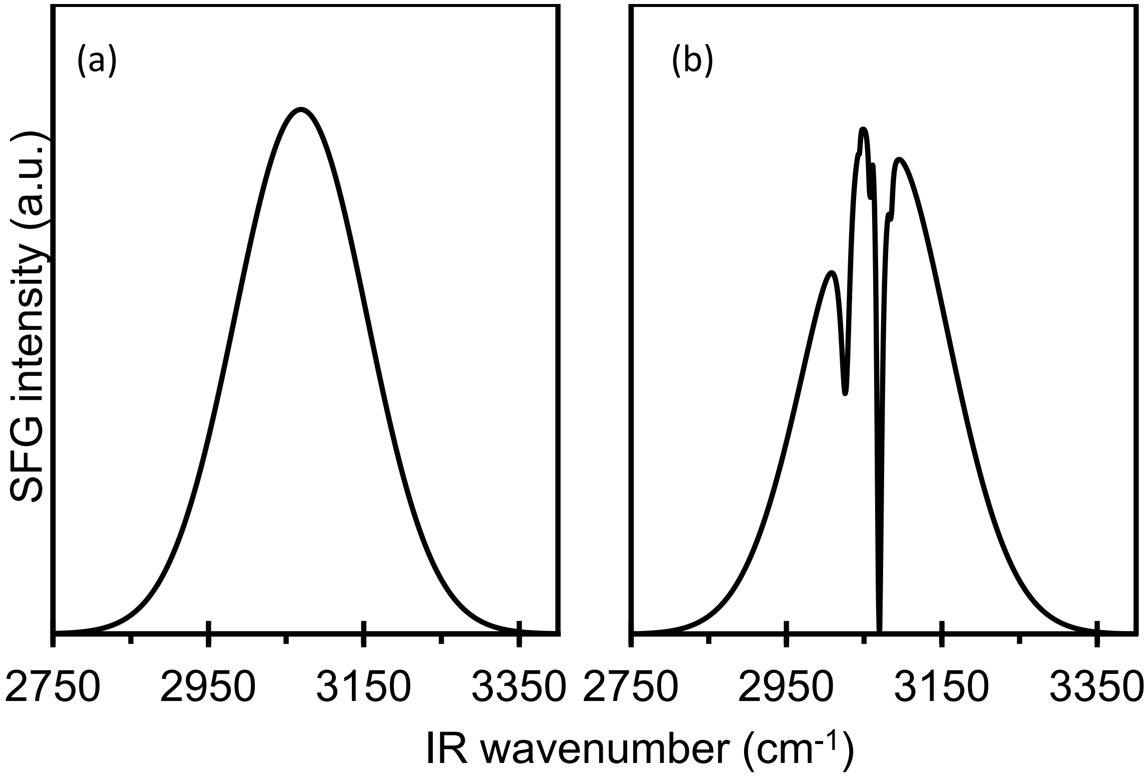

Figure 3.2. Model spectra of (a) purely nonresonant signal and (b) nonresonant signal attenuated by resonant absorption of polystyrene.

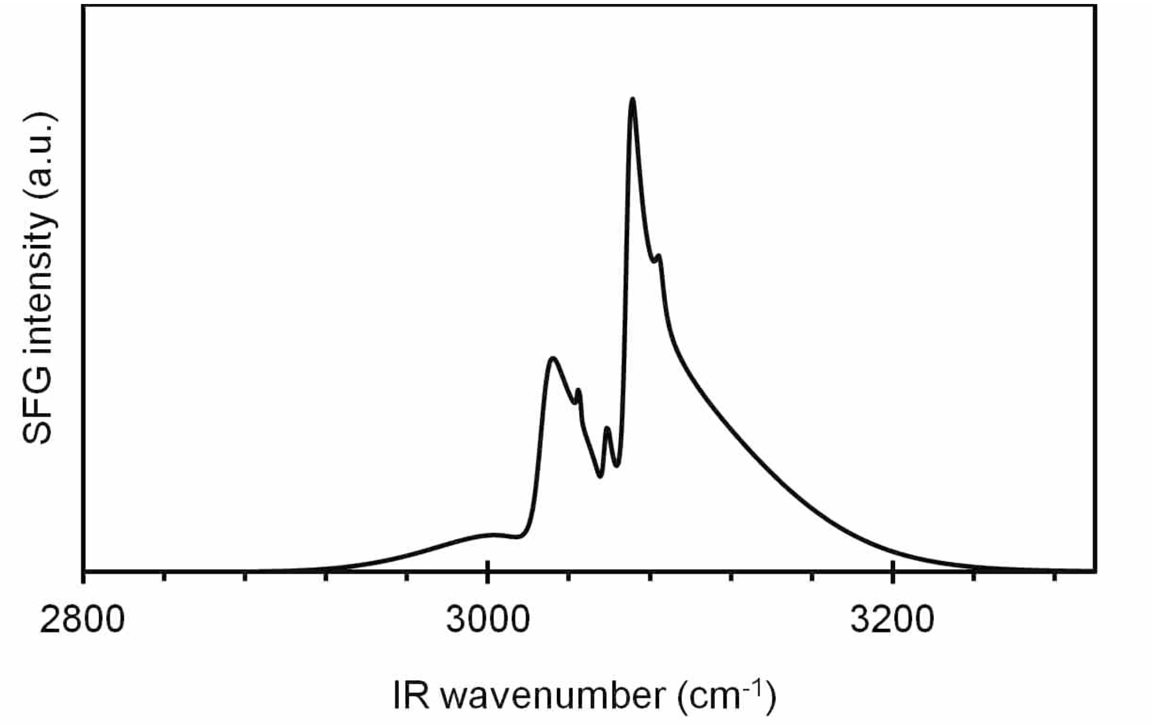

Figure 3.3. Modeled data generated by allowing the unattenuated gaussian nonresonant response to interfere with the resonant spectrum**.**

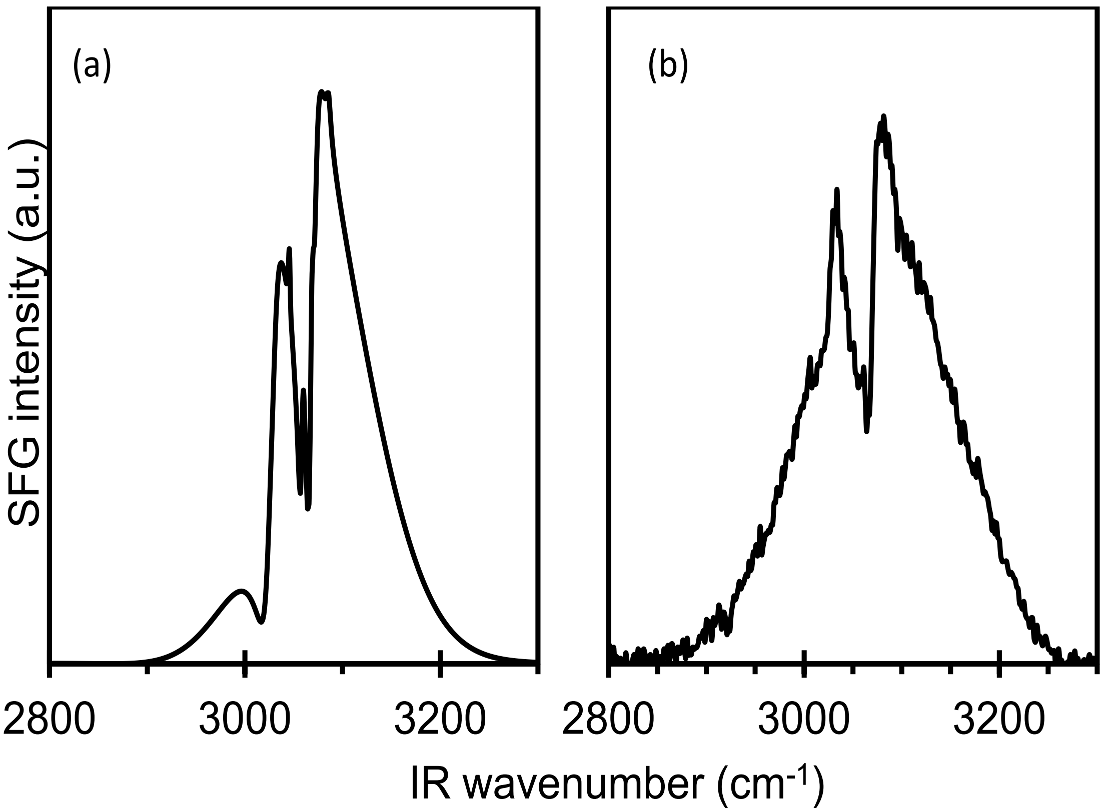

Figure 3.4. Two spectra in which the attenuated nonresonant response is allowed to interfere with the resonant response. Spectrum (a) is a model spectrum made by combining a purely resonant polystyrene spectrum with the nonresonant signal attenuated by the same resonant polystyrene spectrum. Spectrum (b) is an experimental spectrum of a 220 nm polystyrene film on polished silicon without nonresonant suppression. Both spectra exhibit the broad peak base and derivative line shapes typical of signals with nonresonant interference present.

unattenuated model nonresonant signal is simpler to use, and it is still complex; therefore, it is able to interfere with the resonant features in the time domain similar to the way a nonresonant response would during a VSFG experiment. Other than Figure 3.2, Figure 3.3, and Figure 3.4 where equal amounts of resonant and nonresonant signal were used, all model spectra were made such that the maximum of the resonant signal was equal to five times the maximum of the nonresonant signal.

The apodization of spectra was done by convoluting the signal in the time domain with a model time profile of the visible up-converting pulse. This pulse was modeled using a Gaussian peak with a single exponential decay. The MATLAB code used to generate the spectra, including apodizations, is included in section A.3 of the Appendix.

Spectral fitting parameters were obtained using the curve fitting tool (cftool) in MATLAB by fitting to the model equation

$$\mathrm{f}(\omega) = \left| \frac{\sqrt{A_1}\Gamma_1}{\omega - \omega_1 + i\Gamma_1} + \frac{\sqrt{A_2}\Gamma_2}{\omega - \omega_2 + i\Gamma_2} \right|^2 \tag{3.13}$$

Equation (3.13) accounts for only for two Lorentzian peaks and assumes no contribution from the nonresonant signal.

3.2.2 Experimental

Polished silicon (111) wafers were cut into approximately 1-inch squares and cleaned by immersion in piranha solution (18 M sulfuric acid and 30% hydrogen peroxide, 3:1 by volume) for one hour. (*Cautionary Note*: Piranha solution is very corrosive, and extreme care must be used when handling.) The clean silicon was then rinsed with Millipore-purified water (18 MΩ), then immersed in Millipore-purified water for at least one hour. Just prior to coating, silicon pieces were dried under a stream of nitrogen gas. Polystyrene (M_w=230,000 from Aldrich) solution in toluene (UltimAR® from Mallinckrodt Chemicals) was then coated on the clean silicon substrate with a spin-coater (Model WS650SZ-6NPP/A1/AR1 from Laurell Technologies) to give ~100 nm thick films. Film thicknesses were determined using spectroscopic ellipsometry (M-2000 from J. A. Woollam Co., Inc.) .

VSFG spectroscopy was performed using an altered version of the set-up described in detail elsewhere.[41] An amplified femtosecond laser (Quantronix, Integra C) is split into two beams. One beam is used to generate a spectrally broad infrared pulse by pumping an optical parametric amplifier (Light Conversion via Quantronix TOPAS-C). The second beam, used as the visible upconverting pulse, is spectrally narrowed using either one or two Fabry-Perot etalons. The experimental data obtained with full nonresonant suppression was performed using two etalons to narrow the visible pulse, whereas all other data was collected using a single etalon. In all cases, the infrared input was *p*-polarized, and the visible input was *s*-polarized.

A half-wave plate and a polarizer cube were placed in the collection path to control the polarization(s) of VSFG signal from the sample allowed to enter the detector. The polarizer cube was positioned to allow only *p*-polarized signal to pass to the detector, and was locked onto a delay stage that could be moved precisely in and out of the collection path. The waveplate was placed prior to the polarizer cube in the collection path. The position of waveplate that allowed only *s*-polarized signal to pass to the detector was determined by maximizing VSFG signal off of a gold mirror with the polarizer cube in place. Similarly, the position allowing only *p*-polarized signal to pass through was determined by minimizing the gold signal with the polarizer cube in place.

Nonresonant VSFG signal was suppressed by delaying the visible pulse relative to the IR pulse.[10] The amount of suppression for the spectra containing nonresonant signal was determined by collecting spectra at different delays until the spectra looked nonresonant free. The amount of suppression needed to eliminate detectible nonresonant signal was determined by increasing the delay until the signal looked nonresonant free, and then continuing to delay until the *ssp* and *psp* spectra matched.

3.3 Results and Discussion

3.3.1 Resonant Attenuation of Nonresonant Signal

A nonresonant signal, by definition, should produce a uniform intensity across all of frequency space, given probe beams of uniform intensity. In the case of broadband VSFG, a purely nonresonant spectrum, such as from an Au surface, should have the same spectral profile as the infrared beam; this approach is commonly used to characterize the infrared source. One must be careful, however, in assuming that the spectral profile measured from a metal surface is the exact profile that is used to generate a VSFG spectrum from the actual sample of interest. The infrared spectral profile can be modified by at least two processes. First, any resonant absorbers in the infrared beam path will alter the spectral profile that probes the surface of interest. Some of these absorbers may in fact not generate a VSFG signal, such as the CH_2 groups in all-*trans* chains,[34] but will selectively deplete the infrared light used to probe the surface. This is especially a concern with a thin film of material where the infrared beam can be absorbed on passage through the film before reaching the substrate. The second process that can affect the shape of the spectral profile is competition for intensity with the resonant signal. Both these processes are now explored with model spectra to see the effect they can have on the measured VSFG spectrum.

Figure 3.2 (a) shows a model nonresonant response, described by a single Gaussian peak centered at 3069 cm^{-1} with a full-width at half-max of 200 cm^{-1}. This is the type of signal that would be expected from a purely nonresonant surface, such as Au or Si. Figure 3.2 (b) shows how the VSFG spectrum would appear if a resonant absorber were placed in the IR beam path. A model resonant spectrum of polystyrene was used, with the amplitude chosen to illustrate an extreme case in which the most intense of the resonant peaks fully attenuates the nonresonant signal at that frequency. The dips in the nonresonant profile cause by resonant attenuation appear very similar to the destructive interference between resonant and nonresonant features that is typical of Au substrates,[3] although the cause in this case is fundamentally different.

For comparison, we now consider conventional interference between the resonant and nonresonant responses, where the infrared profile is or is not affected by resonant absorption. A model spectrum of the same resonant features from Figure 3.2 (b) interfering with the Gaussian nonresonant signal is shown in Figure 3.3. In this treatment, the infrared profile is not altered by absorption at the resonant frequencies.

Figure 3.4 (a) shows a model spectrum in which the resonant polystyrene signal interferes with the attenuated nonresonant signal from Figure 3.2 (b). Figure 3.4 (b) shows an experimental spectrum of a 220 nm polystyrene film on polished Si that was collected with no time delay of the visible pulse, such that the maximum nonresonant response is present. The presence of nonresonant signal in Figure 3.3 and both spectra of Figure 3.4 leads to some similarities between them, including the derivative line shapes and broadening of spectral features. These similarities between the spectra in Figure 3.3 and Figure 3.4 are indicators of the presence of nonresonant signal.

The challenge in interpreting such spectra, however, lies in how to properly model the nonresonant response. If there is no resonant attenuation in the nonresonant signal, then conventional approaches, such as measuring the infrared profile by up-conversion from an Au surface, can likely be used. However, if the nonresonant response has structure, it becomes incredibly difficult to accurately model that response. If the model of the nonresonant contribution is incorrect, then any determination of resonant parameters is compromised.[19,37] The imposition of structure on the infrared profile will also have consequences in the time-domain, as discussed in the next section. Ultimately, for the purpose of determining resonant parameters, it is better that the spectra be completely free of nonresonant contributions. Unfortunately, in some cases, it is possible for some nonresonant signal to be present, even in the absence of the typical indicators of nonresonant signal, which we now discuss.

3.3.2 Incomplete Suppression of Nonresonant Response

As discussed previously, the nonresonant response can be suppressed by delaying the visible probe pulse relative to the infrared probe pulse.[10] With this approach, one can generally tell that the nonresonant contribution has been removed by watching for certain indications. The first indicator is the lack of the broad quasi-Guassian pedestal on which the resonant features appear. The second indication is that any features that appeared with derivative line shapes on the nonresonant background will appear as symmetric peaks because the interference and resulting distortion has been removed. Unfortunately, these indicators are not always sufficient to guarantee that all the nonresonant contribution has been eliminated.

Figure 3.5 contains model polystyrene spectra produced in two ways. In the spectrum labeled "Nonresonant Suppressed", the visible beam is delayed in time by 500 fs to mostly suppress the nonresonant signal. The nonresonant signal is again modeled by the

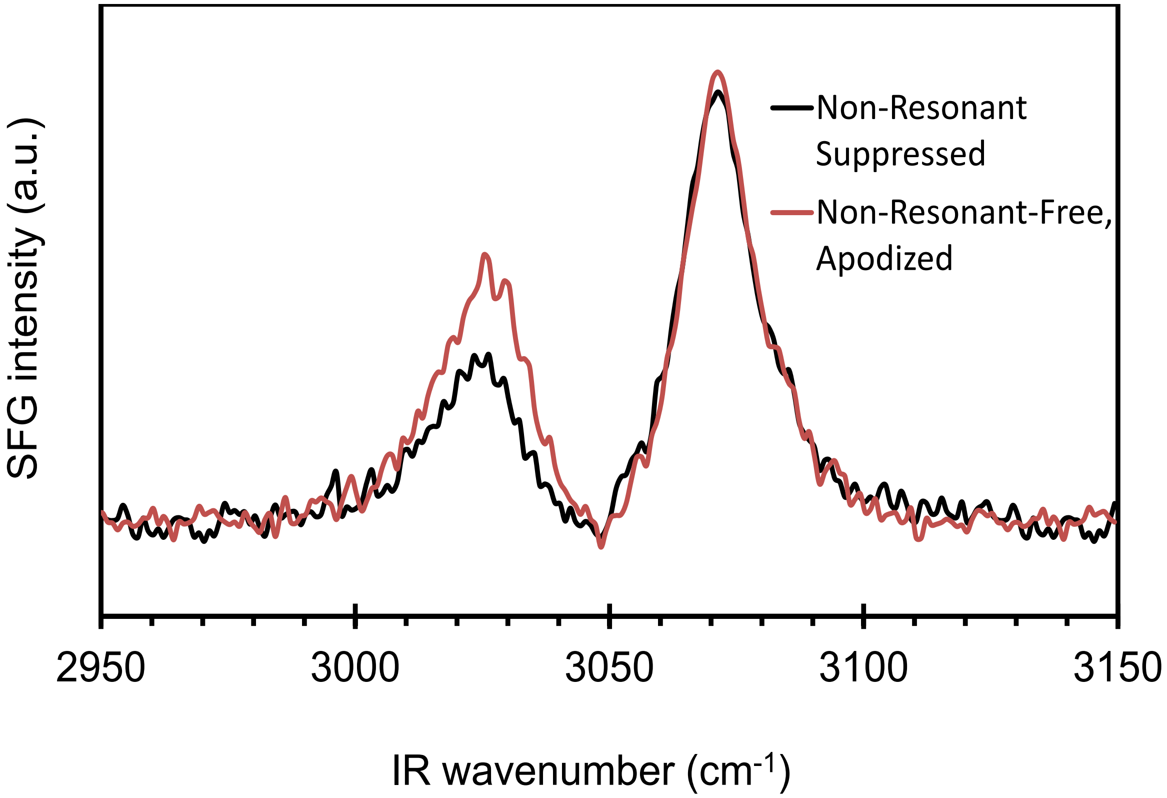

Figure 3.5 Model polystyrene spectra made by transforming a polystyrene spectrum with Gaussian nonresonant interference and a purely resonant polystyrene spectrum into the time domain, apodizing with a model visible pulse centered at 200 femtoseconds after the initial excitation, followed by a reverse transform to produce the frequency-domain spectrum.

Gaussian profile used in Figure 3.2 (a). Note the lack of dispersive line shapes and the absence of a broad pedestal in this spectrum, which could be interpreted as indicating a complete suppression of the nonresonant contribution. The spectrum labeled “Nonresonant-Free, Apodized” in Figure 3.5 was modeled with the same resonant response, but in this case no nonresonant contribution was included. The only effect of the delay of the visible pulse is to apodize the response in the time domain. As expected, there is no broad pedestal because no nonresonant contribution was included in the model.

For both spectra in Figure 3.5, the time delay was set to 500 fs; however, the two spectra exhibit significant differences. Note in particular that the relative intensities of the 3027 cm^{-1} peak and the 3069 cm^{-1} peak differ between the signal with nonresonant signal suppressed and the signal that never contained nonresonant signal. Since the relative intensities of those peaks can be used to determine molecular orientation, such an analysis of these two spectra would yield two different orientations despite the fact that the same underlying resonant signal, visible probe pulse, and up-conversion delay time were used to generate both spectra.

Although the obvious indicators of nonresonant signal, dispersive lineshape and a broad baseline, appear to be absent, the “Nonresonant Suppressed” spectrum is still influenced and distorted by a nonresonant contribution. The result of the interaction between these two contributions is a significant change in relative intensity. This is similar to what was seen in the case of functionalized fused silica surfaces, nonresonant signal can still be present, through the cross-term of Equation (3.2), even when the spectrum appears to be purely resonant.[17] Thus one could obtain a spectrum that appears to be free of a nonresonant response and erroneously analyze and interpret it. Although the bases of the peaks do appear slightly broader than in the nonresonant-free signal, in an actual experimental with any degree of noise, this subtle difference will likely not be observed. Great care must be exercised to be certain that a spectrum is, in fact, free of the nonresonant contribution; lack of the obvious indicators is not adequate.

Figure 3.6 shows the two model data sets represented from Figure 3.5 and the fits obtained using the built-in curve-fitting tool, cftool, in MATLAB to fit each to two lorentzian peaks. The nonresonant signal is clearly still present in data set (a) because it differs from the data set in which the spectrum was apodized but did not contain nonresonant signal. However, despite using the same purely-resonant model to obtain the fits for both spectra, good fits were obtained for both spectra. Results from fitting both spectra are shown in Table 3.1.

Nothing about the results of the fit would suggest that the model is incorrect, but the results are very different, particularly for the relative amplitudes of the two peaks. The difference in the apparent relative amplitude of the two peaks caused by the presence of nonresonant signal is significant, and would lead to a different interpretation of tilt angle, despite the two spectra containing exactly the same resonant signal and appearing free from nonresonant contributions. These results show that obtaining a good fit using a model that ignores nonresonant contributions is not sufficient to ensure that the collected signal is free from nonresonant interference.

Figure 3.7 shows the same two model spectra from Figure 3.5, but with a 2.3 ps delay for the visible up-converting pulse. The resulting spectra are significantly different from those collected with less delay of the up-converting pulse because a different part of the resonant FID is used in generating the sum-frequency signal. With the longer delay of the up-converting pulse, these two spectra are still free from the indicators of nonresonant signal, but the signal that contained a nonresonant contribution now more closely matches that obtained without a nonresonant contribution. Thus with a longer delay time, the model signal containing

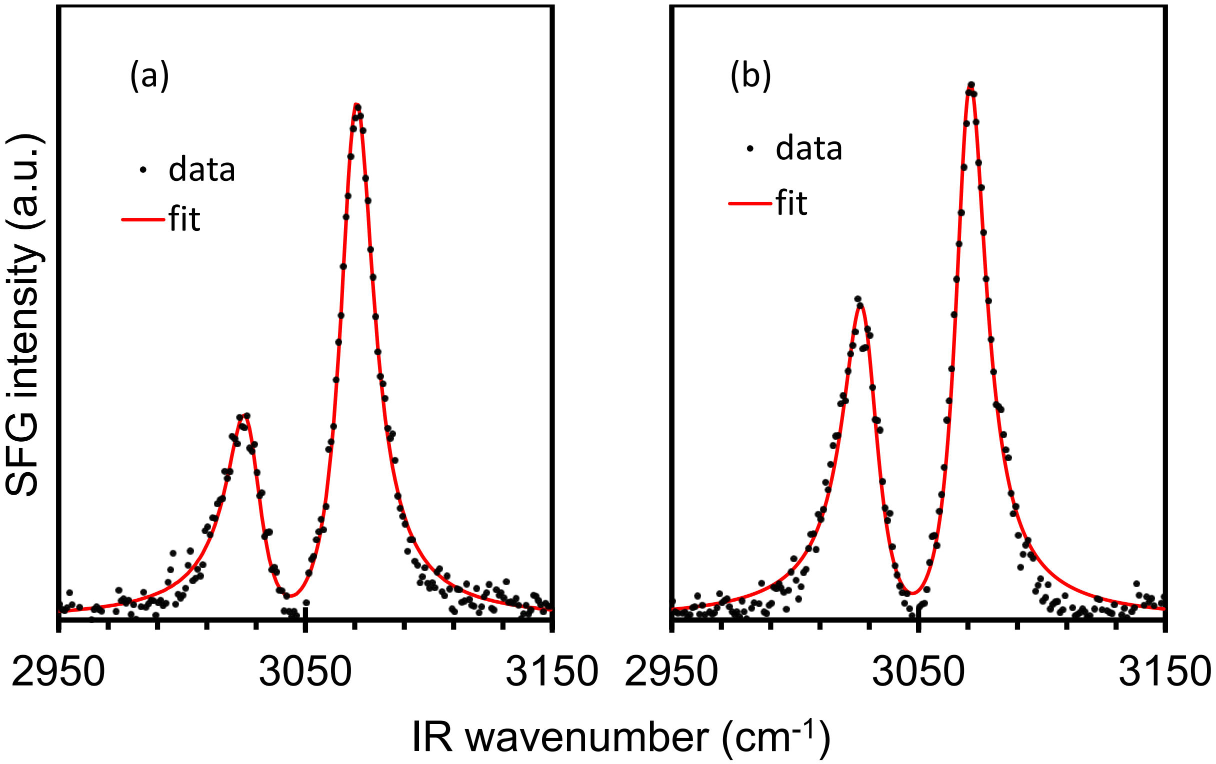

Figure 3.6 Model polystyrene spectra made by transforming a polystyrene spectrum with nonresonant interference (a) and a purely resonant polystyrene spectrum (b) into the time domain, then apodizing with a model visible pulse centered at 500 femtoseconds after the initial excitation. Good fits were obtained using MATLAB's built-in curve-fitting tool accounting for two resonant peaks and no nonresonant signal, despite the presence of nonresonant signal in Spectrum (a).

Table 3.1 Parameters obtained from fitting model data sets with identical resonant peak parameters to a model including two resonant Lorentzian peaks and no nonresonant contribution.

	ν_0 (cm^{-1})	Γ (cm^{-1})	A	A_{3027}/A_{3069}	R^2
NR Included	3070	8.422	0.9467	0.3231	0.9857
	3027	8.68	0.3059		
NR Free	3070	7.74	0.9491	0.5456	0.9805
	3028	8.843	0.5178		

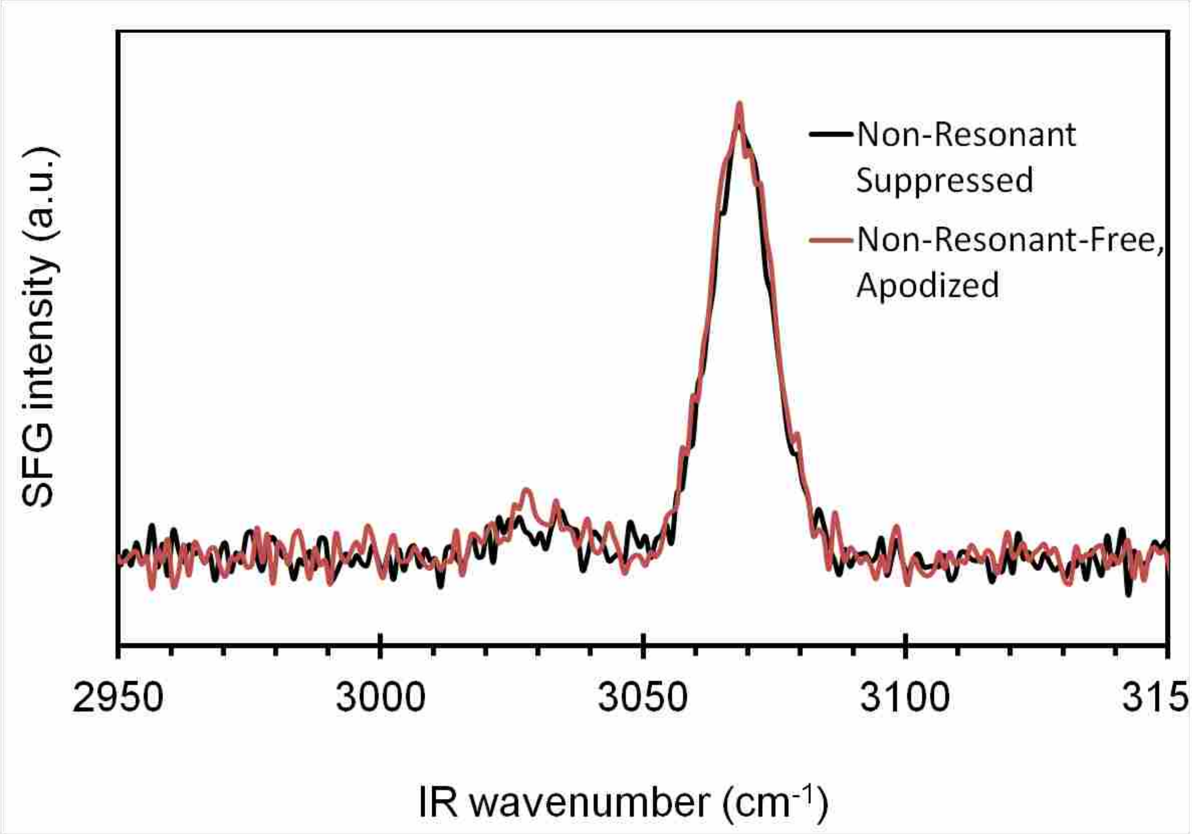

Figure 3.7 Model polystyrene spectra made by transforming a polystyrene spectrum with nonresonant interference and a purely resonant polystyrene spectrum into the time domain, then apodizing with a model visible pulse centered at 2.3 picoseconds after the initial excitation.

nonresonant interference more closely resembles the signal free from nonresonant contributions. Or, in other words, the more completely the nonresonant contribution is completely suppressed.

In our experience, a delay of only several hundred femtoseconds is not sufficient to fully suppress the nonresonant response, even though the spectra may appear to be free of nonresonant interference. We have also found that our variable time-delay method will simply not work if there is any nonresonant contribution present.[30] One point to mention is that in the model spectra, there was no inclusion of resonant attenuation of the infrared probe pulse. If such attenuation is happening in the actual experiment, the result will be to shape the infrared spectrum, which will also lengthen the pulse in time, meaning the nonresonant signal will persist longer than if such attenuation did not occur. The effect will also be most pronounced at the resonant frequencies, since that is where the shaping occurred in the frequency domain.

Of course, the optimal delay time will depend on the particular temporal profile of the visible pulse, thus each practitioner will need to determine the delay that is adequate for each individual VSFG system. It is particularly important to pay attention to the leading edge of this profile, which cannot be infinitely steep and will therefore sample some signal occurring before the maximum intensity of the visible pulse. We, therefore, urge caution and recommend using a longer delay than may be felt to be necessary to ensure complete suppression of the nonresonant response. As the delay time is increased, the overall signal intensity does drop, but that is a necessary trade-off to be certain that the measured spectrum is indeed free of the nonresonant response.

3.3.3 Polarization Considerations

One of the advantages of VSFG is that judicious combination of the input and output polarizations can be used to gain additional information about molecular orientations. The symmetry of the $\chi^{(2)}$ tensor, which governs second-order nonlinear processes including VSFG, limits the allowed polarization combinations. For example, when the visible and infrared inputs are respectively *s*-polarized and *p*-polarized, and the surface has azimuthal symmetry, the SFG light must be *s*-polarized; this is known as the *ssp* polarization combination. For our model system of spin-coated thin films of atactic polystyrene, the bulk is isotropic, but the surface is assumed to have azimuthal symmetry. Thus the resonant signal generated with *s*-polarized visible and *p*-polarized light must be of *s* polarization. It is not obvious, however, that the nonresonant signal is necessarily limited in this way because it can arise from the polymer surface, the substrate, or the polymer-substrate interface, with or without the presence of resonant peaks.

The surface of silicon (111) has three-fold symmetry with respect to rotation about the surface normal, not azimuthal symmetry. Therefore, the nonresonant signal coming from a silicon substrate could have a different polarization than the resonant and nonresonant signals coming from the polymer film. Thus, with *s*-polarized visible input and *p*-polarized infrared input, the azimuthally asymmetric components of the system may produce *p*-polarized light, or a *psp* spectrum. By selecting a single polarization of collected light (*s* or *p*), the signal generated by the substrate and any other parts of the sample that lack azimuthal symmetry may be isolated from the signal generated by azimuthally symmetric parts of the sample, or vice versa. Due to symmetry limitations on the signal generated by the polymer film, only nonresonant signal coming from the substrate should generate *psp* signal; therefore, a *psp* spectrum of this system should only contain nonresonant signal generated from the sample.

Figure 3.8 shows pure *psp* and pure *ssp* spectra of polystyrene on silicon obtained with no suppression of the nonresonant response. In these spectra, the central infrared frequency was

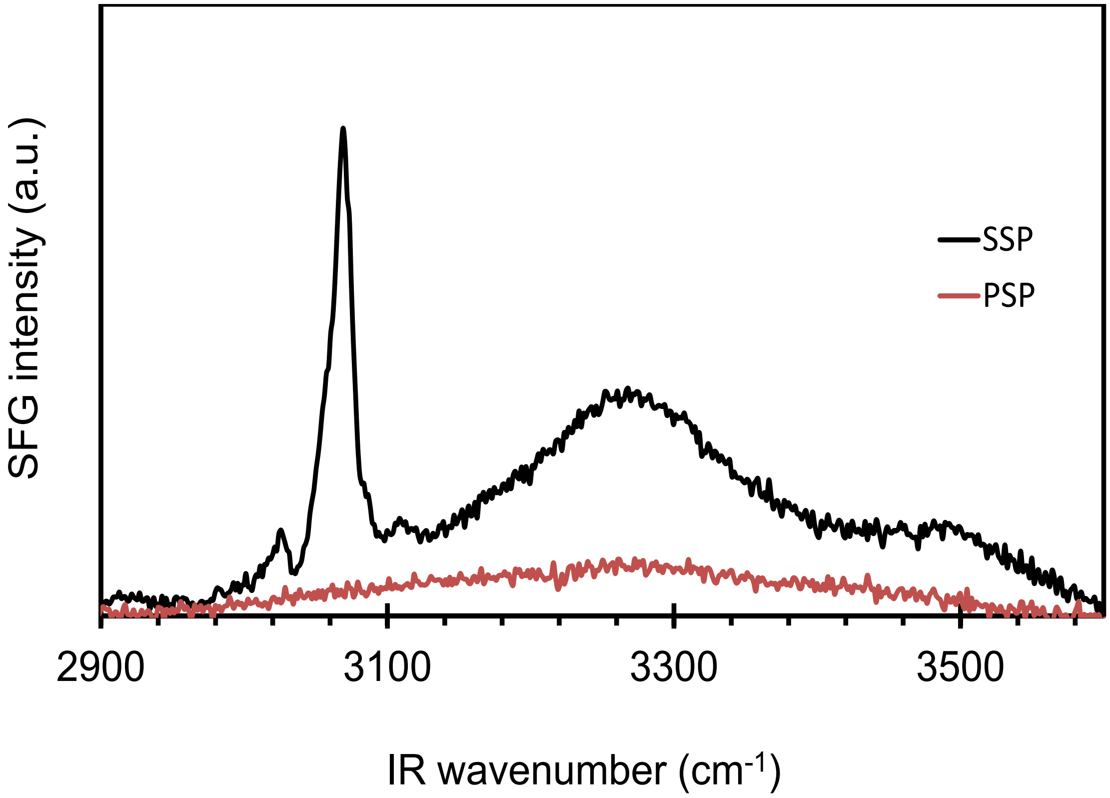

Figure 3.8 Slightly off-resonant scans of polystyrene on polished silicon with a polarization filter in place along the collection path to isolate the purely ssp spectrum (black) and the purely psp spectrum (red). The pure ssp spectrum shows resonant peaks and nonresonant signal, whereas the pure psp spectrum shows only nonresonant signal.

tuned to a slightly higher energy than the resonant features of polystyrene. The pure *psp* spectrum exhibits a featureless, quasi-Gaussian shape, and the pure *ssp* spectrum of the same sample contains resonant peaks overlaid on a broad nonresonant "background." As predicted by the symmetry of the sample, the *psp* spectrum contains only nonresonant signal, indicated by the featureless Gaussian shape typical of a purely nonresonant signal. Also predicted by symmetry arguments, the pure *ssp* spectrum contains both resonant and nonresonant contributions. This appears similar to what was seen with alkanethiol monolayers on Au, where multiple elements of $\chi_{NR}^{(2)}$ contributed to the measured SFG response.[42]

Figure 3.9 shows a spectrum of polystyrene on polished silicon where two etalons were used to spectrally narrow the visible beam, and the delay of the up-conversion pulse was adjusted such that the spectrum contained no nonresonant signal. With these conditions, there is no apparent difference between the filtered and unfiltered *ssp* spectra. This result provides further confirmation that the *psp* polarization combination contains only nonresonant signal, and the removal of the *psp* contribution has no effect on a purely resonant signal. Because of the symmetry of this system, therefore, we can selectively remove part of the nonresonant signal by removing the *psp*-polarized contribution from the total collected signal. This provides a tool by which we can detect the presence of nonresonant signal with any amount of up-conversion delay.

Although we cannot remove all nonresonant signal by removing the *p*-polarized portion of the "*ssp*-polarized" VSFG signal, doing so can reveal its presence. In our theoretical models, we saw that when the nonresonant signal is not fully suppressed, the relative amplitudes of peaks can be altered from what they should be in a signal that is free from nonresonant signal. Similarly, when *p*-polarized signal is selectively removed from a *ssp* VSFG spectrum and

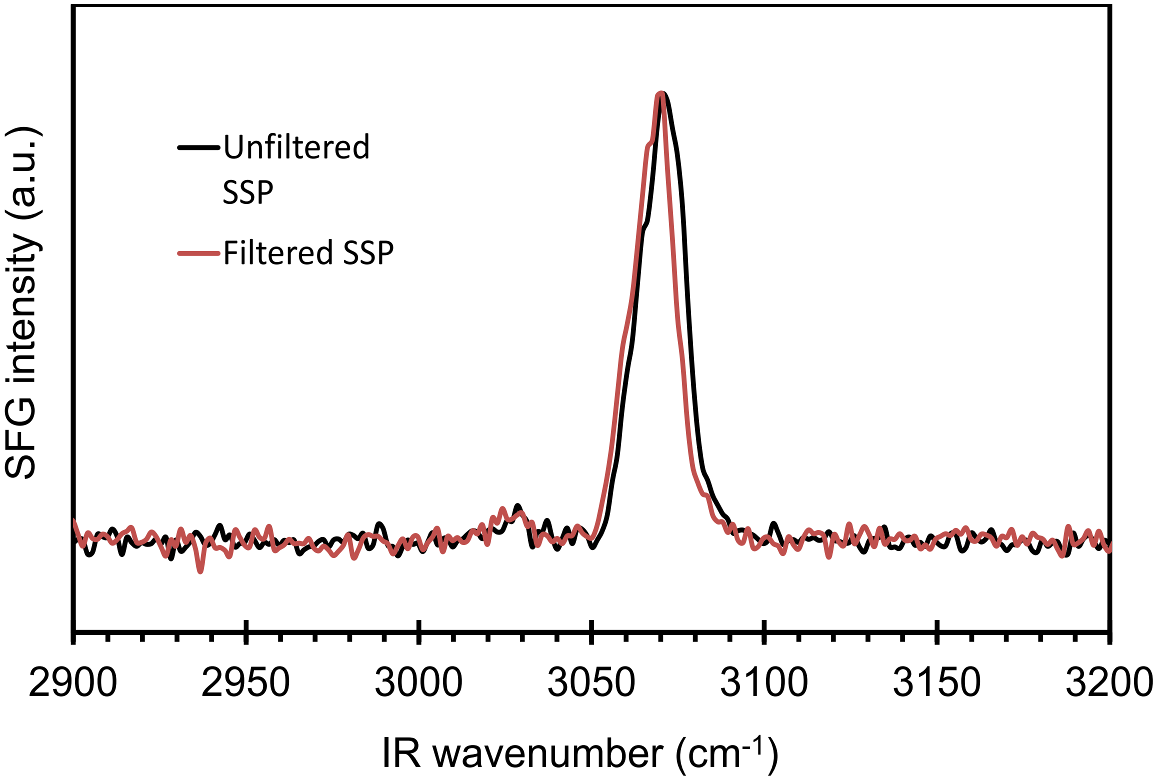

Figure 3.9 Sum-frequency generation spectrum of polystyrene with the nonresonant signal fully suppressed with (red) and without (black) the psp portions of the signal rejected by a polarization filter. The two signals are identical, which indicates that no signal is produced with the psp combination unless some nonresonant signal is present.

compared to the same experimental spectrum with the *psp* contribution included, the apparent relative peak amplitudes change.

Figure 3.10 shows the SFG spectrum of a polystyrene film on polished silicon with the temporal overlap between the visible and infrared pulses adjusted to give the maximum nonresonant signal. Filtering out the *p*-polarized signal reveals that the *psp* nonresonant signal has different phase characteristics than the *ssp* nonresonant signal. The *psp* signal interferes destructively at low frequency, but it interferes constructively at high frequency. Figure 3.11 shows an even more dramatic case of this type of interference. Cases may exist in which the relative peak amplitudes are unaffected by the presence of nonresonant signal; however, a change in apparent relative peak amplitudes after filtering the purely nonresonant *psp*-polarized part of the signal indicates that some nonresonant signal is present.

While it is standard practice to include an analyzing polarizer in the collection optics, we recommend either removing this polarizer or rotating it to select the orthogonal polarization as a means of determining whether a time-delayed VSFG spectrum is, in fact, free of nonresonant contributions. Observing no difference between a filtered and unfiltered *ssp* spectrum does not guarantee that there is no nonresonant contribution, but significant differences between filtered and unfiltered spectra are an indicator that some nonresonant signal is still present, and the delay of the visible pulse should be increased until the filtered and unfiltered spectra are the same.

As an additional example of how individual VSFG setups may require different delay times of the visible pulse, Figure 3.12 shows the sum-frequency generation spectra of a polystyrene coating on polished silicon collected with a 600 fs delay, but with only a single etalon used to spectrally narrow the up-converting visible beam. For the spectra in Figure 3.9, two etalons were used, which provided better spectral resolution than is seen with a single etalon.

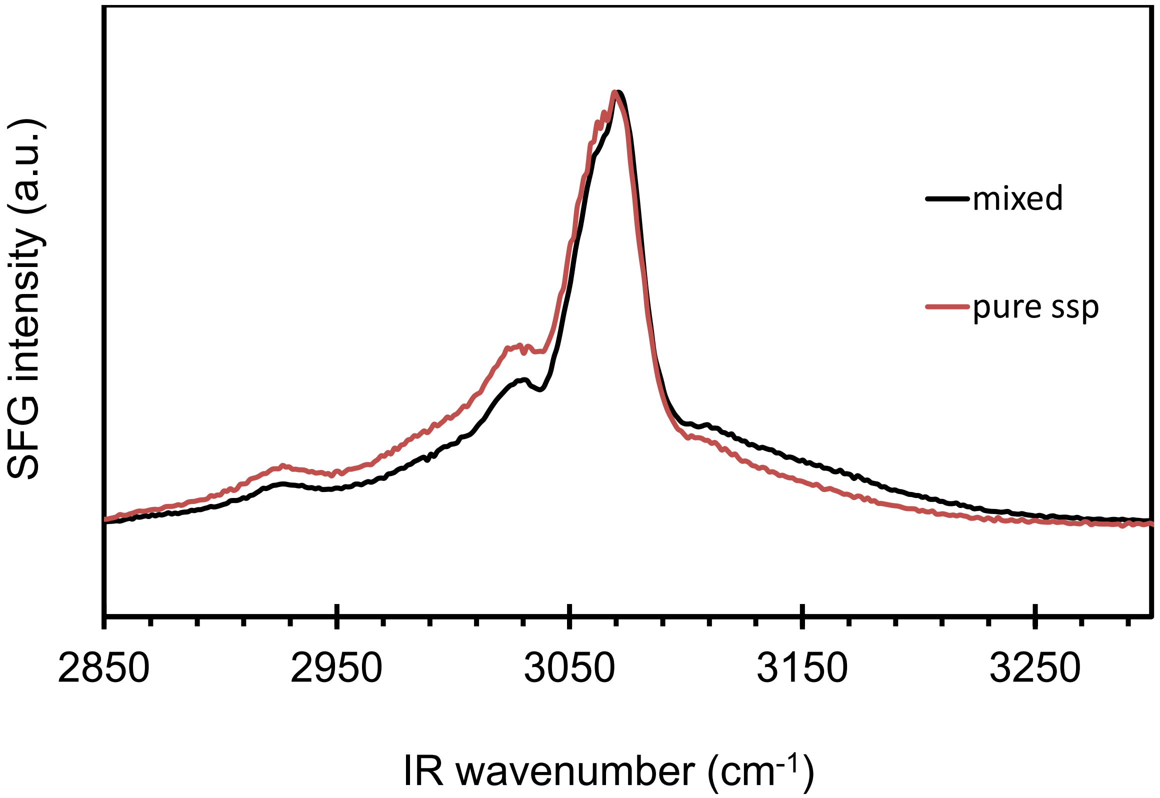

Figure 3.10 Sum-frequency generation spectrum of polystyrene with the nonresonant signal maximized with (red) and without (black) the psp portions of the signal rejected by a polarization filter. The two spectra show the differences in relative peak intensity caused by removal of part of the nonresonant signal.

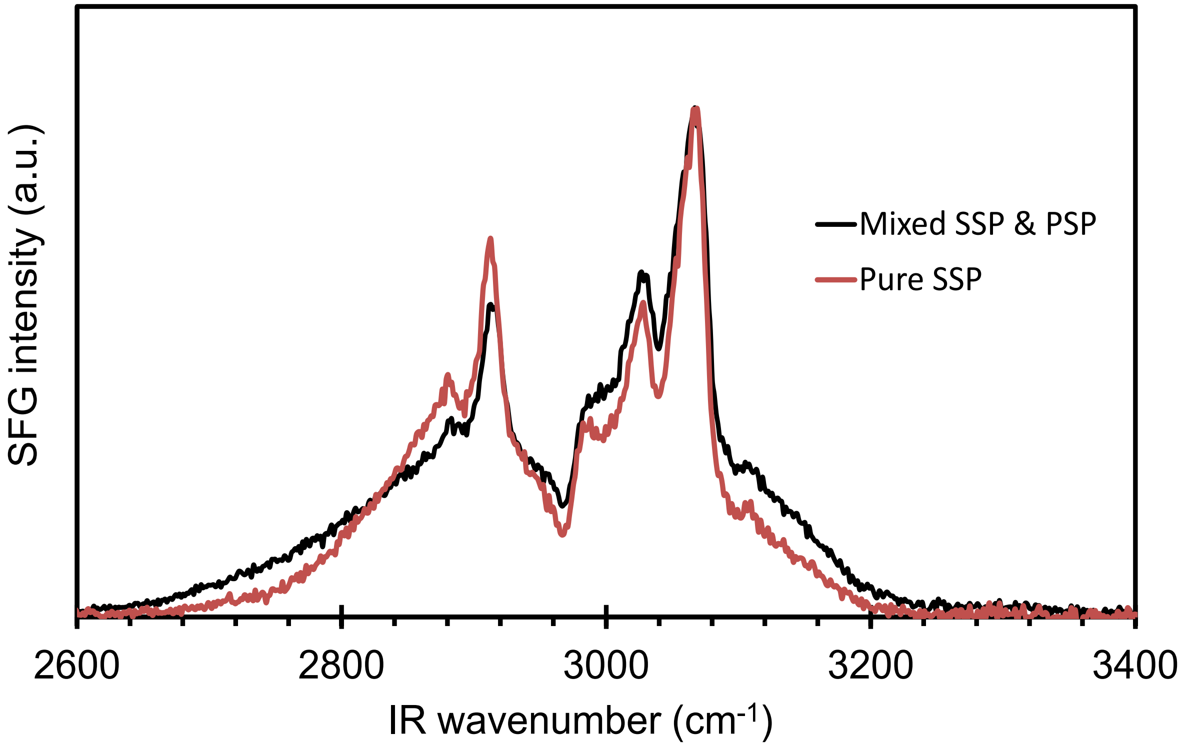

Figure 3.11 Spectra of an aged polystyrene film on silicon with aliphatic contamination, showing the frequency-dependence of the phase of the nonresonant signal relative to the resonant signal.

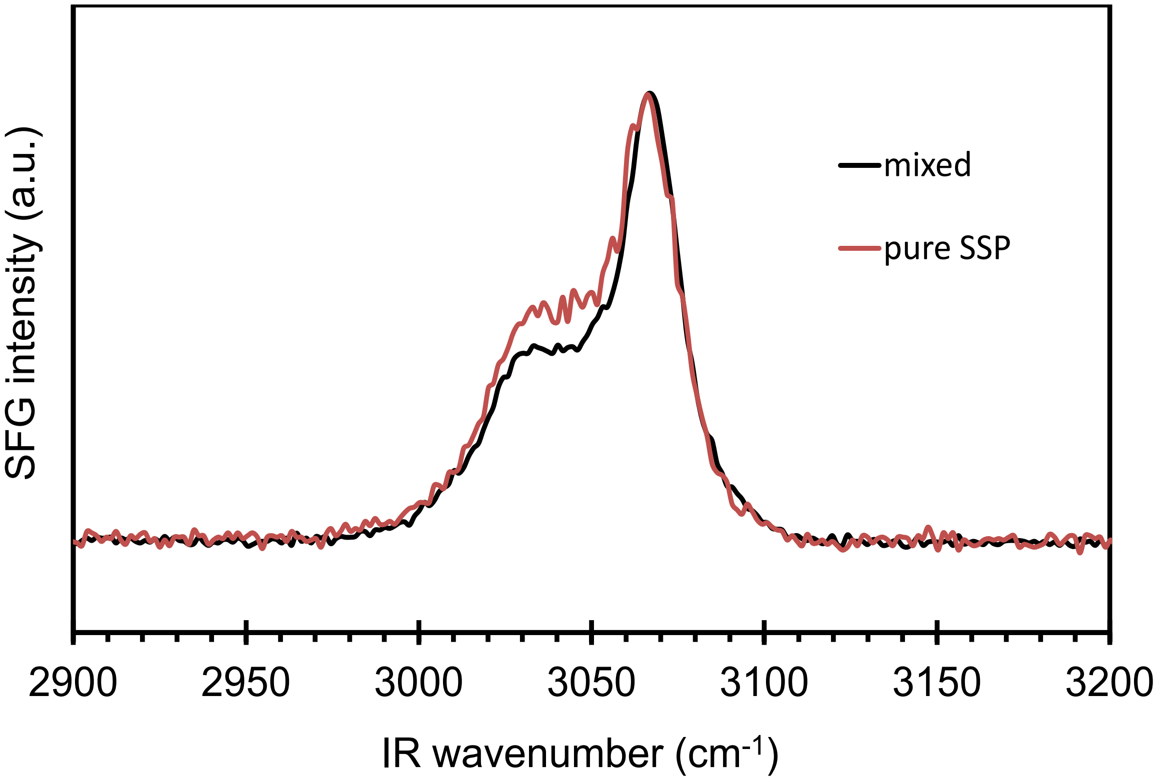

Figure 3.12 Sum-frequency generation spectrum of polystyrene with (red) and without (black) the psp portions of the signal rejected by a polarization filter. To collect each spectrum, the visible pulse was delayed until indicators of nonresonant signal were no longer apparent. The differences between the two spectra indicate that the suppression of nonresonant signal was incomplete.

This delay time was chosen because all the obvious indicators of nonresonant interference are absent. Both spectra in Figure 3.12 look to be free of nonresonant signal; in particular, the broad pedestal is completely lacking. However, the change in relative peak amplitude when the *psp*-polarized light is removed indicates that some nonresonant signal is still present.

3.3.4 General Considerations and Recommendations

The presence of nonresonant signal invariably distorts the resonant response, which can lead to erroneous determinations of relative intensities, which leads to incorrect interpretations of molecular orientation. Reliable analysis of sum-frequency generation spectra therefore requires the complete removal of the nonresonant signal; however, confirming the full removal of nonresonant signal can be challenging. As these results show, it is possible to collect spectra that appear free of nonresonant signal, but that actually do contain some nonresonant contribution at the resonant frequencies.

Suppression of the nonresonant response by introducing a time delay between the infrared and visible pulses is a viable approach to produce a purely resonant spectrum. Sufficient delay must be introduced in order to have confidence in the results obtained from any analysis of the measured spectrum. The ideal time delay of the visible pulse is that in which the measured response identically matches the apodized resonant signal without nonresonant interference. Unfortunately, such a comparison is not possible under actual experimental conditions because signals that are intrinsically nonresonant-free can only exist theoretically.

Checking for nonresonant signal in a “forbidden” polarization is one method that can be used to determine if nonresonant signal is still present, even with a time-delayed visible pulse. If the spectra appear different when the forbidden polarization is included, that is an indication that some nonresonant signal is part of the measured response. This approach is most likely to be viable with an azimuthally symmetric surface and a crystalline substrate, such as polymer thin films on polished Si. In systems with an amorphous substrate, however, the *psp* nonresonant signal will likely not be seen; the same symmetry considerations will apply to the surface of interest and the substrate. For chiral systems, the surface itself can produce signal in the *psp* polarization combination,[43] so this approach is also unlikely to be successful in that case. In any case, it should be noted that this polarization method can indicate the presence of nonresonant signal, but it cannot definitively prove the absence of nonresonant signal.

3.4 Conclusions

The presence of nonresonant signal in VSFG spectra impedes accurate analysis, and several methods have been developed to obtain spectra free from nonresonant interference. One method used to remove nonresonant signal from spectra is to experimentally suppress the response by delaying the upconverting pulse in time with respect to the initial excitation to a time after the nonresonant part of the signal has dephased. Although the presence or absence of nonresonant signal is often judged based on the presence or absence of typical indicators, such as a broad pedestal at the base of resonant peaks and dispersive line shapes, this method can be misleading.

We have shown through both theoretical modeling in MATLAB and experimental data comparing the signal from "allowed" and "forbidden" polarizations that the absence of nonresonant indicators does not necessarily prove that spectra are free from nonresonant signal. The presence of nonresonant signal alters the apparent relative peak amplitudes in spectra, which confounds accurate analysis of molecular orientation. Despite significant differences in the parameters obtained by fitting to an equation accounting for only resonant peaks, the goodness of fit is similar for both spectra. Fitting alone is unable to confirm either the presence or absence of nonresonant signal in the spectrum.

Although comparing an experimentally apodized spectrum at a given upconversion delay to the apodized purely resonant spectrum is impossible, the relationship between the symmetry of the sample and allowed polarization combinations sometimes allows the isolation of nonresonant signal at any upconverstion delay by rotating and/or filtering the signal produced at the sample. In our example of atactic polystyrene films on silicon (111) substrate, signal resulting from the *psp* combination of polarizations contains only nonresonant signal, whereas the *ssp* combination contains both resonant and nonresonant parts. When the *psp* combination is experimentally filtered out of a nominally *ssp* spectrum free from nonresonant contribution, the resulting spectrum is identical to the unfiltered spectrum. However, when the signal from this system does contain nonresonant contributions, the relative peak amplitudes and widths change when the *psp* contribution is filtered from the spectrum. Using this method, we showed experimentally that it is possible to collect experimental spectra free of nonresonant indicators that contain nonresonant signal.

At long enough delay times, it is possible to remove nonresonant signal, but knowing how much delay is enough can pose a challenge. The optimal delay between the two pulses depends on the duration of the nonresonant response in the time domain and the time domain shape of the visible pulse. The proper delay must be determined for each system under study and for each SFG system. However, the fact that nonresonant signal can be present in the absence of obvious indicators complicates such a determination. The selective polarization method we have demonstrated here provides an additional way to check for nonresonant signal. Although the method demonstrated here does not absolutely ensure the absence of nonresonant signal, it does provide an additional way to check for nonresonant signal in VSFG data.

**This work was done in conjunction with Alex Curtis and Shawn Averett, who contributed to the modeling of spectra and the development of the polarization method for checking for the presence of nonresonant signal, respectively.*

3.5 References

(1) Zhu, X. D.; Suhr, H.; Shen, Y. R. *Phys. Rev. B*. **1987**, *35*, 3047.

(2) Shen, Y. R. *Nature* **1989**, *337*, 519.

(3) Bain, C. D. *J. Chem. Soc., Faraday Trans.* **1995**, *91*, 1281.

(4) Buck, M.; Himmelhaus, M. *J. Vac. Sci. Technol., A* **2001**, *19*, 2717.

(5) Williams, C. T.; Beattie, D. A. *Surface Science* **2002**, *500*, 545.

(6) Richmond, G. L. *Chem. Rev.* **2002** *102*, 2693.

(7) Chen, Z. *Polymer International* **2007**, *56*, 577.

(8) Van Der Ham, E. W. M.; Vrehen, Q. H. F.; Eliel, E. R. *Opt. Lett.* **1996**, *21*, 1448.

(9) Richter, L. J.; Petralli-Mallow, T. P.; Stephenson, J. C. *Opt. Lett.* **1998**, *23*, 1594.

(10) Lagutchev, A.; Hambir, S. A.; Dlott, D. D. *J. Phys. Chem. C* **2007**, *111*, 13645.

(11) Roke, S.; Kleyn, A. W.; Bonn, M. *Chem. Phys. Lett.* **2003**, *370*, 227.

(12) Malyk, S.; Shalhout, F. Y.; O'Leary, L. E.; Lewis, N. S.; Benderskii, A. V. *J. Phys. Chem. C* **2013**, *117*, 935.

(13) Zheng, W. Q.; Pluchery, O.; Tadjeddine, A. *Surf. Sci.* **2002**, *502-503*, 490.

(14) Baldelli, S.; Gewirth, A. A. *Adv. Electrochem. Sci. Eng.* **2006**, *9*, 163.

(15) Shaw, S. K.; Lagutchev, A.; Dlott, D. D.; Gewirth, A. A. *J. Phys. Chem. C* **2009**, *113*, 2417.

(16) Hayes, P. L.; Chen, E. H.; Achtyl, J. L.; Geiger, F. M. *J. Phys. Chem. A* **2009**, *113*, 4269.

(17) Quast, A. D.; Curtis, A. D.; Horn, B. A.; Goates, S. R.; Patterson, J. E. *Anal. Chem.* **2012**, *84*, 1862.

(18) Curtis, A. D.; Reynolds, S. B.; Calchera, A. R.; Patterson, J. E. *J. Phys. Chem. Letters* **2010**, *1*, 2435.

(19) Curtis, A. D.; Burt, S. R.; Calchera, A. R.; Patterson, J. E. *J. Phys. Chem. C* **2011**, *115*, 11550.

(20) Guyot-Sionnest, P.; Shen, Y. R. *Phys. Rev. B* **1986**, *33*, 8254.

(21) Guyot-Sionnest, P.; Shen, Y. R. *Phys. Rev. B Condens. Matter* **1987**, *35*, 4420.

(22) Guyot-Sionnest, P.; Shen, Y. R. *Phys. Rev. B* **1988**, *38*, 7985.

(23) Held, H.; Lvovsky, A. I.; Wei, X.; Shen, Y. R. *Phys. Rev. B Condens. Matter Mater. Phys.* **2002**, *66*, 205110.

(24) Morita, A. *Chem. Phys. Lett.* **2004**, *398*, 361.

(25) Yamaguchi, S.; Shiratori, K.; Morita, A.; Tahara, T. *J. Chem. Phys.* **2011**, *134*, 184705/1.

(26) Kazuya, S.; Yamaguchi, S.; Tahara, T.; Morita, A. *J. Chem. Phys.* **2013**, *138*, 064704/1.

(27) Shen, Y. R. *J. Phys. Chem. C* **2012**, *116*, 15505.

(28) Laaser, J. E.; Xiong, W.; Zanni, M. T. *J. Phys. Chem. B* **2011**, *115*, 2536.

(29) Stiopkin, I. V.; Jayathilake, H. D.; Weeraman, C.; Benderskii, A. V. *J. Chem. Phys.* **2010**, *132*, 234503/1.

(30) Curtis, A. D.; Asplund, M. C.; Patterson, J. E. *J. Phys. Chem. C* **2011**, *115*, 19303.

(31) Ji, N.; Ostroverkhov, V.; Chen, C.-Y.; Shen, Y.-R. *J. Am. Chem. Soc.* **2007**, *129*, 10056.

(32) Ward, R. N.; Davies, P. B.; Bain, C. D. *J. Phys. Chem.* **1993**, *97*, 7141.

(33) Zhuang, X.; Miranda, P. B.; Kim, D.; Shen, Y. R. *Phys. Rev. B: Condens. Matter Mater. Phys.* **1999**, *59*, 12632.

(34) Bredenbeck, J.; Ghosh, A.; Nienhuys, H.-K.; Bonn, M. *Acc. Chem. Res.* **2009**, *42*, 1332.

(35) Mukamel, S. *Principles of Nonlinear Optical Spectroscopy*; Oxford University Press, Inc.: New York, New York, 1995.

(36) Shalhout, F. Y.; Malyk, S.; Benderskii, A. V. *J. Phys. Chem. Lett.* **2012**, *3*, 3493.

(37) Busson, B.; Tadjeddine, A. *J. Phys. Chem. C* **2009**, *113*, 21895.

(38) Meier, R. J. *Vib. Spectrosc.* **2005**, *39*, 266.

(39) Curtis, A. D.; Asplund, M. C.; Patterson, J. E. *J. Phys. Chem. C* **2011**, *115*, 19303.

(40) Curtis, A. D.; Brigham Young University: 2012.

(41) Curtis, A. D.; Reynolds, S. B.; Calchera, A. R.; Patterson, J. E. *J. Phys. Chem. Lett.* **2010**, *1*, 2435.

(42) Tanaka, Y.; Lin, S.; Aono, M.; Suzuki, T. *Appl. Phys. B: Lasers Opt.* **1999**, *68*, 713.

(43) Fu, L.; Liu, J.; Yan, E. C. Y. *J. Am. Chem. Soc.* **2011**, *133*, 8094.

Chapter 4: Plasma Treatment of Polystyrene Thin Films Affects More than the Surface

*Reproduced with permission from Calchera, A.R.; Curtis, A.D.; Patterson, J. E.

ACS Appl. Mater. Interfaces, ***2012***, 4 (7), 3493-3499. ©2012 American Chemical Society

4.1 Abstract

Plasma treatment of polymer materials introduces chemical functionalities and modifies the material to make the native hydrophobic surface more hydrophilic. It is generally assumed that this process only affects the surface of the material. We used vibrationally-resonant sum-frequency generation spectroscopy to observe changes in the orientation of phenyl groups in polystyrene (PS) thin films on various substrates before and after plasma treatment. VR-SFG selectively probes regions of broken symmetry, such as surfaces, but can also detect the emergence of anisotropy. On dielectric substrates, such as fused silica, the spectroscopic peak corresponding to the symmetric stretching (ν_2) mode of the phenyl rings was undetectable after plasma treatment, showing that surface phenyl rings were altered. This peak also diminished on conducting substrates, but the intensity of another peak corresponding to the same mode in a bulk-like environment increased significantly, suggesting that plasma treatment induces partial ordering of the bulk polymer. This ordering is seen on conducting substrates even when the polymer is not directly exposed to the plasma. Annealing reverses these effects on the polystyrene bulk, however, the surface phenyl rings do not return to the orientation observed for untreated films. These results call into question the assumption that the effects of plasma treatment are limited to the free surface and opens up other possibilities for material modification with low temperature plasmas.

KEYWORDS: Surface modification; molecular orientation; plasma treatment; bulk polymer modification; sum frequency generation; field-responsive polymers

4.2 Introduction

Exposure to an air- or oxygen-plasma induces a variety of modifications in polymers at a low cost and with minimal environmental impact. These modifications include removal of surface contaminants, polymerization of monomers, cross-linking of polymer chains, etching away thin layers of polymer, functionalizing polymer surfaces, and improved hydrophilicity of the surface.[1] Because of the versatility, economy, and environmental cleanliness of the process, plasma treatment is often preferred over other modification methods and has become a common processing step in a variety of applications.

Plasma treatment of polymers commonly invokes the assumption that only the free surface is modified. In fact, the purported surface specificity of plasma treatment is often identified as an advantage of the technique. This surface-specificity is of particular importance in cases where the native bulk properties of the polymer play an important role in its ultimate application. However, even if the only aim of the treatment is to alter the surface chemistry, the bulk properties of the polymer can still influence the surface properties. For example, plasma treatment of polydimethylsiloxane induces a difference in the surface and bulk modulus that results in cracking, which causes the cracked surface to be more hydrophobic than surfaces without cracks.[2]

We used vibrationally-resonant sum-frequency generation (VR-SFG) spectroscopy[3] to study changes in the orientation of the phenyl rings of polystyrene (PS) in response to plasma treatment. In VR-SFG, two beams from a pulsed laser overlap spatially and temporally at the sample, generating a new beam with a frequency equal to the sum of the two input frequencies.

VR-SFG spectra give both compositional and orientational information about the molecules in the sample. Additionally, unlike linear vibrational spectroscopies such as FTIR and Raman that probe all molecules in the sample, VR-SFG signal originates only from locations in the sample that lack inversion symmetry. When the bulk of the material is largely isotropic, this technique can be used to selectively probe molecules at surfaces and interfaces. However, because the molecules probed with VR-SFG are selected by symmetry and not proximity to the free surface, it also has the advantage of detecting signal from other regions of broken symmetry. This means that when areas of broken symmetry are present in sub-surface regions, VR-SFG probes deeper into the material than surface-specific techniques such as XPS or TOF-SIMS.

Previous VR-SFG studies of plasma-treated PS films used fused silica substrates and reported a loss of signal intensity that they attributed to destruction of phenyl rings on the polymer surface.[4-6] In our more comprehensive study, which included the use of multiple substrates and removal of nonresonant interference, we have seen that this understanding is incomplete. Although some destruction of the phenyl rings certainly occurs on all substrates, we show here that the more dominant change on conducting substrates is a reorientation of the bulk polymer material.

In a study by Poncin-Epaillard *et al.*,[7] the response of isotactic polypropylene films exposed to microwave plasmas affected the orientation of the polymer bulk, although these polymer films already had some crystalline character prior to plasma exposure. Our study with atactic PS demonstrates that bulk polymer orientation can be affected by plasma treatment even when the polymer initially lacks long-range order. Although the previous study proposed that the changes they observed in the bulk were caused by exposure of the polymer to high levels of vacuum ultraviolet (VUV) radiation present in the treatment chamber, we show that such exposure does not significantly influence the bulk structure of the polymer in our experiments. We additionally show that the effects of plasma treatment depend on the substrate used to support the films, that bulk modification occurs with short treatment times (~1 s), and that the modifications to polymer bulk require 80% less power in the plasma than reported in the previous study. In light of the information presented here, common assumptions about the surface-specificity of the plasma treatment process need to be revised.

4.3 Experimental Methods

Silicon, sapphire, and fused silica substrates were cleaned by immersion in piranha solution (18 M sulfuric acid and 30% hydrogen peroxide, 3:1 by volume) for one hour. (*Cautionary Note*: Piranha solution is very corrosive, and extreme care must be used when handling.) The substrates were then rinsed with Millipore-purified water (18 MΩ), then immersed in Millipore-purified water for at least one hour. Immediately prior to coating with polymer, substrates were dried under a stream of nitrogen gas. Stainless steel mirrors (24 gauge, Mirrored Stainless Solutions) were prepared simply by removing the protective plastic backing just prior to spin-coating to avoid the risk of rusting in piranha solution.

Substrates were spin-coated with PS (M_w=230,000 from Aldrich) solution in toluene (UltimAR® from Mallinckrodt Chemicals) with a spin-coater (Model WS650SZ-6NPP/A1/AR1 from Laurell Technologies) to give ~100 nm thick films. For certain samples, poly(methyl methacrylate) (M_w=120,000 from Aldrich) was spin coated on top of PS from a nitromethane (spectrograde from Fisher Scientific) solution to give ~150 nm thick films. Film thicknesses were determined using spectroscopic ellipsometry (M-2000 from J. A. Woollam Co., Inc.).

Solvent-cast PS samples were prepared by dispensing a solution of PS in toluene to cover the surface of the substrate, then allowing the solvent to evaporate for at least 24 hours. 2% wt.

PS was used to collect the data reported here, but similar results were obtained independent of solution concentration.

Plasma treatment was performed with an 18 W RF plasma from a Harrick Plasma basic plasma cleaner (PDC-32G). Plasma was generated in the evacuated chamber (~200 mtorr), bleeding in room air as necessary to sustain the plasma. Unless otherwise stated, the plasma was sustained for 1 s to treat each sample. Measurement of film thickness following 1 s of plasma treatment shows that the etching of polymer causes a negligible (less than 1 nm) decrease in thickness.

VR-SFG spectroscopy was performed using the set-up described in detail elsewhere.[8] The system uses an amplified femtosecond laser (Quantronix, Integra C) that is split into two beams. One beam is spectrally narrowed with two Fabry-Perot etalons for use as the upconverting visible beam. The other is used to pump an optical parametric amplifier (Light Conversion via Quantronix, TOPAS-C) to generate broadband infrared light. All spectra were collected using the *ssp* (*s*-polarized SFG output, *s*-polarized visible input, *p*-polarized IR input) polarization combination. Nonresonant VR-SFG signal was suppressed by delaying the visible pulse relative to the IR pulse by approximately 2 ps.[9] All spectra presented together in a single figure were collected on the same day with the same degree of nonresonant suppression.

Freshly prepared samples were scanned with VR-SFG within 48 hours of coating. Freshly plasma-treated samples were scanned immediately after treatment. Annealed samples were stored in a vacuum oven heated to 120˚C for 24 hours, then cooled slowly to room temperature over a period of 24 hours before being scanned.

4.4 Results & Discussion

4.4.1 Effects of Plasma on Bulk Polystyrene

As shown in Figure 4.1, the VR-SFG spectrum of an untreated PS thin film contains two readily distinguishable features: a prominent peak at 3069 cm^{-1} assigned to the phenyl ν_2 mode, and a less intense peak at 3027 cm^{-1} assigned to the ν_{20b} mode.[10] Our discussion will also focus on a much smaller peak centered around 3059 cm^{-1}, assigned to the ν_2 mode in a more densely-packed environment.[11] Although the ν_2 peak at 3059 cm^{-1} is usually weak in VR-SFG spectra of untreated PS, the IR spectrum of PS shows a strong peak attributed to the ν_2 stretching mode around 3060 cm^{-1} with no peak present at 3069 cm^{-1}. The linear spectroscopic technique is sensitive to the bulk, whereas VR-SFG is more sensitive to the surface, assuming the bulk is completely isotropic. Resonant spectra of untreated PS films are identical on all substrates, as shown previously[8] and again confirmed in this study.

Following plasma treatment of PS on silicon, the peak at 3069 cm^{-1} decreases in intensity, and the peak at 3059 cm^{-1} increases in intensity, as shown in Figure 4.1. The change in the intensities of the ν_2 peaks corresponds to a change in the type of phenyl rings that contribute to the measured spectrum. Prior to plasma treatment, the signal from the surface phenyl rings dominates, whereas after plasma treatment, the signal from more densely-packed, bulk-like phenyl rings dominates. Because randomly oriented phenyl rings cannot produce VR-SFG signal, the observation of phenyl rings in the bulk suggests that the bulk of the polymer is no longer completely isotropic.

Not only is a change in the relative intensities of the ν_2 peaks observed following plasma treatment, but this change is also typically accompanied by a significant increase in absolute VR-SFG intensity, also shown in Figure 4.1. Even samples that normally do not produce any

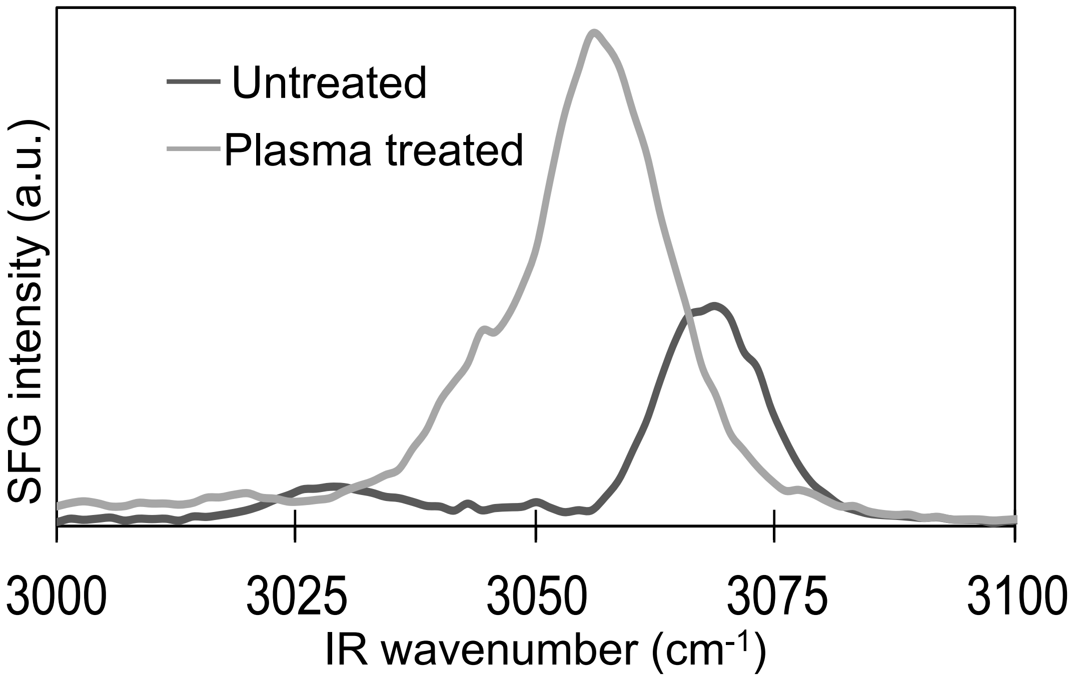

Figure 4.1 VR-SFG spectra (ssp polarization combination) of untreated and plasma-treated PS. Untreated PS exhibits a strong peak at 3069 cm^{-1} and a weaker peak at 3059 cm^{-1}. After plasma treatment, the 3069 cm^{-1} peak corresponding to surface phenyl rings is no longer detected and the 3059 cm^{-1} peak, corresponding to bulk phenyl rings, increases in intensity.

resonant VR-SFG signal, such as the solvent-cast PS shown in Figure 4.2, exhibit a discernible VR-SFG peak at 3059 cm^{-1} after plasma treatment for 10 seconds. The increase in absolute VR-SFG intensity supports the idea that previously unordered bulk PS becomes ordered to some degree with plasma treatment; the greater abundance of bulk phenyl rings compared to surface groups gives rise to a larger signal. Although this increase in signal strength occurs with many samples, the magnitude of the effect varies from sample to sample. This variability likely originates from factors beyond our control, such as an intensity gradient within the plasma treatment chamber, the exact placement of the sample in the cylindrical sample chamber, slight variations in polymer thickness, and/or slight variations in the time of plasma treatment.

Our investigation of layered polymers on silicon substrates further confirms that phenyl rings of PS are aligned by plasma treatment. An additional 150 nm of poly-methyl-methacrylate (PMMA) was coated on top of PS prior to plasma treatment. The spectra collected before and after plasma treatment are shown in Figure 4.3. Prior to plasma treatment, the response of PS is too weak to be seen; however, after plasma treatment the peak at 3059 cm^{-1} becomes apparent, and the PMMA peak at about 2950 cm^{-1} also increases in intensity. Because the thickness change from the plasma exposure is negligible compared to the total thickness of the PMMA film, the observed structural modification of PS in these samples was achieved without direct exposure of PS to the plasma.

4.4.2 Determining Relative Orientations from VR-SFG Data

Use of polarized light in VR-SFG experiments allows orientational information to be extracted from the spectra. Assuming free rotation about the axis of the bond that attaches the phenyl group to the polymer chain, and assuming complete azimuthal symmetry, the relative

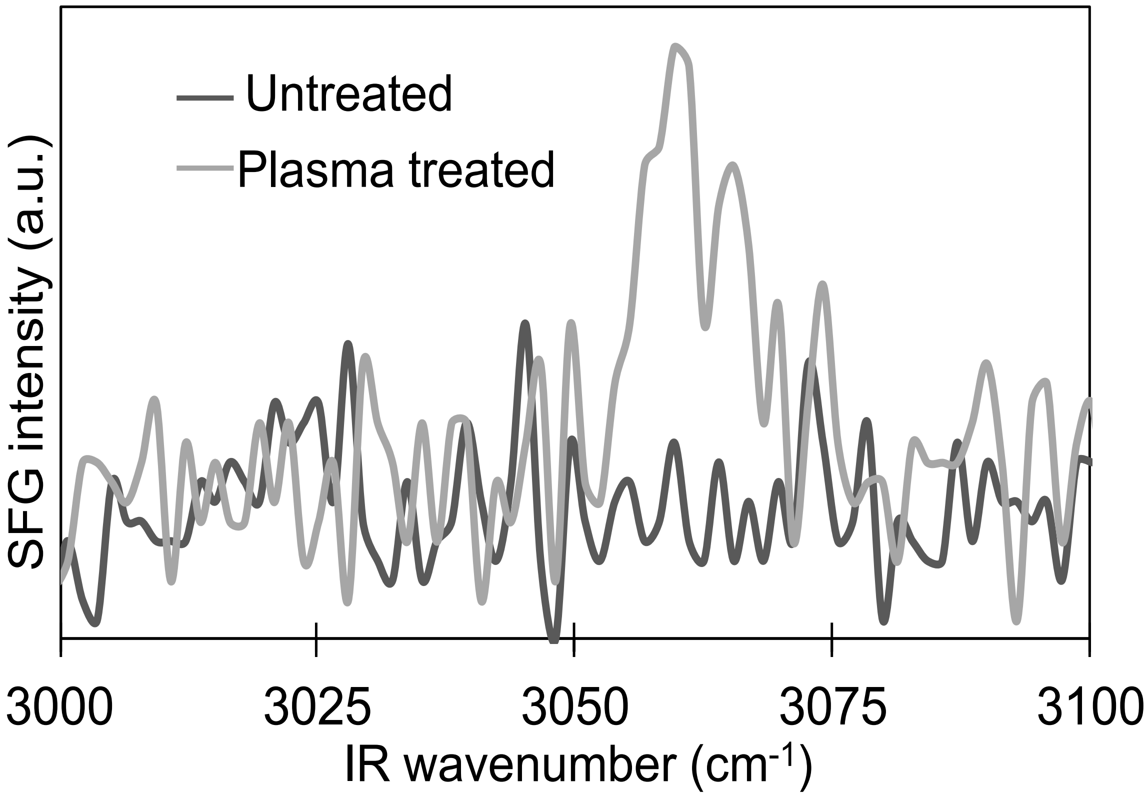

Figure 4.2 VR-SFG spectra of a PS thin film solvent cast onto polished silicon before and after plasma treatment. Untreated solvent-cast samples give no resonant VR-SFG signal; however, after 10 seconds of plasma treatment, a weak resonant signal appears around 3059cm^{-1}.

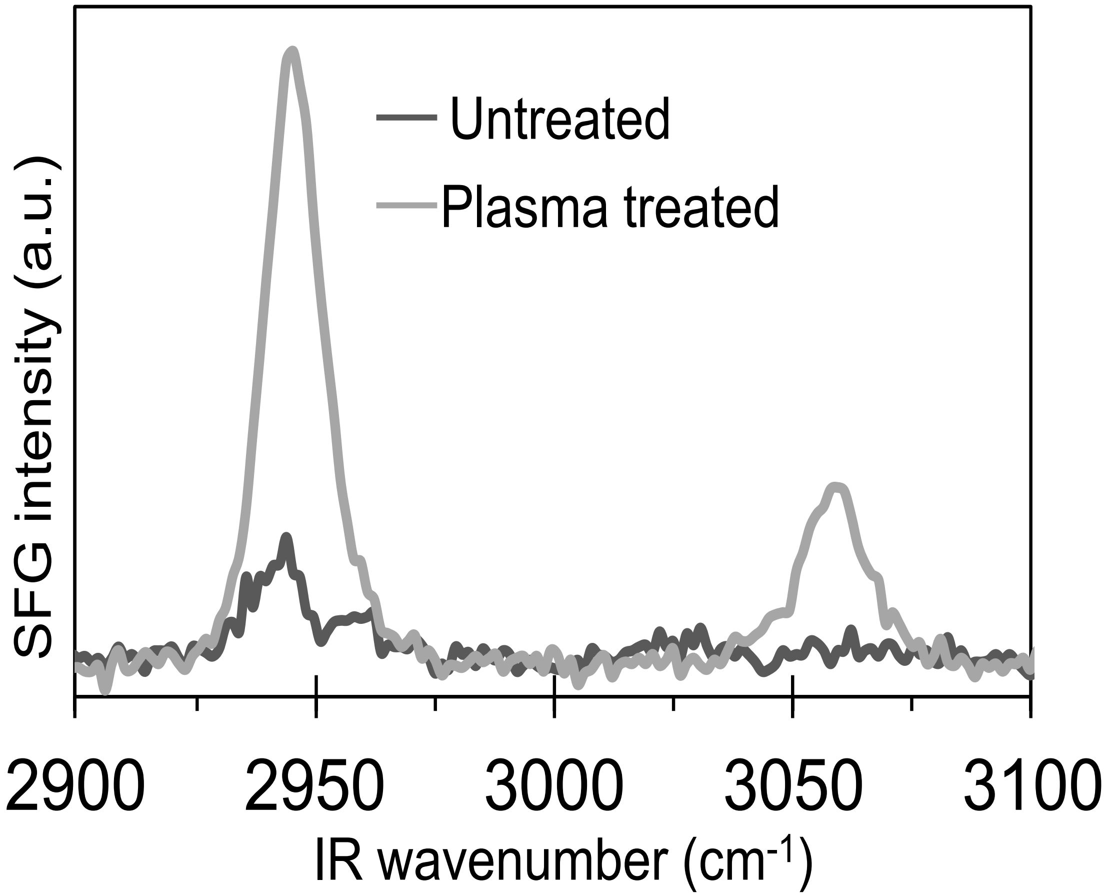

Figure 4.3 VR-SFG spectra of a sample of PS on silicon with an additional thin film of PMMA spin coated on top of it before and after plasma exposure. The 3059 cm^{-1} peak of PS appears after plasma treatment without exposure to the free surface to plasma species. The 2945 cm^{-1} peak of PMMA not only persists, but also increases in intensity. following treatment.

amplitudes of the peaks in *ssp* polarized spectra can be related to the average tilt angle of the phenyl rings from the surface normal using the following equation:[12-14]

$$R = \left|\frac{A_{B1}}{A_{A1}}\right| = \left|\left(\frac{\beta_{caa,B1}}{\beta_{aac,A1}}\right)\left(\frac{2(<\cos 3\theta> - <\cos\theta>)}{(7+2r)<\cos\theta> + (1-2r)<\cos 3\theta>}\right)\right| \tag{4.1}$$

In the above equation, A_{A1} and A_{B1} represent the amplitudes of the peaks corresponding to modes of A_1 and B_1 symmetry, respectively. For phenyl groups, the peak at 3027 cm^{-1} corresponds to the ν_{20b} mode, which has B_1 symmetry, and the 3069 cm^{-1} and 3059 cm^{-1} peaks both correspond to the ν_2 mode, which has A_1 symmetry. $\beta_{aac,A1}$ and $\beta_{caa,B1}$ represent the respective hyperpolarizabilities of the same two modes, and r is the ratio of β_{ccc}/β_{aac} for the ν_2 mode. The r value for the ν_2 mode has been theoretically calculated as 1.13 by Briggman *et al.*[15] θ is the tilt angle relative to the surface normal, illustrated in the inset to Figure 4.4. Orientation information can be extracted by comparing the ratio of the intensities of the 3027 cm^{-1} and 3069 cm^{-1} (or 3059 cm^{-1}) peaks, which are the most dominant features in the spectrum.

The absolute magnitude of the curve described by Equation (4.1) and shown graphically in Figure 4.4 depends on the hyperpolarizability ratios of the vibrational modes. Unfortunately, exact values of the hyperpolarizability are not available, but qualitative changes can still be determined by observing trends in relative peak amplitudes.[16] In this fashion, the orientation of PS phenyl rings on the different substrates after plasma treatment can be compared relative to the orientation of phenyl rings in untreated PS.

For the spectra of plasma-treated PS on silicon, the intensity of the ν_2 peak increases relative to the intensity of the 3027 cm^{-1} peak. This provides a smaller value for R in Equation (4.1), corresponding to a smaller tilt angle from the surface normal than in untreated PS. Because these spectra are dominated by signal from the bulk, this information reveals that

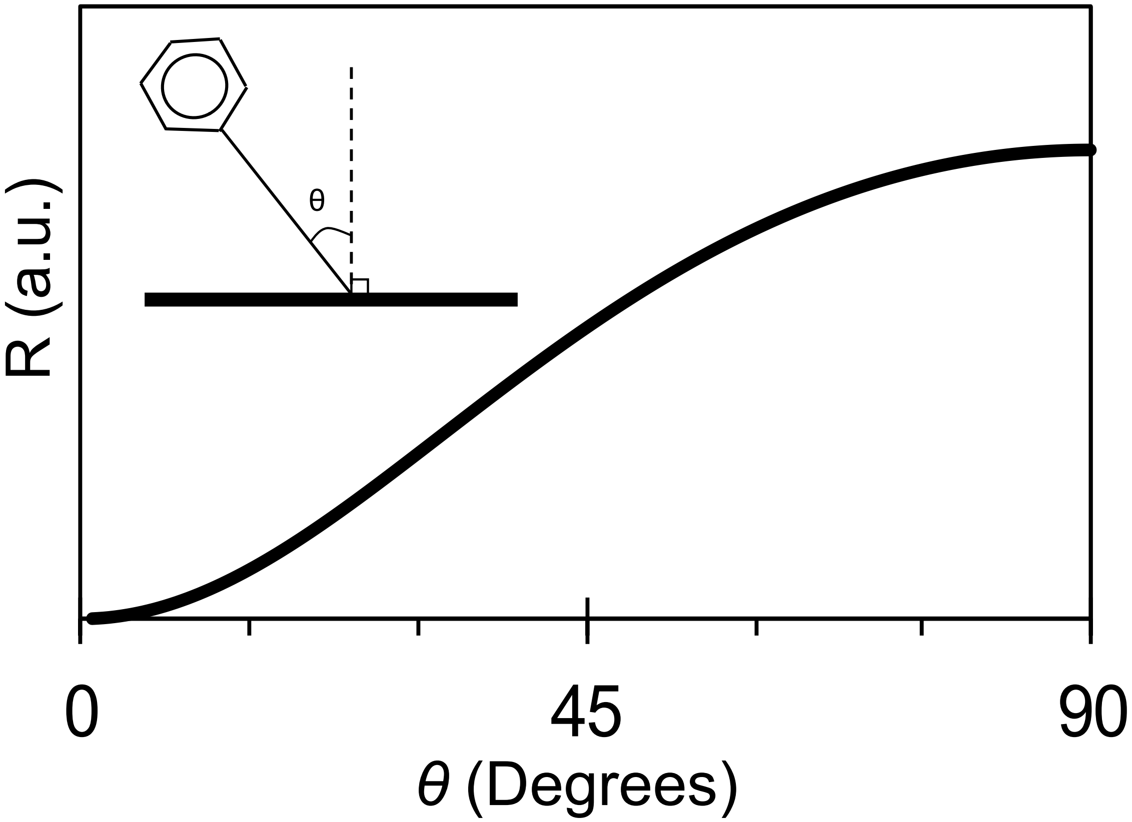

Figure 4.4 Chart of Equation (4.1) used in the determination of tilt angles (θ, in inset figure) from VR-SFG spectra. The plotted curve represents only the angular portion of the equation and assumes no knowledge of hyperpolarizability values. The hyperpolarizability ratio offsets this curve by a constant value, but the general shape is always the same.

the bulk phenyl rings of PS become more upright with plasma treatment. Any discernible information about the surface, however, is lost.

Although signal intensity often increased after plasma treatment for PS on silicon, the coatings on fused silica substrates suffered significant signal loss following plasma treatment. The disappearance of the ν_2 peak at 3069 cm^{-1} is the most apparent spectral difference between untreated and freshly plasma-treated fused silica windows, as shown in Figure 4.5. A weakening or disappearance of this peak has also been observed in previous VR-SFG investigations of plasma-treated PS thin films on fused silica substrates, but with a different interpretation of results than we propose.[4-6] Prior investigators attributed this change to destruction of the phenyl ring by the plasma; however, as seen in our studies, the aromatic peak at 3027 cm^{-1} persists at nearly the same intensity after plasma treatment. The persistence of this peak demonstrates that phenyl rings are still present on the surface with nearly equal concentration but have adopted a different orientation. Interference from the nonresonant SFG signal can often mask this feature;[8] this was likely the case in the earlier studies.

For plasma-treated PS on fused silica, the value of R in Equation (4.1) is very large due to the disappearance of the ν_2 peaks. This change corresponds to a relatively high tilt angle, or phenyl rings that are more parallel to the plane of the surface than before plasma treatment. We do not see the 3059 cm^{-1} peak corresponding to bulk PS in these samples, but this observation alone is not enough to verify that the bulk is not ordered. The bulk may adopt a preferred orientation in fused silica, but if the phenyl rings lie parallel to the surface plane, we would still expect the absence of the 3059 cm^{-1} peak. Although it cannot be distinguished from these spectra alone whether the bulk of PS on fused silica is ordered with a large tilt angle or remains isotropic, the phenyl groups that are observed are nearly lying down. However, further

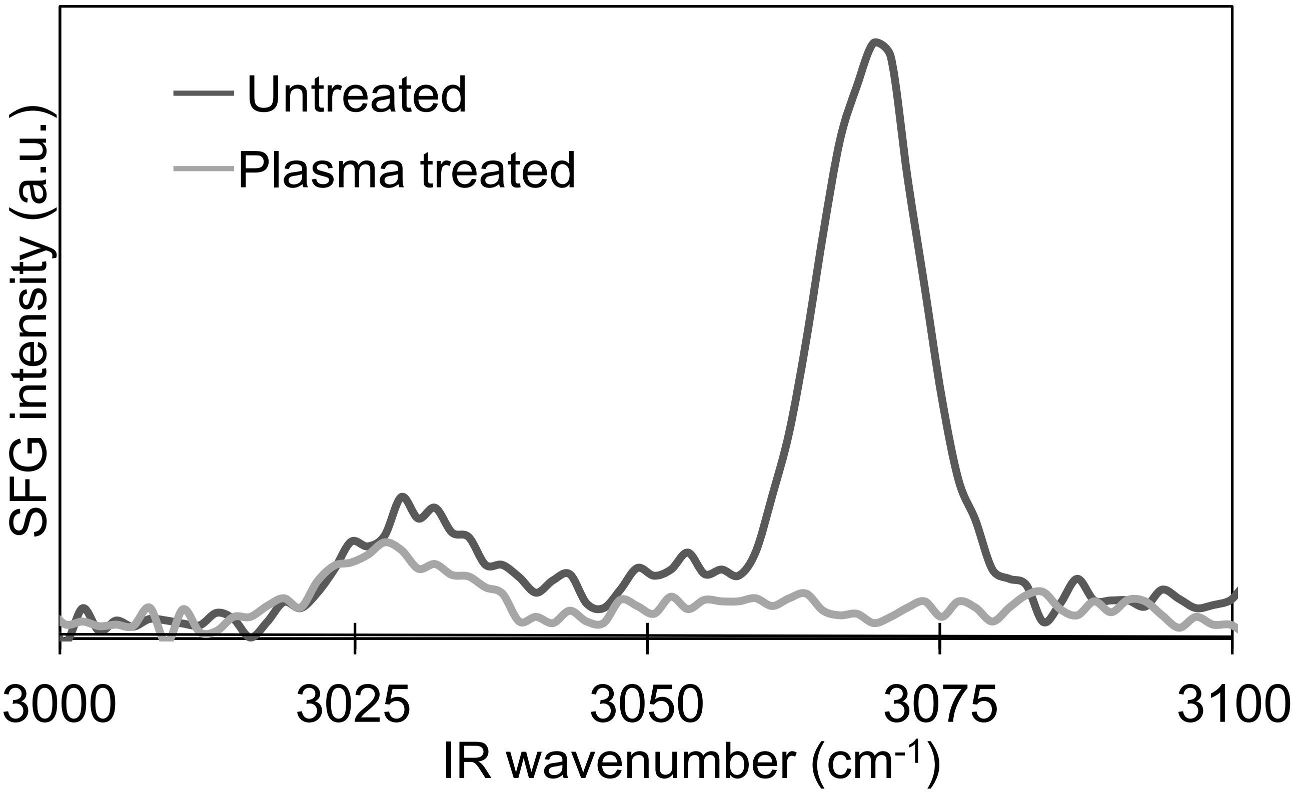

Figure 4.5 VR-SFG spectra of PS on fused silica before and after plasma treatment. Prior to plasma treatment, the resonant signal detected from PS on fused silica substrate is identical to that obtained from PS on polished silicon. Following plasma treatment of PS on a fused silica substrate, the signal from the ν_2 peak is greatly diminished.

experimental constraints applied to study the connection between substrate properties and plasma effects do suggest that plasma modifications of PS films on fused silica substrates are in fact limited to the free surface, as shown below.

4.4.3 Substrate Dependent Response to Plasma Treatment

Three properties of the substrate potentially cause the different response of PS to plasma treatment: crystallinity, transparency to vacuum ultraviolet (VUV) radiation, and/or conductivity. The crystallinity of the substrate was shown to have no effect; PS films on sapphire substrates behaved similarly to those on fused silica substrates whether the sapphire was a *z*-oriented single crystal or amorphous. As mentioned previously, Poncin-Epaillard *et al.* proposed that VUV exposure was responsible for the bulk modifications they observed.[7] However, as more recent studies have shown, exposure times on the order of minutes to are required to affect the structure of PS, whereas plasma exposure requires only seconds to cause a change of similar magnitude.[4]We further confirmed that VUV exposure is not responsible for the results obtained on the different substrates by plasma treating PS films on fused silica with an additional fused silica substrate placed on top of the free surface. This prevents direct exposure of the PS to reactive species in the plasma but allows the VUV radiation generated in the plasma to access both the free surface and buried interface. The VR-SFG spectra of the films plasma-treated in this way were identical to those of untreated PS films.

These results not only confirm that penetration of VUV radiation through the transparent substrates is not a significant factor in the orientation of plasma-treated PS, but also suggest that the effects of plasma treatment for PS on fused silica and similar substrates is actually limited to the free surface. One possibility for the large tilt angle of phenyl rings after plasma exposure on insulating substrates is the selective destruction of phenyl rings of a particular orientation. The tilt angle obtained through the analysis of VR-SFG data is the weighted average in the distribution of tilt angles of probed molecules. Phenyl rings with smaller tilt angles that are standing up further from the plane of the surface would be more susceptible to reaction with plasma species, selectively leaving behind phenyl rings with a large tilt angle. Although we offer this simple explanation as a possibility, we acknowledge that the true explanation may be more complex.

After eliminating crystallinity and substrate transparency to VUV radiation, the only link we have been able to establish between substrate properties and the response to plasma treatment is the conductivity of the substrate. As shown in Figure 4.6, the effects observed for PS on silicon substrates also occur on other conductive substrates, such as steel (it should be noted that these spectra contain some nonresonant interference). When other insulating substrates, such as sapphire, are used, the effects are similar to those observed on fused silica.

Results from previous studies investigating the effects of electric fields on diblock copolymers support the reasoning that the behavior of the different materials is due to conductivity. Thurn-Albrecht *et al.* showed that when an electric field of sufficient strength is applied to a diblock copolymer of PMMA and PS at elevated temperature, the cylindrical domains reorient parallel to the applied electric field.[17] For that study, the copolymer was rolled between aluminized Kapton sheets, which acted as electrodes; on one side the aluminum directly contacted the copolymer, and on the other side the Kapton contacted the copolymer. Similarly, in the present study, one side of the PS directly contacted a conducting substrate, and the other side was either directly exposed to plasma or separated from the plasma by a thin film of PMMA. Although the results observed in the previous study required elevated temperatures to overcome

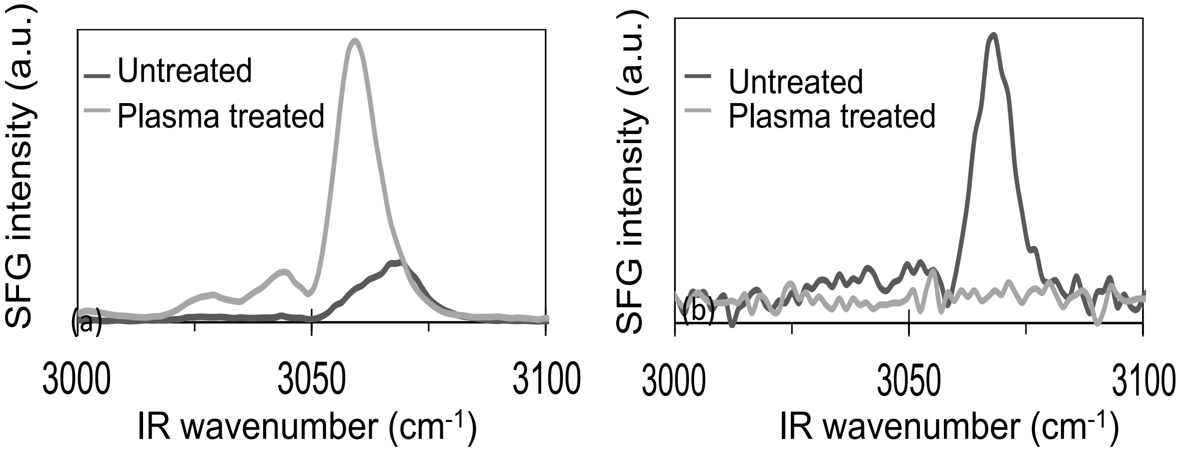

Figure 4.6 VR-SFG spectra of PS on a) stainless steel and b) sapphire. PS on stainless steel substrates showed an increased VR-SFG response and change in the dominant ν_2 peak following plasma treatment, similar to films on silicon substrates. PS films on sapphire substrates behaved similarly to those on fused silica substrates.

intermolecular interactions, the environment inside the plasma chamber likely provides the energy necessary to reorient polymer chains at much lower temperatures.

4.4.4 The Effects of Annealing on Plasma-Treated Polymer

Previous studies have shown that after a plasma-treated surface is annealed, it recovers some of the properties of the untreated polymer.[1,2,6,18-24] During the annealing process, the polymer is heated above the glass transition temperature, and polymer chains are able to move past each other more freely and into a thermodynamically-preferred orientation, if one exists. If no orientation is favored, they assume a random orientation. The extent and nature of the corresponding structural recovery was investigated by comparison of the VR-SFG spectra of plasma-treated PS after annealing to those of untreated samples.

Annealing of untreated PS changes the overall intensity of the VR-SFG signal, but does not change the relative peak intensities in the resonant spectrum.[8] This consistency in the VR-SFG signal indicates that the average orientation of the phenyl groups remains unchanged. A comparison of annealed and unannealed films before plasma treatment confirmed these results. Because annealing has no effect on the orientation of phenyl rings in untreated PS films, any differences observed between plasma-treated films and untreated films after annealing must be due to residual effects of the plasma treatment, not the annealing process itself.

Although annealing does not affect the orientation of phenyl groups of untreated PS, the annealing process has a significant effect on plasma-treated PS. Figure 4.7 compares spectra of plasma-treated and untreated PS on silicon substrates after annealing. The 3059 cm^{-1} peak that dominates immediately after plasma treatment diminishes with annealing, and the 3069 cm^{-1} peak becomes prominent again, similar to an untreated film; however, the relative intensities of the 3069 cm^{-1} and 3027 cm^{-1} peaks do not return to the same ratio as untreated PS. The change

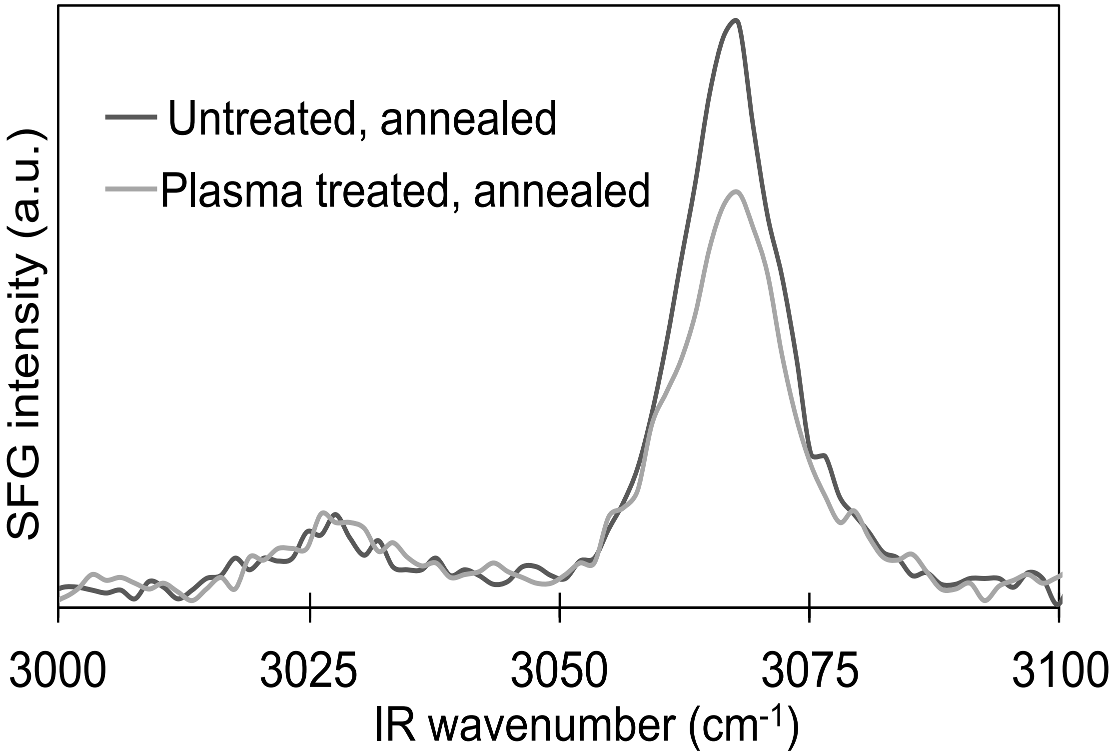

Figure 4.7 VR-SFG spectra of treated and untreated PS on silicon following annealing for 24 hours at 120˚C. The 3069 cm^{-1} peak is restored after annealing, but the ratio between the 3069 cm^{-1} and 3027 cm^{-1} peaks for plasma-treated samples differs from that of the untreated samples.

of the dominant ν_2 peak from 3059 cm^{-1} back to 3069 cm^{-1} suggests that the phenyl rings in the bulk have again adopted a random orientation and that only surface phenyl groups are detected.[11]

Because the substrate is more electron-dense than the polymer, and can therefore minimize interfacial energy independent of PS orientation, the polymer can recover the same orientation in the bulk and at the buried interface as untreated samples.[25] Once the bulk returns to the original isotropic orientation, VR-SFG is no longer sensitive to bulk contributions, and the detected signal must originate from the free surface. The lack of recovery in relative intensities, however, indicates that although the density of detected phenyl rings returns to that of untreated polymer, the orientation of those phenyl rings is not fully restored upon annealing.

Plasma-treated films on fused silica (and all other substrates studied) recovered in a manner similar to those on polished silicon. As shown in Figure 4.8, after annealing, the 3069 cm^{-1} peak reappeared with signal comparable to that collected from untreated annealed samples on fused silica, but the signal-to-noise ratio was insufficient to discern additional peaks. The recovery of intensity by the ν_2 peak after annealing further supports the idea that many surface phenyl groups remain after plasma treatment; if a significant fraction of surface phenyl groups had been chemically altered or destroyed, surface recovery would not be possible.

Although plasma treatment primarily results in the reorientation of phenyl rings, additional chemical functionalities do influence surface reordering. A study by Zhang *et al.*[4] reported a peak in the C=O region of the VR-SFG spectrum after plasma treatment that is not initially present, and x-ray photoelectron spectroscopy (XPS) also confirmed the addition of oxygenated moieties to the surface. Although we emphasize the modification of PS bulk with plasma treatment, we agree with this claim of some chemical modification to the surface. In fact, the failure of the phenyl rings to completely recover the orientation of the untreated polymer following annealing supports this idea. If the only modification to the surface with plasma treatment were the removal or reorientation of phenyl rings on the free surface, we would expect to see the recovery of that original surface with annealing. We see, however, a greater tilt angle of surface phenyl groups on annealed plasma-treated films than on annealed untreated films. Because the structure of the polymer has been chemically altered at the surface, the preferred orientation at equilibrium also changes, which causes the phenyl rings to tilt closer to the surface than they do in untreated films.

We do not yet have a complete sense of the long-term behavior of plasma-treated PS films on conducting substrates. We previously showed that freshly spin-coated PS films resemble annealed films after about 1 week at ambient conditions.[8] When plasma-treated samples were stored at ambient conditions, we still observed the increased intensity of the 3059 cm^{-1} peak for at least six weeks. This result indicates that significant alignment of the bulk phenyl rings persists for some time and does not relax without heating. The recovery of the surface seems to depend on whether the samples were stored in an inert environment; the more hydrophilic surface is probably quickly contaminated, which will affect the ability of the remaining phenyl rings at the surface to reorient. These aspects of material aging are still under investigation.

4.5 Conclusions

Plasma treatment is generally thought to only affect the surface of a material, but our work has shown that plasma treatment can induce anisotropy in polystyrene thin films. The ordering of the bulk during plasma treatment can be selectively controlled by choice of substrate. On conducting substrates, previously isotropic phenyl rings in the bulk of the polymer organize and adopt a more upright orientation. Plasma treatment of PS on insulating substrates, however, does not result in significant change to the bulk structure but results in surface phenyl rings that are mostly lying down. In addition to altering the orientation of phenyl rings on the surface and, for some cases, in the bulk, the plasma treatment also results in a chemically altered surface. This chemical change has been reported previously and is evident in the addition of a small CO signal to the VR-SFG spectra[4] and the inability of plasma-treated PS to recover an untreated orientation after annealing. Although the density of phenyl rings on the annealed surface approaches that of the untreated surface, the tilt angle of the rings is typically greater than what is observed on the untreated PS surface. Work to investigate the effects of plasma treatment on other polymers is ongoing.

Our results have shown that the effect of plasma treatment of polymers is not always limited to the free surface; therefore plasma treatment is not necessarily a surface-specific treatment. The knowledge that it is possible to modify more than just a free surface with exposure to plasma provides new possibilities regarding the practical aspects of plasma treatment of polymers. The effect of plasma treatment on the bulk of the material must now be considered in applications where it is desirable to selectively modify the surface. Conversely, if an application requires an ordering of the bulk only, plasma treatment with surface protection may be a possible route to accomplish this goal.

ACKNOWLEDGMENT We thank Shawn Kunzler, Kevin Ames, and Kimberly Heiner for their assistance in preparing samples. We thank Matthew R. Linford and Steven R. Goates for helpful discussion of this work and additionally thank Matthew R. Linford for the use of his plasma cleaner and ellipsometer. This work was supported by the Air Force Office of Scientific Research Young Investigator Research Program (AFOSR-YIP), Award FA9550-09-1-0142.

4.6 References

(1) Liston, E. M.; Martinu, L.; Wertheimer, M. R. In *Plasma Surface modification of Polymers: Relevance to Adhesion*; Strobel, M., Lyons, C., Mittal, K. L., Eds.; VSP BV: Netherlands, 1994; 3–39.

(2) Fritz, J. L.; Owen, M. J. *J. Adhes.* **1995**, *54*, 33–45.

(3) Zhu, X. D.; Suhr, H.; Shen, Y. R. *Phys. Rev. B* **1987**, *35*, 3047–3050.

(4) Zhang, D.; Dougal, S. M.; Yeganeh, M. S. *Langmuir* **2000**, *16*, 4528–4532.

(5) Zhang, C.; Wang, J.; Khmaladze, A.; Liu, Y.; Ding, B.; Jasensky, J.; Chen, Z. *Opt. Lett.* **2011**, *36*, 2272–2274.

(6) Li, J.; Oh, K.; Yu, H. *Chin. J. Polym. Sci.* **2005**, *23*, 187–196.

(7) Poncin-Epaillard, F.; Brosse, J. C.; Falher, T. *Macromolecules* **1997**, *30*, 4415–4420.

(8) Curtis, A. D.; Reynolds, S. B.; Calchera, A. R.; Patterson, J. E. *J. Phys. Chem. Lett.* **2010**, *1*, 2435–2439.

(9) Lagutchev, A.; Hambir, S. A.; Dlott, D. D. *J. Phys. Chem. Lett. C* **2007**, *111*, 1345–13647.

(10) Varsányi, G.; Szöke, S. *Vibrational spectra of benzene derivatives*; Academic Press, 1969.

(11) Curtis, A. D.; Calchera, A. C.; Patterson, J. E. *Vib. Spectrosc.* **2013**, *68*, 71–81.

(12) Gautam, K. S.; Schwab, A. D.; Dhino, W. A.; Zhang, D.; Dougal, S. M.; Yeganeh, M. S. *Phys. Rev. Lett.* **2000**, *85*, 3854–3857.

(13) Hirose, C.; Akamatsu, N.; Domen, K. *Appl. Spectrosc.* **1992**, *46*, 1051–1072.

(14) Duffy, D. C.; Davies, P. B.; Bain, C. D. *J. Phys. Chem.* **1995**, *99*, 15241–15246.

(15) Briggman, K. A.; Stephenson, J. C.; Wallace, W. E.; Richter, L. J. *J. Phys. Chem. B* **2001**, *105*, 2785–2791.

(16) Curtis, A. D.; Burt, S. R.; Calchera, A. R.; Patterson, J. E. *J. Phys. Chem. C* **2011**, *115*, 11550–11559.

(17) Thurn-Albrecht, T.; DeRouchey, J.; Russell, T. P.; Jaeger, H. M. *Macromolecules* **2000**, *33*, 3250–3253.

(18) Garbassi, F.; Morra, M.; Occhiello, E. *Polymer Surfaces: From Physics to Technology*; Wiley: New York, 1998.

(19) Fridman, A. *Plasma Chemistry*; Cambridge University Press: New York, 2008.

(20) Murakami, T.; Kuroda, S.; Osawa, Z. *J. Colloid Interface Sci.* **1998**, *202*, 37–44.

(21) Morra, M.; Occhiello, E.; Garbassi, F. *J. Colloid Interface Sci.* **1989**, *132*, 504–508.

(22) Occhiello, E.; Morra, M.; Morini, G.; Garbassi, F.; Humphrey, P. *J. Appl. Polym. Sci.* **1991**, *42*, 551–559.

(23) Occhiello, E.; Morra, M.; Garbassi, F.; Johnson, D.; Humphrey, P. *Appl. Surf. Sci.* **1991**, *47*, 235–242.

(24) Pennings, J. F. M.; Bosman, B. *Colloid Polym. Sci.* **1979**, *257*, 720–724.

(25) Dowben, P.A.; Xu, B.; Choi, J.; Monkawa, E. In *CHARACTERIZATION AND SPECTROSCOPY OF THIN FILMS*; Nalwa, H. S., Ed.; Academic Press: San Diego, 2002; Vol. 2; 98

Chapter 5: Coupling Adhesion Measurements with VSFG Spectroscopy

5.1 Introduction

The ability to control and adjust the adhesive properties of an adhesive or coating is highly sought-after in many fields, including medical, engineering, and manufacturing. Despite the broad importance of adhesion phenomena, the development of new adhesives is performed principally by trial and error. The reason adhesive engineers must resort to empirically-based methods in developing new adhesives is that the molecular-level processes governing adhesion are still largely ambiguous.

The study of the relationship between structure and adhesive properties, by the very nature of the adhesive process, poses significant challenges. The location of the adhesive interaction between two substrates prohibits most spectroscopic investigation of the phenomenon. Because relatively few molecules are located at the interface where adhesion takes place, bulk spectroscopies such as FTIR or Raman are unable to discern the molecules participating in the adhesion process, which may behave differently than the molecules located in the bulk of the sample. Most surface-specific spectroscopic techniques, such as x-ray photoelectron spectroscopy (XPS) and attenuated total reflectance FTIR (ATR-FTIR) also fail to capture molecular information about functional adhesives because the probing depth of the technique prohibits gaining any information at all from buried interfaces. The only recourse when studying adhesives using bulk or surface-specific spectroscopies has been to break the adhesive bond, at which point information regarding the orientation of molecules participating in adhesion and how that orientation changes during failure has been lost.

Vibrational sum-frequency generation spectroscopy (VSFG) allows the spectroscopic study of adhesives without breaking the adhesive bond. The symmetry requirements to produce VSFG signal allow it to avoid the pitfalls of both surface-specific and bulk techniques. As discussed in Chapter 1, signal in VSFG and other techniques derived from second-order nonlinear optics is produced only in regions of a sample lacking inversion symmetry because of the symmetry requirements of $\chi_{ijk}^{(2)}$. If the bulk materials are isotropic, this requirement gives the techniques the ability to selectively probe surfaces and interfaces.

This ability to study molecules specifically at an interface enables the study of interfacial phenomena without breaking the interface. The molecules participating in the adhesion interaction in a functional adhesive can be studied spectroscopically using VSFG. Such study could determine the relationship between molecular orientation and the functionality of the adhesive at any stage of the adhesive process, whether static or under an applied stress. With continued study using such techniques, adhesive engineers could eventually use a more directed approach to developing new adhesives with specific desired properties.

As discussed in Chapter 1, Wilson *et al.*[1] have previously used VSFG to study adhesion between polystyrene thin films and spin-on glass with both hydrophobic and hydrophilic treatments. They used a peel test to compare the strength of adhesion between the polystyrene and spin-on glass with the two treatments. They found that when the spin-on glass was treated to make it hydrophilic, the polystyrene films passed the peel test, whereas the films adhering to the natively hydrophobic spin-on glass failed the peel test. They determined different orientations of polystyrene at the hydrophobic and hydrophilic interface, and proposed that the improved interaction between the phenyl rings of polystyrene spin-on glass enabled by the orientation at the hydrophilic interface caused the improvement in adhesion on that substrate.

In our VSFG adhesion studies, we hope to use improvements in VSFG analysis and knowledge of nonresonant signal, including the selective suppression of nonresonant contributions[2] to determine a relationship between polymer orientation and adhesive strength in a functional adhesive. With the variable time delay technique, which provides multiple spectra with the same underlying peak parameters, we are now able to uniquely fit VSFG spectra without nonresonant signal interference and obtain reliable peak parameters for the resonant spectra.[3] With reliable peak parameters, we may use the analysis technique put forth by Briggmann *et al.*[4] to accurately determine the relative orientation of molecules under different circumstances.

In addition to using improved VSFG analysis techniques, we have made progress toward the successful coupling of VSFG experiments with dynamic strength testing of an adhesive bond. The NIST study used only a peel test to study adhesive failure. The peel test only provides qualitative data on adhesive failure, and does not allow the determination of molecular behavior as the bond fails. By testing adhesives with a tensile tester while simultaneously collecting VSFG spectra, we can learn about how the molecular orientation at the adhesive bond changes under measured quantities of stress leading up to failure. In this chapter, I outline the efforts made toward successfully testing adhesive strength of PMMA and polystyrene simultaneously with VSFG data collection, along with the degree to which those efforts have been successful.

5.2 General Methods and Equipment

Polystyrene (M_w=230,000) was obtained from Aldrich, toluene was UltimAR® from Mallinckrodt Chemicals, poly(methyl methacrylate) (PMMA) (M_w=120,000) was obtained from Aldrich, and nitromethane was spectrograde from Fisher Scientific. The adhesives used to attach the posts was either rubber cement (All-purpose Cement from Henkel Corporation) or cyanoacrylate superglue (Super Glue Liquid from Henkel Corporation).

Spin-coating was performed using a Model WS650SZ-6NPP/A1/AR1 spin coater from Laurell Technologies. Spin-coating of solvent was done at a low speed so that the solvent was distributed over the surface in a thin layer, and was still wet after the program was finished. The program used for spin-coating solvents is included in the Appendix chapter, along with the programs used to obtain different thicknesses of polymer films. Solvent-cast polymer films were made by placing a solution of dissolved polymer on the substrate and allowing the solvent to completely evaporate.

Strength testing was performed using an Instron 3345 tensile tester fitted with an Instron Model 2519-104 force transducer with a load capacity of 500 N. Prompted test methods for running the tensile-testing protocols described were composed using the built-in tools included in the Blue Hill 2 Material Testing Software (version 2.9), a software package designed to be used with Instron tensile testers. Detailed instructions on how to set up and edit methods using this program are included in the Appendix.

5.3 Coupling strength tester with laser system

**Dr. Qingsong Wang designed the pulley system, sample mount, posts, and sample holders described in this section, with some contributions from Alex Curtis.*

Several challenges must be overcome in order to couple the strength tester to the VSFG system. First, the sample must be mounted in such a way that simultaneously allows light to enter and exit, yet stabilizes it enough for strength testing. Secondly, tensile testers are designed to pull samples apart vertically, not horizontally as we require given the optical setup.

Furthermore, we must ensure that the sample mount couples to the tensile tester in a way that neither the tensile tester nor the sample moves.

We coupled the tensile tester to the laser system through a pulley system that translates the vertical motion of the tensile tester into horizontally-applied stress on the adhesive sample. A picture of the implementation of this system is shown in Figure 5.1. We fixed a hook attachment to the top arm of the tester, and replaced the bottom mount with a pulley assembly. A steel cable with a loop on one end and a ball on the other end is used to connect the tester with the sample. The loop in the cable fits over the hook on the top arm of the tensile tester, and the ball fits into a channel on the end of the posts adhered to the sample. The cable is fed through the pulley assembly, and then attached to the post on the sample. Once the sample is secured in the sample mount assembly, the test is ready to begin.

To prevent movement of the tensile tester or sample mount, we attach the sample mount to the tensile tester via two rigid arms made of stainless steel that bolt to both the pulley assembly of the tensile tester and the sample mount bolted to the table. The braces ensures that the stress applied to the sample is completely uncoupled with the relative positions of the tensile tester and the sample.

To solve the problem of allowing light in and out of the sample without compromising the ability to perform simultaneous strength testing, we designed a custom sample holder and posts for applying stress to the adhesive bond. As shown in Figure 5.2, the sample holder is essentially a stainless steel tube, threaded on the inside. At the closed end of the tube, a hole is drilled through the center. This hole leads to a tube whose inside diameter is the same as the outer diameter of the post, and whose outer surface is threaded. The hole and tube allow the insertion of a post with which the sample is stressed via the tensile tester, while the threading on

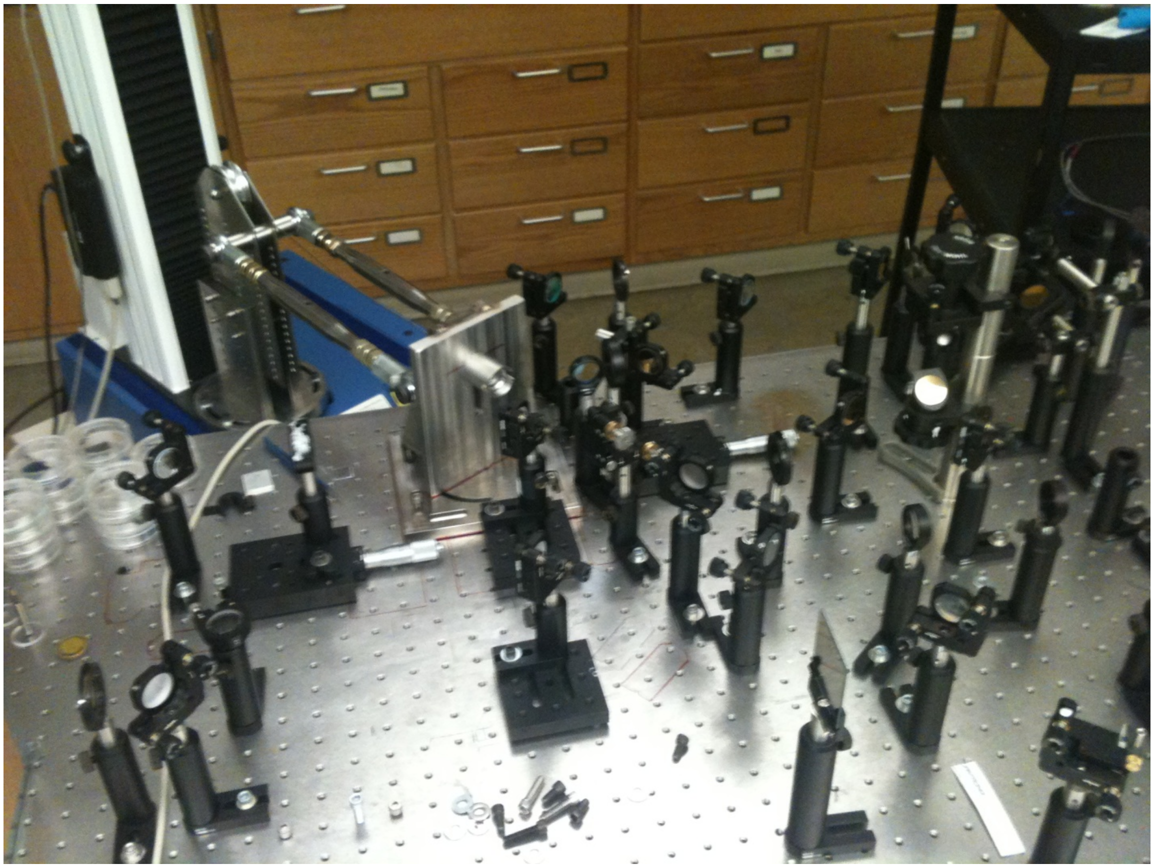

Figure 5.1 Instron 3345 coupled to the VSFG system.

Figure 5.2 Adhesion sample holder. This holder adequately supports the sample for collecting stress data while allowing light to enter and exit the sample for the spectroscopic data collection. Inset: the post used to stress the adhesive samples can be inserted all the way through the hole in the back, and has a special channel to attach the cable that connects it with the tensile tester.

the outside of the tube allows the whole assembly to be tightly mounted onto the permanent sample mount on the optics table. A circular ring with four notches at 0°, 90°, 180°, and 270° and threading around the edges is used to hold the sample into the sample holder. The notches are designed to assist in tightening the ring flush with the front surface of the sample.

The inset image shows a post designed to be used with this sample holder. It attaches to the cable that connects the sample with the tensile tester through the channel that is large enough to accommodate the ball at the end of the cable, and then narrows toward the back end of the post so that the ball is held in as the cable applies a load to the sample. This channel allows the post to be inserted all the way through the hole in the back of the sample holder, which facilitates accommodating the sample in the holder when coupled to the tensile tester.

The dimensions of the sample holder are precise enough to the dimensions of the adhesion samples that the sample cannot move very much in the sample holder. During testing, this immobility is advantageous, but it does present some challenges when initially placing the sample in the holder. The post must be attached to the sample in nearly the exact center so that it can match with the hole in the back of the sample holder. This is done by using a spare sample holder that is not attached to the sample mount as a guide. A post is passed through the tube and hole in the back of the sample holder, adhesive is applied to the end of the post, and then the post is attached to the sample by placing the sample holder over the sample and lowering the post until it makes contact with the coating. The sample holder is left over the sample until the adhesive sets.

To place the sample in the holder, first the cable from the tensile tester is passed through the back of the sample holder, and attached to the post by sliding the ball through the post channel. The sample is then pushed back through the cylinder until the coating side of the sample is flush with the back of the sample holder. The front ring is then screwed down to fit snugly over the non-coated side of the sample, and the sample is ready for simultaneous spectroscopic study and strength testing.

5.4 Challenges with creating samples

Including collecting a background scan, each VSFG spectra takes between five and ten minutes to collect; therefore, one of the first challenges to overcome in performing a dynamic VSFG study of adhesives under stress is making a sample configuration that can withstand stress long enough to collect several spectra. The first types of samples we tried were silicon or fused silica coated with either a spin-coated (~100 nm) layer of polystyrene or a solvent-cast (~1 mm) layer of polystyrene. In each sample, a post is attached to the polymer with an adhesive, either cyanoacrylate or rubber cement, and stressed using a tensile tester. As observed by Wilson *et al.* in their adhesion study with polystyrene, the thin films of polystyrene on a hydrophilic surface such as clean SiO_2 is very strong. The bond between the adhesive and the post failed before the bond between polystyrene and the substrate in these samples. On the contrary, the thicker films of polystyrene tended to peel off of the substrate extremely easily, and were too fragile to even place into the tensile tester sample holder without breaking the bond.

Polystyrene and poly(methyl methacrylate) (PMMA) are not miscible. Because the two polymers are known to have poor compatibility, we tried various combinations of polystyrene and PMMA films on the same substrates and with the same adhesives to attach the posts. Figure 5.3 illustrates several sample configurations that have been attempted.

Figure 5.3 (a) shows a sample where 100 nm of polystyrene in is spin-coated from toluene solution onto a fused silica window, 10% PMMA in nitromethane is solvent-cast onto another fused silica window, and the two sides are solvent-welded together by spin-coating a thin

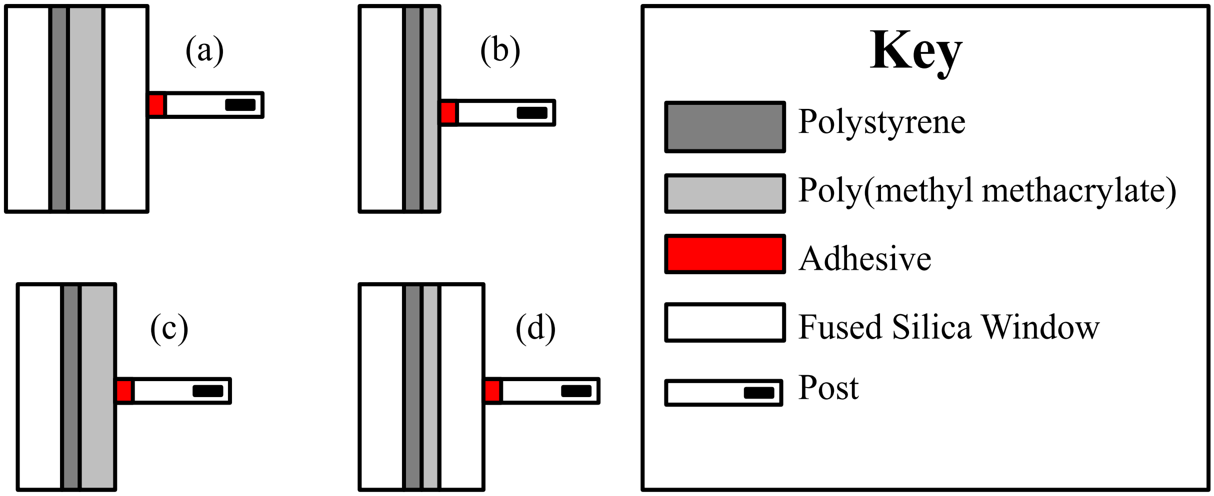

Figure 5.3 Examples of sample types that have been attempted in adhesive testing so far. (a)100 nm polystyrene and 1 mm PMMA between fused silica windows. (b) 100 nm polystyrene layered with 100 nm PMMA on one fused silica window. (c) 100 nm polystyrene layered with 1 mm PMMA on a fused silica window. (d) 100 nm polystyrene and 100 nm PMMA between two fused silica windows.

layer of toluene onto the PMMA side and placing the polystyrene-coated window on top of the PMMA-coated window. The post is then attached using adhesive to the back of the fused silica window coated with PMMA. This type of sample is extremely weak, and none of them even survived the process of attaching the post to the back window.

Figure 5.3 (b) shows a sample created by spin-coating 100 nm of polystyrene from toluene solution on a fused silica window. PMMA was spin-coated from nitromethane solution on top of the polystyrene coating to make a 100 nm layer. The post was then attached directly to the PMMA layer. This sample type was able to withstand up to 100 N of force from the tensile tester, but the failure was between the post and the adhesive rather than between the polystyrene and PMMA layers.

Figure 5.3 (c) shows a type of sample that was made by spin-coating 100 nm of polystyrene from toluene solution onto a fused silica window, then solvent-casting PMMA from nitromethane solution (10% PMMA by weight) on top of the thin polystyrene film. The post was then attached directly to the PMMA layer. With this type of sample, the coating began to peel away from the substrate even before tensile testing was attempted.

The sample illustrated in Figure 5.3 (d) was made by spin-coating ~100 nm of polystyrene from toluene solution onto one fused silica window, spin-coating ~150 nm of PMMA from nitromethane solution onto the other window, and attaching the two by spin-coating a thin layer of toluene onto the PMMA side, placing the polystyrene-coated side coating-down onto the PMMA side, and allowing the solvent to completely evaporate. As with the other solvent-welded samples, these samples were extremely fragile, and did not survive to be placed into the tensile testing apparatus.

The type of samples with thin layers of polystyrene and PMMA attached to the post with rubber cement were the only ones that survived enough force to make it viable for adhesion testing. However, the adhesion between the PMMA and polystyrene (and polystyrene to the glass) was too strong compared to the adhesion between the rubber cement and the post. So far, we have been unsuccessful in our attempts to make the adhesion between the polymers and the glass comparable to the adhesion between the rubber cement and the post. We have tried solvent-casting a thin layer of PMMA, polystyrene, or polyethylene glycol terephthalate (PET) directly onto the fused silica window. These coatings were made so that the surface area of the polymer coverage was approximately equal to the surface area of contact with the post, but this made the adhesive strength too weak in every case, and the post broke off under its own weight before coupling with the tensile tester.

Another problem that occurs is that cyanoacrylate tends to dissolve the polymers. This dissolution is especially a problem with the thin films. Rubber cement does not dissolve the polymers, but does not adhere as strongly to the polymers, and also has a proprietary composition, and so is not favorable to use in spectroscopic studies where vibrational modes from the adhesive could appear and interfere with modes from the coating being tested. Currently, we use mainly rubber cement as an adhesive for the post because the problems associated with using it are preferable to the dissolution of the polymer, which causes the adhesive bond being tested to change: rather than simply testing a polymer coating, after dissolving the polymer, the experiment tests a coating of polymer mixed with cyanoacrylate.

5.5 Efforts with tensile tester programs

One way to resolve the issues with weak adhesive forces in the samples is to program the tensile tester to apply loads in different ways. Additionally, the tensile tester must be controllable remotely in order to keep the room dark for spectroscopic measurements. A prompted test was custom-designed and optimized to stress samples while collecting spectroscopic data. Details about this program and instructions on how to create custom programs using Blue Hill 2 software are included in the Appendix. To allow time to collect spectra at each amount of force applied to the sample, the program must stop and hold that quantity of force until the spectrum can be collected, so a mechanism for holding a certain quantity of force must be included in the program.

The test method was designed in the Blue Hill 2 software that was provided by the manufacturer to work with the tensile tester. The different steps of the test were controlled using the test profiler built into the program. The test profiler test was built using a three-step model. The first step is a ramp up to a set force. The second step is a holding step. In the first runs with the tests, the tester held displacement, but under these methods, the adhesive relaxed over time and the force changed even at the same displacement. The second step now holds the force, which sometimes requires that an adjustment be made to the extension but ensures that the comparisons in spectra and molecular orientation correlate to how much stress is put on the adhesive bond. This second step is on a timer to end after a certain amount of time, or when the user ends the hold manually, whichever occurs first. The third step is a relative ramp which increases the load by a set amount. The test then loops back to the holding step, and the cycle repeats until the user chooses to end the test.

One of the first problems to overcome was that the tensile tester tended to overshoot the ending force input, especially for the first step. Figure 5.4 (a) shows the load/time curve of an experiment testing a thin polystyrene film with cyanoacrylate as the adhesive to attach the post. As seen in this figure, overshooting past the desired load causes the sample to immediately break

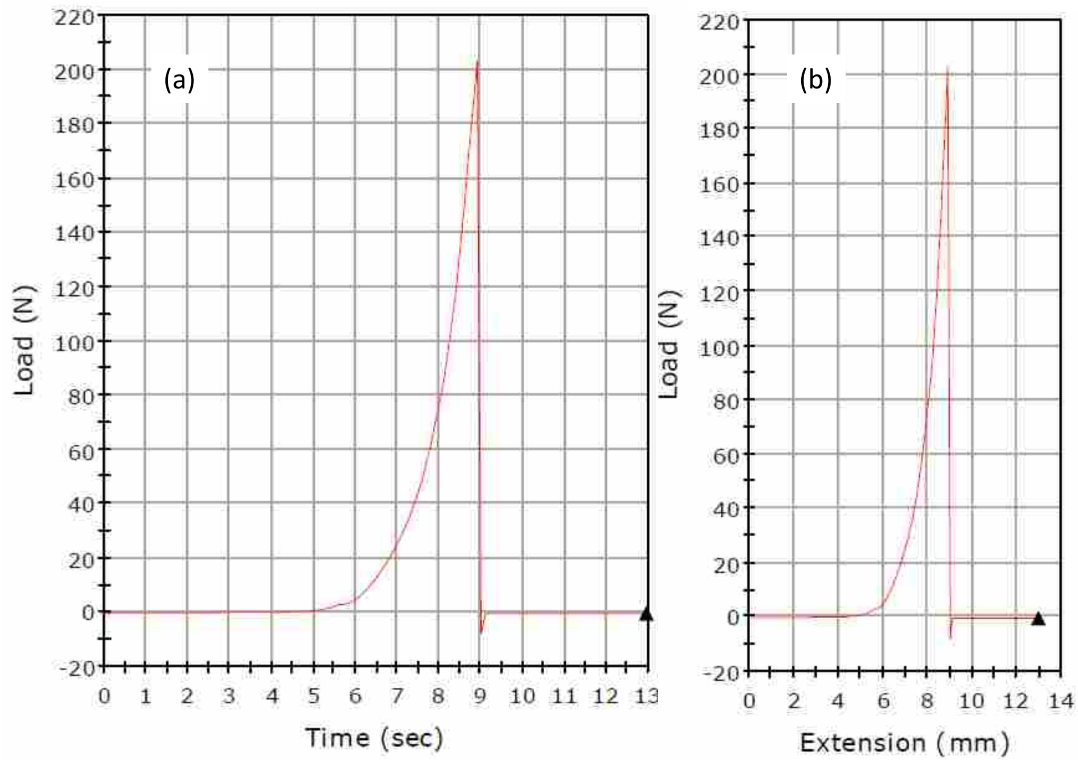

Figure 5.4 A test profiler method test of a polystyrene thin film on fused silica, using cyanoacrylate adhesive to attach the post. (a) shows how the load changed over the course of the test. The test ended within nine seconds due to the program overshooting the set load for the first step. (b) shows the results of the same test with load plotted against extension. This shows that although spectra could not be collected during this test, the tensile data is consistent with a successful test.

before the load can be sustained and a spectrum collected. Figure 5.4 (b) shows the load/extension curve for this same experiment. The shape of the curve is what would be expected for a stiff adhesive bond with a sharp transition from the elastic region to the break, so although spectra cannot be collected during the test, the tensile test itself still appears valid.

After some trial and error, it was determined that the amount that the instrument overshot the end force for the initial step was roughly proportional to the speed of the extension and the amount of force applied. In every case, the amount of force applied needed to be quite small, so the main change that could be made was to adjust the speed of the extension. When the extension is applied slowly, the problem with overshooting is minimized, but not eliminated. The detailed program for stressing an adhesive simultaneous with spectroscopic study is included in the Appendix.

Figure 5.5 shows an example of a successful timed test, which was performed on a sample using fused silica as the substrate and two thin film layers of polystyrene and PMMA like the sample illustrated by Figure 5.3 (b), with rubber cement as the adhesive to attach the post. The tensile tester overshoots the set load of 1 N for the first step, but does not apply enough load to break the sample. The test then continues with the program automatically applying a greater load and holding for set periods of time before ramping up to the next load. This process of ramping and holding is able to occur approximately thirty times before adhesive failure.

Figure 5.6 shows the load-extension data for the same test as Figure 5.5. Similar to what is shown in Figure 5.4 (b), the load rises with respect to extension, and then drops sharply at the breaking point. At low loads, the curve retraces itself several times because the extension had to be adjusted in order to maintain constant load over periods of time, and this data did not exactly follow the same curve each time; however, the similarities between this data and the data shown

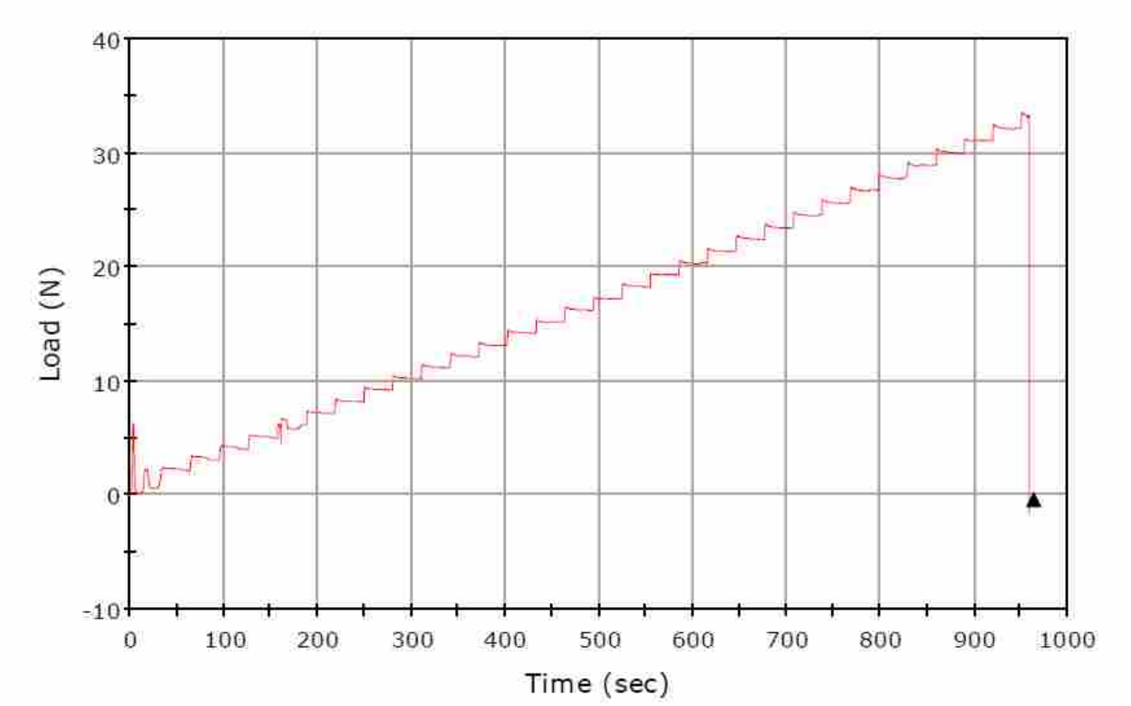

Figure 5.5 Strength testing data from a sample composed of thin layers of polystyrene and PMMA on fused silica, attached to the tensile tester post with rubber cement. The test overshoots the first pre-determined load only minimally, and is able to incrementally ramp and hold the load many times before break.

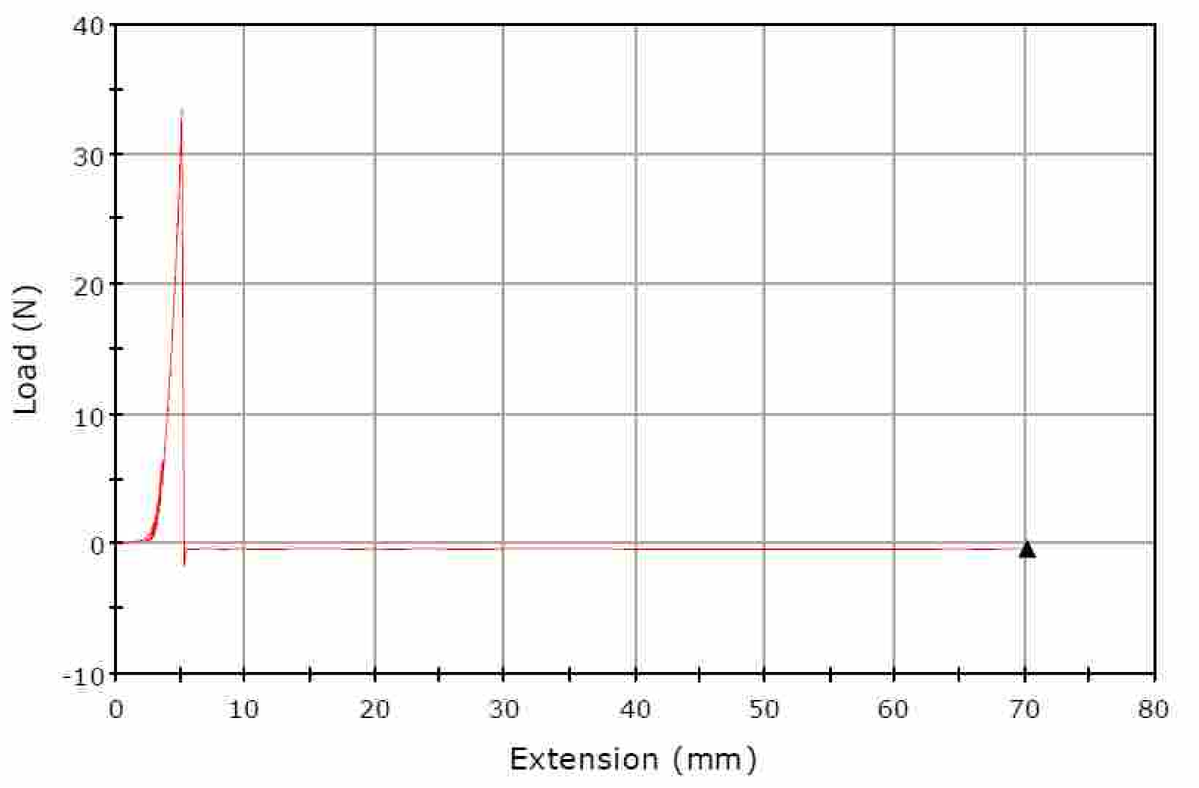

Figure 5.6 The load-extension data for the same test as in Figure 5.5. The curve is retraced several times, but is consistent with data collected by continuously increasing the load.

for the test where load was continuously increased (though inadvertently) in Figure 5.4 (b) confirms that holding the load does not significantly affect the shape of the curve. Similar results have been obtained in repeated trials using this program, and we believe that it will be reliable in gradually applying and holding loads to enable the collection of spectroscopic data.

It should be noted that the two sets of data do differ significantly in the load at break. The test with continuously increasing load broke at about 200 N, whereas the test with holds broke at about 35 N. Different adhesives were used to attach the post in the two trials shown in Figure 5.4-Figure 5.6, and we used different strength testing programs to test the two samples; however, such a discrepancy is also not uncommon for nominally identical samples tested using the same strength-testing program.

Several variables that are challenging to control affect the strength of the resulting adhesive bond, including the amount of adhesive used to attach the post and the pressure applied to the post when it was attached. Such variables would definitely need to be eliminated if these adhesive tests were performed as a way to determine the standard adhesive strength of these systems. However, we believe that as long as VSFG signal can be reliably correlated with the behavior of the adhesives the study can still be considered successful, even if the behavior of the adhesives is not otherwise predictable.

5.6 Preliminary data combining strength testing and VSFG spectroscopy

A significant challenge with collecting resonant VSFG spectra of adhesion phenomena using VSFG is that the signal from the buried interface tends to be weak. This is especially true for polystyrene, which is thought to have phenyl rings lying down nearly parallel with the surface of the substrate for hydrophilic substrates. This orientation of phenyl rings weakens the interaction of phenyl vibrational modes with the electric fields of the input beams. While using a hydrophobic substrate could increase VSFG resonant signal, it also reduces adhesion and makes the dynamic testing significantly more difficult. In most studies it is desirable to increase the delay between the visible and infrared pulses such that the nonresonant signal is completely suppressed.[2] However, due to the weak resonant signal, in our preliminary studies coupling VSFG with strength measurements, we have included a maximum amount of nonresonant signal. Figure 5.7 shows a VSFG spectrum collected from a sample similar to that shown in Figure 5.3 (b), made by coating a fused silica window with a 100 nm film of polystyrene and a 100 nm film of PMMA, then attaching the post directly to the PMMA with rubber cement. To collect the spectrum in Figure 5.7 (a), the sample was placed in the holder, but no force was applied with the strength tester, and the spectrum contains only one very weak peak at about 2950 cm^{-1}. Figure 5.7 (b) shows the VSFG spectrum as the sample is further stressed with 23 N of load applied. The peak broadens out and increases in intensity from the spectrum when no force was applied as the spectrum becomes dominated by nonresonant signal. Figure 5.7 (c) shows that as the sample is further stressed to 58 N, the peak begins to decrease in intensity again, until in Figure 5.7 (d) under 110 N of load, the signal contains no distinguishable features. The adhesive bond between the post and the rubber cement failed during the ramp up to ~135 N of load shortly after the collection of the spectrum in Figure 5.7 (d).

The only feature that looks as though it could result from a resonant peak appears only very weakly in Figure 5.7 (a) at about 2950 cm^{-1}. None of the polystyrene peaks appear at that frequency, so this peak must either result from a vibrational mode in PMMA or the rubber cement. Wang *et al.* attributed a strong peak in the *ssp* spectrum of PMMA at 2960 cm^{-1} to the methyl asymmetric stretch;[5] however, the same group published another paper just months later attributing this peak (now at 2955 cm^{-1}) to the symmetric stretch of the ester methyl group.[6] In

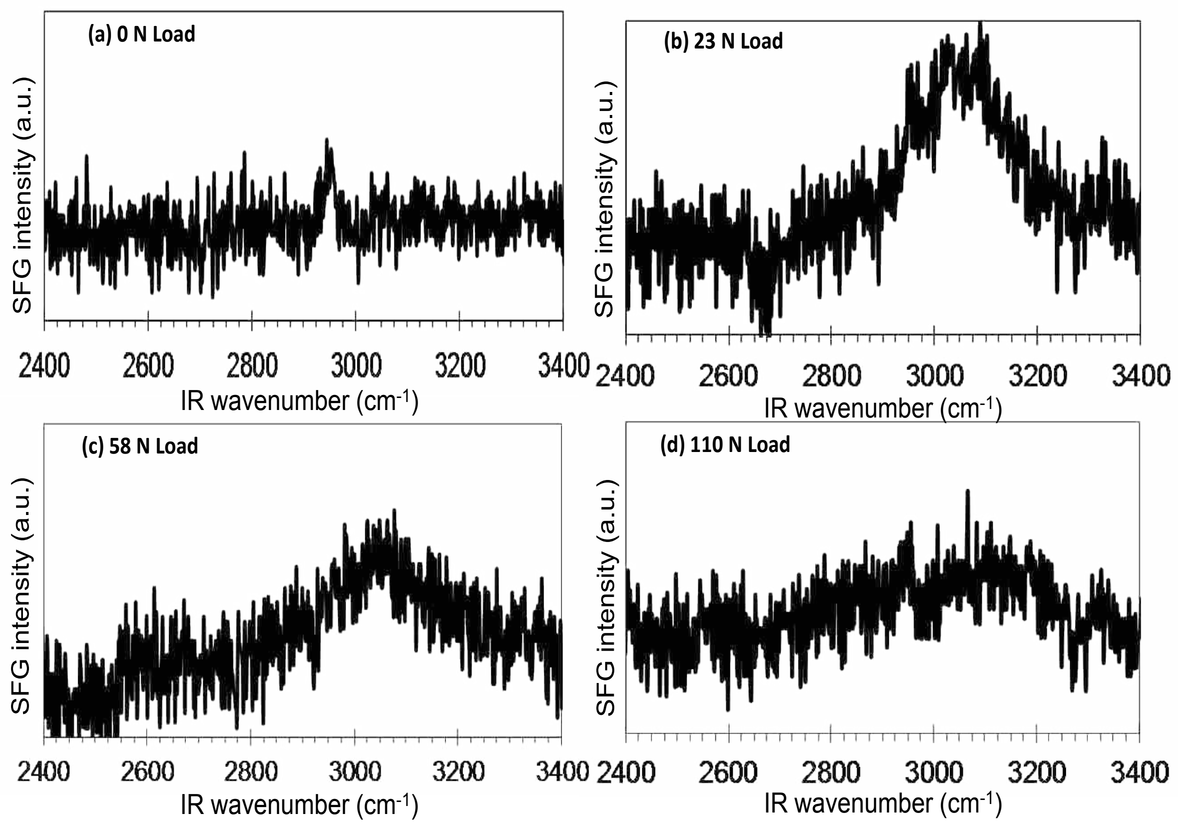

Figure 5.7 VSFG spectra of a polystyrene/ PMMA thin film coated on fused silica. The film was attached to the post using rubber cement with various amounts of load on the adhesive bond.

addition to the inconclusiveness in the mode assignment of the dominant peak in PMMA spectra, our spectra contain a high degree of nonresonant signal, which has been known to distort peak parameters, including position.[7,8] Because of the discrepancies in the literature and the presence of nonresonant signal in the spectra of Figure 5.7, we will refrain from making a specific mode assignment to this peak.

Although the dominance of the nonresonant signal in these spectra precludes any analysis of the resonant signal, the fact that the nonresonant signal changes throughout the testindicates that some molecular-level change or changes occur as load is applied to the adhesive bond. That these changes occur even before nearing the breaking point is further encouraging because even without a molecular-level explanation of adhesive failure, it provides a spectroscopic signature to warn of impending adhesive failure. With further knowledge of the molecular origins of the nonresonant signal, these spectroscopic signatures of failure could be tied to the specific molecular-level changes that are occurring at the adhesive bond.

Unfortunately, this experiment was only successfully performed once. The spectra presented in Figure 5.7 were collected prior to the development of a program to increase the load incrementally and hold the load while spectra were collected, and by the time a program had been developed to overcome this challenge, the laser system began malfunctioning. Upon restoration of spectrometer functionality, we hope to repeat these tests using the new strength tester program so that we will have more information about the macroscopic mechanical behavior of the adhesive bond as well as the ability to collect spectroscopic data at multiple points prior to sample breakage.

5.7 Conclusions and Future work

Studying adhesion processes on a molecular level is made difficult by the location of adhesive interactions at buried interfaces. Bulk and most surface-specific spectroscopic techniques fail to selectively probe this region of the sample nondestructively, but vibrational sum frequency generation spectroscopy (VSFG) can achieve the interface specificity necessary to probe functional adhesives. A previous VSFG study of polymer adhesion by Wilson *et al.* performed adhesion strength testing separately from the spectroscopic analysis.

To tie the changes we observed in the VSFG spectra throughout strength testing of the adhesive bond to orientational changes, we must either improve understanding of the nonresonant signal or improve the intensity of the resonant signal. Although it is thought that nonresonant signal originates from an electronic response in the sample, evidence tying structural properties to nonresonant signal shape and intensity is lacking. We have observed previously that annealing and aging polymer films increases nonresonant response,[7,8] and hypothesize that this increase in nonresonant response comes from molecules adopting a broader distribution of orientations. One study to test this hypothesis is underway that will compare the nonresonant signal from metals with known but differing amounts of surface dislocations.

Additional work must also be carried out to attempt to find an adhesive with the right properties to study how the relative amplitudes of resonant peaks change over the course of a strength test. The adhesive should bond well with both the fused silica substrate and the post used for stressing the adhesive, but also have a preferred molecular orientation at the buried interface that interacts strongly enough with the input beams to generate a detectible VSFG response. One such polymer that could be used is poly(ethyleneglycol terephthalate) (PET). PET contains phenyl rings like polystyrene but the phenyl rings are in the main polymer chain rather than attached as a side group. The phenyl C-H vibrational modes are ideal for study with VSFG because the technique is sensitive to small amounts of aliphatic surface contamination, and the phenyl modes appear at a much higher frequency than peaks from aliphatic contamination. In our studies so far, we have found that PET bonds strongly to hydrophilic surfaces, and because the phenyl rings are less free to rotate, they may be less likely to lie down toward the substrate than the polystyrene phenyl rings and therefore more able to interact strongly with the VSFG input beams. This work will be continued upon repair of the VSFG system.

Despite the challenges that still must be overcome to determine a meaningful relationship between the orientation of molecules and macroscopic properties of a functional adhesive bond, we have made significant steps toward doing so. We have made samples that can withstand applied stress for sufficient time to collect VSFG spectra under stress. A strength tester has been coupled with the VSFG spectrometer so that simultaneous spectroscopic measurements and strength testing can be carried out. We have designed a program to apply stress incrementally to the sample and hold that stress until a spectroscopic measurement can be made, and have collected preliminary data demonstrating changes in VSFG signal when stress is added to the adhesive bond. With improvements to our understanding of nonresonant signal and the study of different polymers with more significant resonant VSFG response, we will be able to tie these changes in the VSFG spectra to structural changes to molecular orientation at the adhesive interface.

5.8 References

(1) Lagutchev, A.; Hambir, S. A.; Dlott, D. D. *J. Phys. Chem. C* **2007**, *111*, 13645.

(2) Curtis, A. D.; Asplund, M. C.; Patterson, J. E. *J. Phys. Chem. C* **2011**, *115*, 19303.

(3) Briggman, K. A.; Stephenson, J. C.; Wallace, W. E.; Richter, L. J. *J. Phys. Chem. B* **2001**, *105*, 2785.

(4) Wang, J.; Woodcock, S. E.; Buck, S. M.; Chen, C.; Chen, Z. *J. Am. Chem. Soc.* **2001**, *123*, 9470.

(5) Wang, J.; Chen, C.; Buck, S. M.; Chen, Z. *J. Phys. Chem. B* **2001**, *105*, 12118.

(6) Curtis, A. D.; Burt, S. R.; Calchera, A. R.; Patterson, J. E. *J. Phys. Chem. C* **2011**, *115*, 11550.

(7) Curtis, A. D.; Reynolds, S. B.; Calchera, A. R.; Patterson, J. E. *J. Phys. Chem. Lett.* **2010**, *1*, 2435.

Chapter 6: . Final Remarks and Future Work

6.1 Final Remarks

The objective for this project was to study adhesive mechanisms using vibrational sum-frequency generation spectroscopy (VSFG). Towards this end, we refined VSFG experimental techniques and analysis and designed a system coupling a VSFG spectrometer to a strength tester. We can now be confident in the analysis of the VSFG data we collect, and all of the equipment is now in place to accomplish simultaneous study of quantitative adhesion strength with a strength tester and interfacial study with VSFG. Preliminary data have been collected showing changes in the nonresonant signal as a sample is stressed leading up to failure of the adhesive bond.

Admittedly, the most important advances made in this project so far have been in refining the VSFG spectroscopic technique. Common practice in VSFG experiments has been to declare a spectrum free of nonresonant signal if it is free of the broad pedestal and dispersive lineshapes typical in spectra containing large amounts of nonresonant signal. In this work, we have shown through mathematical modeling and experiment that the presence or absence of nonresonant signal cannot be determined solely on the basis of these indicators, and again confirmed that even small amounts of nonresonant signal can distort the apparent parameters of resonant peaks. In addition, we have developed a new way to detect nonresonant signal in spectra of certain systems by selectively filtering the "forbidden" signal polarization from the data.

The ability to completely remove nonresonant signal enabled the observation of changes in the orientation of phenyl rings in the bulk of polystyrene thin films on polished silicon upon exposure to a radio-frequency air plasma source.[1] Such changes had never before been seen in prior VSFG studies because such studies were always performed using fused silica as a substrate to mitigate the effects of nonresonant interference, and the change to bulk phenyl orientation does not occur with fused silica as a substrate for the coating. Previous studies additionally reported total destruction of surface phenyl rings because VSFG data collected following plasma treatment showed a lack of peaks from phenyl C-H modes;[2-4] however, when nonresonant signal is removed, a peak appears at 3027 cm^{-1} indicating that phenyl rings remain, but adopt a different average orientation than in untreated films.

We further showed that the immediate changes in the orientation of phenyl rings in polystyrene caused by plasma treatment do not persist after the films are annealed. After annealing, the orientation of phenyl rings in the bulk and on the surface of plasma-treated polystyrene on both substrates is identical; however, this orientation is different than what was observed prior to plasma treatment. As with the initial changes in orientation due to plasma treatment, the complete removal of nonresonant signal was necessary to observe these changes due to annealing. Nonresonant signal distorts spectra differently and unpredictably, and even spectra with the same resonant parameters appear to be different when nonresonant signal is present.[5,6] Changes in nonresonant signal, if present, would have presented an impossible problem in data analysis; therefore, results of the study would have been inconclusive.

The plasma paper demonstrated the use of VSFG to gain new information about the mechanics of a process, whereas most previous studies simply showed that VSFG data can be interpreted to give a result that agrees with well-established knowledge or to give an explanation to a previously known phenomenon. Moreover, the study provided compelling evidence against the common assumption that plasma treatment of polymers affects only the free surface. This power to refute a hypothesis is necessary for VSFG to be useful for the study of processes such as adhesion that were previously inaccessible to direct spectroscopic study.

In addition to the improvements to the VSFG technique, we have also made preparations to study adhesion phenomena through traditional strength testing measurements with simultaneous VSFG data collection. We designed a pulley system and mechanism to couple the strength tester to the VSFG spectrometer, found a coating that withstands the sustained stress imposed by the strength tester long enough to collect VSFG spectra, designed a strength testing program that gives proper control over testing parameters to enable the coupled experiments, and collected preliminary data demonstrating changes in the nonresonant signal from the sample with applied stress to the adhesive bond.

6.2 Future work

The dominant signal detected in the preliminary VSFG data from the adhesion studies is nonresonant; therefore, we need more information about the nonresonant signal in order to make any conclusions regarding the relationship between structure and the function of an adhesive bond from these data. We already know that nonresonant signal depends on the identity of substrates, the thickness of coatings, and the history of the sample, and it is thought to arise from a fast electronic response in the sample.[7,8] By scanning frequencies that are not resonant with vibrational modes in the sample, we can also isolate nonresonant signal to study it free of any apodization effects from the resonant signal.

Despite what we already know about the properties of the nonresonant signal in VSFG, we still do not know what relationship, if any, exists between nonresonant signal intensity and molecular orientation. Current work in our lab performed by Shawn Averett in collaboration with several professors from the Mechanical Engineering department seeks to study changes in nonresonant signal from metals as they are stressed. The stress-induced changes in metallic surface structure have been well-studied by other methods. Observation of how nonresonant signal VSFG signal from these materials changes with stress could provide the needed link between structural ordering and nonresonant signal in other materials.

6.3 References

(1) Calchera, A. R.; Curtis, A. D.; Patterson, J. E. *ACS Appl. Mater. Interfaces* **2012**, *4*, 3493.

(2) Li, J.; Oh, K.; Yu, H. *Chin. J. Polym. Sci.* **2005**, *23*, 187.

(3) Zhang, D.; Dougal, S. M.; Yeganeh, M. S. *Langmuir* **2000**, *16*, 4528.

(4) Zhang, C.; Wang, J.; Khmaladze, A.; Liu, Y.; Ding, B.; Jasensky, J.; Chen, Z. *Opt. Lett.* **2011**, *36*, 2272.

(5) Curtis, A. D.; Burt, S. R.; Calchera, A. R.; Patterson, J. E. *J. Phys. Chem. C* **2011**, *115*, 11550.

(6) Curtis, A. D.; Reynolds, S. B.; Calchera, A. R.; Patterson, J. E. *J. Phys. Chem. Lett.* **2010**, *1*, 2435.

(7) Roke, S.; Kleyn, A. W.; Bonn, M. *Chem. Phys. Lett.* **2003**, *370*, 227.

(8) Malyk, S.; Shalhout, F. Y.; O'Leary, L. E.; Lewis, N. S.; Benderskii, A. V. *J. Phys. Chem.C* **2012**, *117*, 935.

Chapter 7: Appendix

7.1 Spin-coating parameter tables

**Given thicknesses are approximate.*

7.1.1 Thin Solvent Layer

Concentration: Pure solvent

Step	Time	Speed	Acceleration
1	2 s	167 RPM	500 RPM/s
2	10 s	400 RPM	3000 RPM/s

7.1.2 Polystyrene in Toluene

7.1.2.1 50 nm

Concentration: 1% polystyrene by weight

Step	Time	Speed	Acceleration
1	2 s	1000 RPM	500 RPM/s
2	55 s	1500 RPM	3200 RPM/s

7.1.2.2 100 nm

Concentration: 2% polystyrene by weight

Step	Time	Speed	Acceleration
1	2 s	2000 RPM	500 RPM/s
2	55 s	2500 RPM	3200 RPM/s

7.1.2.3 220 nm

Concentration: 3% polystyrene by weight

Step	Time	Speed	Acceleration
1	2 s	1000 RPM	500 RPM/s
2	55 s	1500 RPM	3200 RPM/s

7.1.3 Poly(methyl methacrylate) in Nitromethane

**The following programs were determined by layering PMMA on top of PS, but may also give similar thicknesses for layering on a clean uncoated substrate*

p. 43 in first lab book?

7.1.3.1 150 nm

Concentration: 3% PMMA by weight

Step	Time	Speed	Acceleration
1	2 s	2000 RPM	500 RPM/s
2	55 s	2500 RPM	3200 RPM/s

7.1.3.2 240 nm

Concentration: 4% PMMA by weight

Step	Time	Speed	Acceleration
1	2 s	1000 RPM	500 RPM/s
2	55 s	1500 RPM	3200 RPM/s

7.2 Substrate abbreviations for systematic naming

Note: *abbreviations are included for informative purposes within the lab, and not all substrate types were used to collect data included in this document.*

SPS = Single Polished Silicon. This is used for all silicon substrates that are polished on one surface, regardless of orientation. However, all of the data in this document was collected using silicon (111) substrate.

FSW = Fused silica window.

SSN = Thin stainless steel mirror (these are cut into squares, and have a white adhesive protective covering over the polished surface)

NSW = Thin sapphire window - 1/8" thick, 1" diameter window of amorphous sapphire

KSW = Thick sapphire window - 1/4" thick, 1" diameter window of amorphous sapphire

ZSAP = Single crystal "zero-degree" or "z-cut" sapphire. This specific orientation is chosen for use in spectroscopy because sapphire is slightly birefringent, and it is cut from the (0,0,0,1) plane, perpendicular to the optical plane.

QMS = Fused silica microscope slide. These are usually cut into squares prior to coating.

GMS = Glass microscope slide. These are usually cut into squares prior to coating.

7.3 MATLAB Code for Theoretical Modeling

7.3.1 Custom functions used in modeling

**These functions were developed by Dr. Alex D. Curtis. They are included in this Appendix because they are utilized in the MATLAB models that follow but are not included in standard MATLAB packages.*

7.3.1.1 (Complex) Gaussian

Makes a function whose modulus squared is a single Gaussian peak, and is able to interfere with neighboring peaks in its complex form. The full derivation of the form of this function can be found in the dissertation of Dr. Alex D. Curtis (2011), starting on page 233.

```
function g = gaussian(a,x)
    g = zeros(length(x),1);
    g = g+sqrt(a(3)).*(exp(-((x-
a(1)).*2.*sqrt(log(2))./(sqrt(2).*a(2))).^2)).*exp(1i.*-
atan(0.5.*a(2)./(x-a(1))));
end
```

7.3.1.2 Lorentzian

Makes a function whose modulus squared is a single Lorentzian peak. This is the standard form of a Lorentzian peak, which is already complex and therefore able to interfere with neighboring peaks.

```
function l = lorentzian(a,x)
    l = zeros(length(x),1);
    l = l+sqrt(a(3)).*a(2)./((x-a(1))+1i.*a(2));
end
```

7.3.2 Modeling attenuated nonresonant signal

```
clear all

%Set up basic variables
x = (linspace (0,10000, 10000))';
hz = x.*2.998e10;
t = (linspace(0,length(hz)./(max(hz)-min(hz)),10000))';
timestepsize = (max(t)-min(t))./length(t);
L1 = lorentzian([3026.98 7.31 0.43],x);
L2 = lorentzian([3044.86 .86 -0.013],x);
L3 = lorentzian([3057.52 2.13 0.064],x);
L4 = lorentzian([3068.80 3.85 1],x);
L5 = lorentzian([3084.67 2.56 -0.016],x);
Res = L1 + L2 + L3 + L4 + L5;
NRctr = 3069;
NRHWHM = 200;
NRAmp = 1;
NR = gaussian([NRctr;NRHWHM;NRAmp],x);

%Attenuation
NRamt = 1;
normNR = NR./max(NR);
normRes = Res./max(Res);
att = abs(normNR).^2-(NRamt.*(abs(normRes).^2));
plot(x,att);
```

7.3.3 Modeling a resonant signal with nonresonant interference

7.3.3.1 Resonant signal with Gaussian nonresonant interference

```
clear all

%Set up basic variables
x = (linspace (0,10000, 10000))';
hz = x.*2.998e10;
t = (linspace(0,length(hz)./(max(hz)-min(hz)),10000))';
timestepsize = (max(t)-min(t))./length(t);
L1 = lorentzian([3026.98 7.31 0.43],x);
L2 = lorentzian([3044.86 .86 -0.013],x);
L3 = lorentzian([3057.52 2.13 .064],x);
L4 = lorentzian([3068.80 3.85 1],x);
L5 = lorentzian([3084.67 2.56 -.016],x);
Res = L1 + L2 + L3 + L4 + L5;
NRctr = 3069;
NRHWHM = 200;
NRAmp = 1;
NR = gaussian([NRctr;NRHWHM;NRAmp],x);

%Combine NR and Res parts
tRes = (fft(Res));
tNR = (fft(abs(NR).^2));
tResNR = (NRamt.*tNR) + (tRes);
ResNR = ifft(tResNR);

%Plot spectrum
figure(1)
hold on
xmin = 2900;
xmax = 3200;
ymin = -0.2;
ymax = 1;
axis([xmin xmax ymin ymax])
xlabel('Frequency(cm-1)')
ylabel('SFG Intensity (a.u.)')
plot(x,abs(ResNR).^2);
```

7.3.3.2 *Resonant signal with attenuated nonresonant interference*

```
clear all

%Set up basic variables
x = (linspace (0,10000, 10000))';
hz = x.*2.998e10;
t = (linspace(0,length(hz)./(max(hz)-min(hz)),10000))';
timestepsize = (max(t)-min(t))./length(t);
L1 = lorentzian([3026.98 7.31 0.43],x);
L2 = lorentzian([3044.86 .86 -0.013],x);
L3 = lorentzian([3057.52 2.13 .064],x);
L4 = lorentzian([3068.80 3.85 1],x);
L5 = lorentzian([3084.67 2.56 -.016],x);
Res = L1 + L2 + L3 + L4 + L5;
NRctr = 3069;
NRHWHM = 200;
NRAmp = 1;
NR = gaussian([NRctr;NRHWHM;NRAmp],x);

%Attenuation
NRamt = 1;
normNR = NR./max(NR);
normRes = Res./max(Res);
att = abs(normNR).^2-(NRamt.*(abs(normRes).^2));

%Combine NR and Res parts
tRes = (fft(Res));
tNR = (fft(abs(att).^2));
tResNR = (NRamt.*tNR) + (tRes);
ResNR = ifft(tResNR);

%Plot spectrum
figure(1)
hold on
xmin = 2900;
xmax = 3200;
ymin = -0.2;
ymax = 1;
axis([xmin xmax ymin ymax])
```

```
xlabel('Frequency(cm-1)')
ylabel('SFG Intensity (a.u.)')
plot(x,abs(ResNR).^2);
```

7.3.4 Prompted MATLAB program for modeling an apodized spectrum of polystyrene with or with a custom S/N and custom ratio of nonresonant to resonant signal amplitude

```
clear all

%Set up basic variables
x = (linspace (0,10000, 10000))';
hz = x.*2.998e10;
t = (linspace(0,length(hz)./(max(hz)-min(hz)),10000))';
timestepsize = (max(t)-min(t))./length(t);
L1 = lorentzian([3026.98 7.31 0.43],x);
L2 = lorentzian([3044.86 .86 -0.013],x);
L3 = lorentzian([3057.52 2.13 .064],x);
L4 = lorentzian([3068.80 3.85 1],x);
L5 = lorentzian([3084.67 2.56 -.016],x);
Res = L1 + L2 + L3 + L4 + L5;
NRctr = 3069;
NRHWHM = 200;
NRAmp = 1;
NR = gaussian ([NRctr;NRHWHM;NRAmp],x);

%Visible Pulse Model
gauss=abs(gaussian([2.2898e-12 1.0561e-12 .41961],t)).^2;
decay1=exp(-10.08e11.*t);
decay2=exp(-10.08e11.*t);
decay3=exp(-10.08e11.*t);
single=ifft(fft(gauss).*fft(decay3)); %Single Etalon profile
double=ifft(fft(gauss).*fft(decay1).*fft(decay2)); %Double
Etalon profile
[~,vismaxindexsingle] = max(single);
[~,vismaxindexdouble] = max(double);

prompt = {'NR/Res='};
    dlg_title = 'NR Relative to Resonant';
    num_lines = 1;
    def = {'0.2'};
    options.WindowStyle = 'normal';
    options.Resize = 'on';
    inputs = inputdlg(prompt,dlg_title,num_lines,def,options);
    NRamt = (str2double(inputs));
```

```
 prompt = {'time delay'};
    dlg_title = 'visible delay (s)';
    num_lines = 1;
    def = {'2.3e-12'};
    options.WindowStyle = 'normal';
    options.Resize = 'on';
    inputs = inputdlg(prompt,dlg_title,num_lines,def,options);
    timedelay = (str2double(inputs));

 prompt = {'Add Gaussian White Noise'};
    dlg_title = 'Desired S:N Ratio (dB)';
    num_lines = 1;
    def = {'30'};
    options.WindowStyle = 'normal';
    options.Resize = 'on';
    inputs = inputdlg(prompt,dlg_title,num_lines,def,options);
    snr = (str2double(inputs));

%Create Apodized Model Spectra
normNR = NR./max(NR);
normRes = Res./max(Res);
tNR = fft(NR);
tRes = (fft(Res));
tResNR = (NRamt.*tNR) + (tRes);
ResNR = ifft(tResNR);
delay = ((-
1.*vismaxindexsingle)+1+(round(timedelay./timestepsize)));
shift=circshift(single,delay);
shift = shift./max(shift);
Sample= ifft(fft(ResNR).*shift);
Sample = abs(Sample).^2;
Sample = Sample./max(Sample);
Model = awgn(Sample,snr); %Add Gaussian Noise

x = x(2950:3150);
Model = interp1(Model,x);

figure(1)
hold on
xmin = 2900;
xmax = 3200;
ymin = -0.2;
ymax = 1;
axis([xmin xmax ymin ymax])
xlabel('Frequency(cm-1)')
ylabel('SFG Intensity (a.u.)')
```

```
plot(x,Model);
```

7.4 General instructions for using Instron 3345 tensile tester

7.4.1 Programming a prompted test method

1. From the home screen, click "Method."
2. Edit an existing test method or create a new one. To edit an existing method, choose a method on the "recently used methods" list or click the folder icon labeled "open" on the right side of the screen. To create a new test method, click the circle on the right side of the screen labeled "New..." then select the type of method to be created. The most common type that we use is the Test Profiler Method.
3. On the left side of the screen, the "General" tab is automatically selected. This tab is divided into four sections: Method, Sample, Basic Layout, and Advanced Layout. The "Method" subsection allows the user to select a system of units that the test method will use by default, define how the specimen parameters will be assigned, and write a description of the method. The "Sample" subsection allows the user to enter default inputs to describe the samples to be tested, or leave them blank. The labels that appear above the entry boxes can be changed by clicking the ellipses button to the right of the field and changing the text in the field labeled "Prompt." "Basic Layout" allows the user to select how the test screen looks from defaults, and "Advanced Layout" gives the user additional control over the layout seen during a test.
4. The "Specimen" tab is directly below the "General" tab and contains five sub-sections: Dimensions, Number Inputs, Text Inputs, Choice Inputs, and Notes. The "Dimensions" subsection allows entry of default specimen dimensions. For adhesion samples, this is not altered from the defaults. Number inputs allows the user to enter prompts and default values for numerical inputs. The prompts are changed ("Custom Number Input 1, 2, etc" are the

defaults) in the same manner as before, by clicking the ellipses on the right of the field. The "text inputs" subsection is where the user enters prompts and default values for text. "Choice inputs" allows the user to add drop-down menus that the operator can use to record sample parameters from a pre-determined list. The "Notes" likewise allows the programming of prompts and defaults for larger bodies of text notes about the sample.

5. The "Control" tab allows the user to control the behavior of the Instron during a test. The pre-test tab allows the user to decide to preload, auto balance, or pre-cycle prior to the beginning of the test. Usually none of these are selected. The Test tab allows for fine control of the testing parameters. What appears in this tab differs depending on what type of method has been selected, but for the test profiler method there is an option to edit the test profile. Edit the test by clicking "Edit Profile," and a Test Profiler window appears on top of the method screen. The test profile contains blocks that can be edited individually, or more blocks can be added, depending on what specific steps are desired during a test. The test profile must be saved prior to exiting if the changes are to be preserved in the test method. The "end of test" section allows the user to define limits that end the test automatically. It is wise to set one of the criteria to be the load reaching a value below the threshold value of the force transducer most frequently used for the test method to protect the force transducer from damage. Up to four criteria can be entered, and the test will end whenever one of the criteria is met.
6. The "Calculations" tab is just beneath the "Control" tab. This tab allows the user to select which calculations to perform automatically on the test data. Many calculations are built in to the program. Calculations are added to the "selected calculations" list on the right from the "available calculations" list on the left by selecting a calculation and clicking on the

arrow pointing to the right. To remove a selected calculation from the list, select the calculation and click on the arrow pointing to the left. For each calculation, there is an option whether to show it on the graph or not. This option is accessed by selecting the calculation in the list of selected calculations and checking the box in the bottom section of the screen that says "Indicate on graph."

7. The Results tabs allow the user to select which results are displayed in each results table on the report. There are two tabs, so two tables can be displayed on the results readout.
8. The Graphs tabs allow the user to select what data is plotted on each of up to two graphs to be displayed in the results readout, including the selection of x and y data, and how many curves are displayed on each graph.
9. The Reports tab allows the user to select the format, template, and output path of the report generated by tests performed using the method. The template used can be edited in the green "Report" tab at the top of the screen.
10. The final tab on the left side of the screen is "Test Prompts." This tab allows the user to determine how the method prompts the operator during a test. On this screen, check the "Run as a Prompted Test" box to run the method as a prompted test, and then select when to prompt the user by checking the boxes next to the desired options. The options selected will then appear as sub-sections below "Prompt Sequence" in the "Test Prompts" tab, and the inputs and prompts requested of the operator by the method can be selected in these sub-sections.
11. The buttons at the top of the screen, labeled "key 1" and "key 2" can also be customized. The circular button immediately to the left of these two buttons opens the control panel where the "soft key" assignments can be changed with two drop-down menus.

7.5 Prompted test "Adhesion Testing Method Starter" for adhesion samples

The following section contains information that should be in the tabs to the left of the screen for the prompted test designed for adhesion samples. This test method is saved on the computer used to operate the Instron; however, these instructions are designed be used to reproduce the program if necessary.

7.5.1 Soft Key Assignments:

Key 1: End Hold

Key 2: Balance Load

7.5.2 General

7.5.2.1 Method

Test Type: Tension - TestProfiler

System of Units: SI

Assign specimen parameters from: Method default

Method description: Load is ramped to 10N upon start, and load is sustained for 10 seconds (or user input). Another 10 N load is added, and the load is held for another 10 seconds or until user input. This cycle repeats until the test is ended.*

*Changes can be made to how long the load is sustained; the time should be at least as long as needed for a VSFG scan. The description should be changed to reflect changes within the test profiler.

7.5.2.2 Sample

Sample Name: FSW123 (This should match the name given to the sample when collecting spectroscopic data)

Coatings:

Adhesives: (left blank)

Other Notes (Optional): (left blank)

7.5.2.3 Advanced Layout

Skip over the Basic Layout tab and go to the Advanced Layout tab to set up the layout for the test screen as shown approximately in Figure 1.1. The elements shown on the screen can be moved to different panes by selecting the element and using the up and down arrows on the right of the screen to move them up and down on the list. The size of the panes can be adjusted by hovering the mouse over the border between panes and dragging it to the desired position.

7.5.3 Specimen

The only tab where the needed values are different from the default values is the "Text Inputs" tab. Leave Dimensions, Number Inputs, Choice Inputs, and Notes as the default values.

7.5.3.1 Text Inputs

Specimen label: ex: FSW123

Coatings: ex: Polystyrene, 100 nm; PMMA, 200 nm

Adhesive to attach post: Multi-purpose Cement

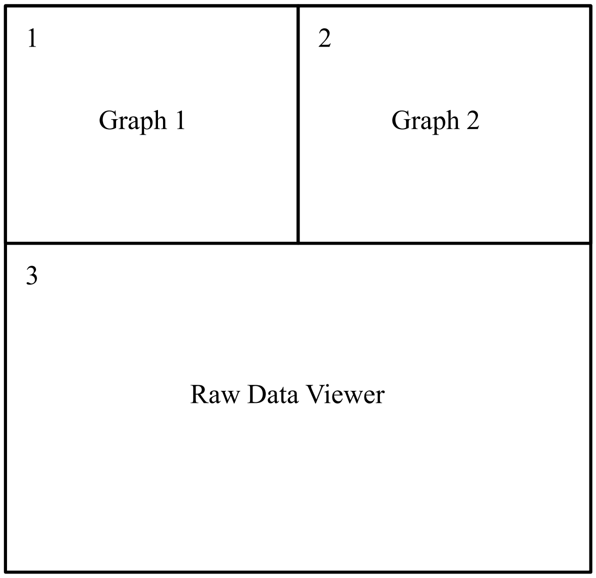

Figure 7.1 Example of the screen setup for adhesion test methods

7.5.4 Control

7.5.4.1 Pre-Test

None of the check boxes should be checked on this screen.

7.5.4.2 Test

Click on the "Edit Profile..." button. This opens another window that allows the user to edit the test profile blocks. The following settings should be entered for each block:

<u>Block 1 Parameters:</u>

Mode: Extension

Shape: Absolute Ramp

Name: 1 Absolute Ramp

EndPoint: 10.0 N

Rate: 10.0 mm/min

<u>Block 2 Parameters:</u>

Mode: Load

Shape: Hold

Name: 2 Hold

Criteria: Duration

Duration: 0.1667 Minutes (10 seconds) (This should be changed to be at least as long as a spectroscopic scan, if not slightly longer)

<u>Block 3 Parameters:</u>

Mode: Extension

Shape: Relative Ramp

Name: 3 Ramp

Delta: 10.0 N

Rate: 10.0 mm/min

Block Control Tab:

Repetition: Enabled (checkbox)

Repetitions: 50 (this number can be increased or decreased if necessary)

Loop to block: 2

Name: 2 Hold

End Test Sequence: Stop

7.5.4.3 End of Test

End of Test 1

Criteria 1: Load

Value 1: 400 N

End of Test 2

Criteria 2: Extension

Value 2: 200 mm

7.5.4.4 Data

Data capture: Manual

Criteria 1:

Channel 1: Time

Interval 1: 100 ms

7.5.5 Calculations

7.5.5.1 Setup

Selected calculations: Break (Standard) and Modulus (Automatic). Break is indicated on graph.

7.5.6 Results 1

7.5.6.1 Columns

Selected Results: Specimen label, Coatings, Adhesive to attach post, Load at break (Standard), Data Point at Break (Standard), Extension at Break (Standard)

7.5.6.2 Format

Style 2 (built in to Blue Hill 2 Software) - this can be easily changed to user preference

7.5.7 Graph 1

7.5.7.1 Type

Multispecimen

Graph Title: Specimen %n to %m

Curves per graph: 4

Offset each curve by: Auto

Enable data point selector (checkbox)

7.5.7.2 x-data

Channel: Extension

Units: mm

Automatic scaling

7.5.7.3 y-data

Channel: Load

Units: N

Automatic scaling

7.5.8 Graph 2

7.5.8.1 Type

Multi-specimen

Graph title: Specimen %n to %m

Curves per graph: 4

Offset each curve by: Auto

Enable data point selector

7.5.8.2 x-data

Channel: Time

Units: sec

Automatic scaling

7.5.8.3 y-data

Channel: Load

Units: N

Automatic scaling

7.5.9 Raw Data

7.5.9.1 Columns

Show all parameters (checkbox is checked)

Selected channels:

1. Time: Heading: Time, Units: sec, Rounding format: Decimal places, Value: 5

2. Extension: Heading: Extension, Units: mm, Rounding Format: Decimal Places, Value: 5

3. Load: Heading: Load, Units: N, Rounding format: Decimal places, Value: 5

7.5.9.2 Format

Default format

7.5.10 Reports

7.5.10.1 Documents

Template: C:\Documents and Settings\All Users\Documents\Instron\BlueHill\Templates\Report-Adhesion.i_rt (this path may need to be changed if the file needs to be replaced)

Document format: PDF

Save the document (checkbox checked)

Specify output path (Browse for a path where the files will be saved): C:\Documents and settings\PattersonLab\Desktop\Instron Results

7.5.10.2 Export Results

Export Results (checkbox checked)

Format: Comma Separated Values (.CSV)

Content: Results and Statistics

Selected Parameters:

Text Inputs: Specimen Label

General: Method Name

General: Method Description

Export Raw Data: Export raw data

Show category names (checkbox checked)

Show all parameters (checkbox checked)

7.5.10.3 Export Raw Data

Export raw data (checkbox checked)

Format: Comma Separated Values (.CSV)

Selected Results: Break (Standard): Load at break (Standard), Break (Standard): Extension at Break (Standard), Break (Standard): Time at Break (Standard)

Show category names (checkbox checked)

Show all parameters (checkbox checked)

7.5.11 Test Prompts

7.5.11.1 Prompt Sequence

Run as prompted test (checkbox checked)

Number of specimens in sample: 1

The following checkboxes should be checked: Prompt before test, show workspace after test, show workspace after calculations, prompt after specimen.

7.5.11.2 Before Test

Prompt before test: Make sure the specimen is properly installed in the test machine. Keep clear. Press the Start button to start the test and "End Hold" button to end holds.

Selected Parameters: Specimen label, coatings, adhesive to attach post

7.5.11.3 After Specimen

Prompt after specimen: Any special notes that should be considered?

Selected parameters: specimen note 1

7.5.12 Reports Tab

(The Reports tab is the green tab accessible through either the tabs at the top of the screen or from the home screen)

7.5.12.1 Body

This is the only section that needs to be altered from the defaults

Report Contents:

Selected items: Sample file name, Sample description, Method description, Defaults Table, Sample Note 1, Graph 1, Graph 2, Results Table 1

7.6 Running an adhesion test with the "AdhesionTesting Method Starter" method (or future methods based on it) on Instron 3345

1. If the computer connected to the tensile tester is on, turn it off. The computer must be turned off before the tensile tester can be turned on.

2. Check all connections between the Instron and the computer. Take this time to ensure that the appropriate force transducer is connected on the upper arm, and that the correct attachments are attached to the tester.
3. Turn on the Instron 3345 tensile tester.
4. Turn on the computer and sign in (Username: Instron; Password: pullme).
5. Start up the BlueHill2 software.
6. Click on the desired method name (ex: Adhesion Testing Method Starter), browse for the desired output path, and give a name to the output file.
7. Make sure the sample is properly positioned in the sample holder and the cable is attached through the pulley system on the tester.
8. Enter specimen label, coatings, and the adhesive used to attach the post in the fields provided.
9. Click on the green icon in the upper right-hand corner. In the Transducer Setup - Extension window that pops up, click "Reset Gauge Length" to reset the position to zero.
10. Click the "Balance Load" soft key at the top of the screen.
11. Click Start.
12. After the first load is on the sample, the Instron will hold that load for a pre-determined amount of time that is longer than the time needed to collect a single spectrum. When VSFG data collection at that load is finished, the test can be advanced to the next set load by clicking the End Hold soft key.
13. This is repeated until the test is over. A .CSV and PDF file with the results of the test will save to the default folder that has been selected for the method unless a different path was specified prior to the start of the test.